MEASUREMENT AND EVOLUTION OF THE THICKNESS DISTRIBUTION AND MORPHOLOGY OF DEFORMED FEATURES OF ANTARCTIC SEA ICE

A

THESIS

Presented to the Faculty

Of the University of Alaska Fairbanks

in Partial Fulfillment of the Requirements

for the Degree of

DOCTOR OF PHILOSOPHY

By

Tina Tin, M.Eng., B.A.

Fairbanks, Alaska

May 2003

ProQuest Information and Learning Company
300 North Zeeb Road
P.O. Box 1346
Ann Arbor, MI 48106-1346

MEASUREMENT AND EVOLUTION OF THE THICKNESS DISTRIBUTION AND MORPHOLOGY OF DEFORMED FEATURES OF ANTARCTIC SEA ICE

By

Tina Tin

RECOMMENDED:

Advisory Committee Chair

Chair, Department of Geology and Geophysics

APPROVED:

Dean, College of Science, Engineering and Mathematics

Dean of the Graduate School

4-21-03

Date

Abstract

Antarctic sea ice thickness data obtained from drilling on sea ice floes were examined with the goal of enhancing our capability to estimate ice thickness remotely, especially from air- or space-borne altimetry and shipboard visual observations. The state of hydrostatic equilibrium of deformed ice features and the statistical relationships between ice thickness and top surface roughness were examined. Results indicate that ice thickness may be estimated fairly reliably from surface measurements of snow elevation on length scales of ≥100 m. Examination of the morphology of deformed ice features show that Antarctic pressure ridges are flatter and less massive than Arctic pressure ridges and that not all surface features (ridge sails) are associated with features underwater (ridge keels). I propose that the differences in morphology are due to differences in sampling strategies, parent ice characteristics and the magnitude and duration of driving forces. As a result of these findings, the existing methodology used to estimate ice thickness from shipboard visual observations was modified to incorporate the probability that a sail is associated with a keel underwater, and the probability that keels may be found under level surfaces. Using the improved methodology, ice thickness was estimated from ship observations data obtained during two cruises in the Ross Sea, Antarctica. The dynamic and thermodynamic processes involved in the development of the ice prior to their observation were examined employing a regional sea ice-mixed layer-pycnocline model. Both our model results and previously published ice core data indicate that thermodynamic thickening is the dominant process that determines the thickness of first year ice in the central Ross Sea, although dynamic thickening also plays a significant role. Ice core data also indicate that snow ice forms a significant proportion of the total ice mass. For ice in the northeast Ross Sea in the summer, model results and evidence from ice core and oceanographic data indicate that dynamic thickening, snow ice formation and bottom melting compete to determine the ice thickness during mid and late winter.

Table of Contents

List of Figures

List of Tables

Acknowledgments

As the composition of this *magnus opus* (Measurement and evolution of the thickness distribution and morphology of deformed features of Antarctic sea ice, aka Five Years of Dreaming of Antarctica Every Day) draws to a close, I would like to thank the many people who have made this dream possible. Thanks to my advisor, Martin Jeffries, for giving me the opportunity to discover Alaska, Antarctica and the world of scientific research; for his patience and guidance in leading me to see the scientific way; for always finding time to review my numerous drafts and always returning them so promptly. Thanks to Bill Hibler and Shusun Li for being on my graduate advisory committee. Sincerest thanks to Keith Echelmeyer and Hajo Eicken, who, on top of being my committee members, taught me about ice, science and life.

Over the past five years I've become a fixture in the Geology Department. Thanks to all the friendly smiles and back rubs from the Geofriends who pass by my usual spot in the sun every day. Thanks to Paul Layer, for his statistical and non-statistical advice and for letting me call the 3rd floor of the Natural Sciences Building home. Thanks to June Champlin, Norma Pfeiffer and Wendy Uzzell in the Departmental Office who have made the ride along the paper trail as smooth as possible. Thanks to Bill Witte for making the Geology computer room (aka Witte World) so efficient, friendly and comfortable. Let's hope that future generations of Geology students can have the opportunity to enjoy it too. Additional computer support has been provided by the consultants at the Arctic Region Supercomputing Center who have been tireless in helping me use their Visualization Lab, no matter whether I'm sitting in the lab or somewhere in Europe. More support has come from the staff of the Keith B. Mather Library, including Ann Wood, Chisato Jimura and Judie Triplehorn who have been very helpful and efficient in procuring obscure journal articles.

Even in the dreamy world of Antarctic sea ice, money is still needed to pay for the fuel of the icebreakers and the fries that Ernest serves at 11:30 every night. Thanks to the National Science Foundation for funding Martin's fieldwork and most of my salary.

Additional salary support has been provided by a Teaching Assistantship from the Geology Department, by a Thesis Completion Grant from the Graduate School and by Roger Smith, Director of the Geophysical Institute. International collaborations and discussions at conferences have played a very important part in the development of my scientific thinking. My deepest gratitude to the Center for Global Change and Arctic System Research for awarding me a Global Change Student Research Grant. It has given me freedom and autonomy in making decisions about international collaboration and it also provided partial salary support. Thanks to the College of Science, Engineering and Mathematics, ASUAF and the GI student travel fund for additional travel funding.

Sometimes inspiration comes from unexpected places. Sometimes from half way around the world. I feel very fortunate to be at UAF during the years when Norbert Untersteiner (aka God of Sea Ice) set up his temporary residence here. His wisdom, candidness and anecdotes of adventures in life as well as in the scientific underworld always remind me that there are more important things in life than science and a Ph.D. thesis. Thanks to Uma Bhatt, the surrogate committee member, for her kind and generous encouragement. This thesis would not be as good as it is now and I wouldn't be defending it as confidently as I am today if it was not for my co-authors. Apart from Martin here in Fairbanks, I've solicited inspiration from around the world. Thanks to Jukka Tuhkuri and Mikko Lensu from Helsinki University of Technology in Finland for their fresh perspectives and technical input and for accepting me into the pressure ridge family so readily. Thanks to Ralph Timmermann from the Catholic University in Louvain-la-neuve, Belgium for putting his time, effort and trust in me and the project even before he knew me, and even after getting to know me. And the ones who got away: thanks to Tony Worby and Mark Hopkins for their constructive discussions and valuable insights. Maybe one day we will have the chance to work together. The beginning is often a difficult place to be. Thanks to Dan Hawkins and Cathy Geiger for showing genuine interest and enthusiasm in my work at an early stage of my research, making me start to believe in my own work. One of the things that I love about the sea ice community is the energy, the camaraderie and the friendliness. Thanks to Vicky Lytle, Christian Haas, Wolfgang

Dierking and Hajo for having never even hesitated to share their data with me. Thanks to Paula Kankaanpää, Jean-Louis Tison, Yanling Yu, Drew Rothrock, and John Walsh for welcoming my visits as well as my requests for advice. Thanks to all the sea ice buddies I've met during cruises and conferences – Ted Maksym, Paul Bond, Inga Smith, Josh Downer, Karen Assmann, Daniel Pringle, Knut Høyland, Mats Granskog and Janne Rintala. They made me realize that you can still be cool even if you are a sea ice geek. Thanks to the fellow students of the Snow, Ice and Permafrost Group at UAF for sharing the daily trials and tribulations of being a budding ice scientist.

It's impossible to thank everybody who has been important to me personally in the past five years. You guys, I'll thank you all personally with a huge fat kiss later. Here, though, are a few people who I feel need to be mentioned. Thanks to my long-suffering parents and brother for putting up with my intolerable stubbornness and individualism and still loving me. Thanks to Alain, Sharon, Sigrun and Shawna who have given me the family that I don't have to pretend to like. One year ago today, we lost Karoline. On hearing the news, Tony told me, "Now you have to finish your thesis for the two of you." No one can ever replace her, life will never be the same again. But, still, we try. This one's for you, Karoline.

March 24, 2003

Fairbanks, Alaska

Introduction

The Ross Sea is the body of water on the Antarctic continental shelf between Cape Colbeck at 158°W and Cape Adare at 170°E. In the austral winter, it is covered by a continuous sea ice cover as far north as 62°S. By February, at the height of the austral summer, the ice cover is reduced to a residual ice field northeast of the continental shelf (Jacobs and Comiso, 1989) and some perennial ice north of Oates and Pennell Coasts and at scattered locations along the coast of Victoria Land (Jeffries and Weeks, 1992). With the current interest in global climate change, its causes and its consequences, the role of the cryosphere is being closely scrutinized. The Ross Sea ice cover is a dynamic place where sea ice formation, modification and advection take part in the chain of interactions between the atmosphere, ice and ocean. Polynyas are maintained by upwelling of warm ocean waters (Jacobs and Comiso, 1989) or ice advection under consistent winds (Van Woert, 1998). Brine release from sea ice formation contributes towards the formation of Antarctic Bottom Water which is circulated globally (Jacobs and Amos, 1967). The high surface albedo of the ice floes reduces the amount of short wave radiation absorbed by the earth's surface. The effects of changes in the Ross Sea ice cover and its feedback to the global ocean and atmosphere circulation are not well understood. Sea ice thickness distribution, its variation and evolution in time and space are key variables in identifying the effects of climate change on the Ross Sea ice cover and in understanding the feedback of the Ross Sea ice cover to the climate system. Yet, fewer than ten ships traverse this 940 000 km^2 of the cryosphere each year. Due to its vastness and remoteness it is difficult to examine the time-varying characteristics of the Ross Sea ice cover in detail and over a broad scale simultaneously.

Over the years, description of the ice thickness distribution has been achieved through a combination of field sampling and remote sensing programs while understanding of the processes underlying observed phenomena has emerged from results of field observations, field and laboratory experiments and numerical modeling studies. Of the

different methods that are used to monitor ice thickness and extent of the Ross Sea ice cover, satellite remote sensing methods give the most comprehensive spatial and temporal coverages. However, to date, ice thickness cannot be directly estimated from microwave backscatter data. On the other hand, its estimation from radar and laser altimeter measurements of the surface elevation of ice floes seems promising (Laxon et al., 2002). With the current technology, drilling holes on ice floes still provides the most accurate estimates of sea ice thickness. In addition, examination of the crystal structure of the ice floes can reveal the processes that were involved in the formation of the sampled ice. However, sampling of ice floes from icebreakers or helicopters is an expensive operation and hence samples are limited in number, time and space. The samples can only be used to represent the ice conditions at the time and location of sampling although, as a result of ice drift, they contain characteristics acquired along their drift paths. Other remote methods which cover larger areas in space and time, make use of aircrafts, ships or moorings. The laser altimeter and the electromagnetic induction (EM) sounding instrument are often installed together on aircrafts or ships (Haas, 1998; Worby et al., 1999). The laser altimeter measures the distance to the top surface of the ice floe while the EM instrument measures the distance to the ice/water interface by making use of the large difference in electrical conductivity between sea ice and sea water. Sea ice thickness is derived from the difference between the measurements of the two instruments. Moored upward-looking sonars measure the distance from their locations underwater to the bottom surface of ice floes and to the sea surface. Since the majority of the volume of a floating ice floe is underwater, the amount of ice underwater, or the ice draft, is a good estimate of ice thickness. Moored upward-looking sonars have successfully obtained measurements of sea ice draft in the Weddell Sea over periods in excess of two years (Strass and Fahrbach, 1998). Ship-based visual observations require no special instrumentation and can be recorded by trained personnel onboard any vessel traversing the ice pack. Between 1980 and 1999, 14 000 observations have been recorded on 42 cruises in the Southern Ocean (Worby and Ackley, 2000).

There are two goals to this study. The first goal is to enhance our capability to estimate ice thickness remotely, especially from air- or space-borne altimetry and shipboard visual observations. Existing methodologies in the estimation of ice thickness from surface observations are improved and are then used to derive ice thickness from ship observations data obtained in the Ross Sea. Although these estimates are used to represent the characteristics of the ice cover at the time and location of the observations they contain characteristics acquired along their drift paths. Therefore, the second goal of this study is to examine the dynamic and thermodynamic processes involved in the development of the ice along its drift trajectory, prior to its observation during the icebreaker cruises.

Drill data from the Ross Sea obtained during three cruises in May 1995, May 1998 and January 1999, form the basis for the first part of the study. In Chapter 1, the ability to estimate ice thickness from altimetry measurements of top surface roughness and elevation is explored by examining the relationship between top surface roughness and thickness of Ross Sea ice floes. Chapters 2 to 4 focus on improving the existing methodology used in estimating ice thickness from ship observations data. Estimation of ice thickness from ship observations data depends on our understanding of the morphology and state of hydrostatic equilibrium of deformed ice features, including pressure ridges and rubble piles. There have been many studies of deformed ice features in the Arctic and the sub-arctic but there have been few studies of their counterparts in the Antarctic. In Chapter 2, a quantitative scheme, based on results from ice tank experiments conducted by other researchers, is developed specifically for identifying deformed ice features from drill profiles obtained in the Southern Ocean. Drill data from the cruises in the Ross Sea are augmented with similar data from the Amundsen, Bellingshausen and Weddell Seas and a first quantitative study of the morphology and state of hydrostatic equilibrium of deformed ice features in the Southern Ocean is presented in Chapter 3. Based on findings from Chapter 3, the existing methodology used to estimate ice thickness from ship observations is improved in Chapter 4. In Chapter 5, sea ice thickness is estimated from ship observations recorded during the two cruises in the Ross Sea in

May 1998 and January 1999, using the methodology developed in Chapter 4. In order to gain a wider spatial and temporal perspective on these estimates, a regional sea ice-mixed layer-pycnocline model is used to examine the dynamic and thermodynamic processes which determine the thickness of the observed ice along its drift trajectories prior to its observation during the cruises.

I am the first author in each of the five manuscripts included in this thesis. Each manuscript has been written in collaboration with my advisor, Martin Jeffries. In addition, Jukka Tuhkuri and Mikko Lensu from Helsinki University of Technology, Finland, co-authored Chapter 4, while Ralph Timmermann of Université Catholique de Louvain, Belgium, co-authored Chapter 5. In each case, I have instigated the projects and conducted the data analysis and composition of the text. All co-authors provided comments on subsequent drafts. Ralph Timmermann has further provided the computer code and technical support for the numerical model and initial data analysis routines.

REFERENCES

Haas, C. 1998. Evaluation of ship-based electromagnetic-inductive thickness measurements of summer sea-ice in the Bellingshausen and Amunsen Seas. *Cold Regions Science and Technology*, 27(1), 1-16.

Jacobs, S.S. and Amos, A. 1967. Physical and chemical oceanographic observations in the southern oceans. USS Eltanin cruises 16-21 1966-1967. *Lamont Geological Observatory of Columbia University, Technical Report No.1-CU-1-67.* Palisades, NY. 287p.

Jacobs, S.S. and Comiso, J.C. 1989. Sea ice and oceanic processes on the Ross Sea continental shelf. *Journal of Geophysical Research*, 94(C12), 18,195-18,211.

Jeffries, M.O. and Weeks, W.F. 1992. Structural characteristics and development of sea ice in the western Ross Sea. *Antarctic Science*, 5(1), 63-75.

Laxon, S., Wadhams, P., Dick, C. and Steffen, K. 2002. Recent variations in Arctic sea-

ice thickness. *Report to the Arctic Ocean Sciences Board by ACSYS/CliC Observation Products Panel.* IACPO Informal Report No. 7.

Strass, V.H. and Fahrbach, E. 1998. Temporal and regional variation of sea ice draft and coverage in the Weddell Sea obtained from upward looking sonars. *In*: M. O. Jeffries (ed.) Antarctic sea ice: physical processes, interactions and variability, 123-139.

Van Woert, M.L. 1999. Wintertime expansion and contraction of the Terra Nova Bay polynya *In*: Spezie, G. and Manzella, G.M.R. (eds.) Oceanography of the Ross Sea, Antarctica, 145-164. Springer-Verlag, Milan, Italy.

Worby, A.P., P.W. Griffin, V.I. Lytle and R.A. Massom, 1999. On the use of electromagnetic induction sounding to determine winter and spring sea ice thickness in the Antarctic. *Cold Regions Science and Technology*, 29(1), 49-58.

Worby, A.P. and Ackley, S.F. 2000. Antarctic research yields circumpolar sea ice thickness data. *Eos, Transactions, American Geophysical Union*, 81(17), 181, 184-185.

Chapter 1

Sea ice thickness and roughness in the Ross Sea, Antarctica*

1.1 ABSTRACT

Sea ice thickness and roughness data collected on three cruises in the Ross Sea, Antarctica showed interseasonal, regional and interannual variability. Variability was reduced to season, or age of ice floe, when sea ice roughness values from around Antarctica were compared. There were statistically significant correlations between mean snow elevation and mean ice thickness; snow surface roughness and mean ice thickness; and snow surface roughness and ice bottom roughness, which appeared to be independent of season, geographical location and deformation history of ice floes. Our field data indicates that ice thickness can be predicted from snow elevation measurements with higher accuracy in summer. The feasibility of using snow surface roughness to infer ice thickness and ice bottom roughness is promising, and can provide us with a means to study the thickness and underside of Antarctic sea ice at good spatial and temporal resolution.

1.2 INTRODUCTION

Sea ice thickness and roughness are important variables in the air-ice-ocean system. Changes in ice thickness affect energy exchange between ocean and atmosphere, and salt balance and light penetration of the upper ocean. Ice roughness modifies the air-ice and ice-ocean interfaces and affects ice drift and turbulent transfers of heat and momentum. Changes in thickness and ice mass can be used as signals for climate change.

Drilling holes is a reliable way to measure Antarctic sea ice thickness and derive its roughness (e.g., Adolphs, 1999; Andreas and others, 1993), but it is laborious and limited

---

* Tin, T. and M.O. Jeffries. 2001. Annals of Glaciology (33), 187-193.

to a small number of samples. Electromagnetic induction (EM) sounding, which makes use of the large difference in electrical conductivity between sea ice and sea water to detect the ice/water interface, provides a more efficient method to measure Antarctic sea ice thickness (Haas, 1998; Worby and others, 1999). EM sounding can be used on the ice surface or its coverage can be improved by suspending the instrument from an aircraft or icebreaker. The laser altimeter, which can also be operated from an airborne platform, has been used to describe the frequency and height distributions of Antarctic pressure ridge sails (Granberg and Leppäranta, 1999; Haas and others, 1999). However, it is not possible to derive ice thickness directly from altimetry measurements. With the projected launches of NASA's Ice, Cloud, and land Elevation Satellite (ICESat) and ESA's Cryosat, it will be possible to derive sea ice elevation and roughness data of high resolution and wide spatial and temporal coverages will be available. However, the ability to derive ice thickness from these and other airborne altimetry measurements depends on our knowledge of the relations between surface elevation, roughness and ice thickness.

Since ice thickness cannot be measured directly by laser altimeters, a number of studies have been conducted to infer ice thickness from quantities measured from the surface, primarily over Arctic sea ice. Using data obtained by drilling in multiyear ice, Ackley and others (1974) compared the ability of three isostatic models to predict ice thickness from surface elevations and reported that the error in the estimated thickness was only 10% greater than drilling-based operations. Wadhams and others (1992) studied concurrent laser profiling and submarine sonar records, and found that the probability density functions of snow elevation and ice draft could be related by a ratio of the density of ice plus snow and density of water.

In the Antarctic, there have been recent studies of the ratio between snow and ice thickness (Worby and others, 1996), and between snow elevation and ice draft (Adolphs, 1996). The present study augments those studies based on data obtained from drilling profiles with new drilling data obtained in autumn 1998 and summer 1999 in the Ross Sea, Antarctica. The focus of this paper is the operational feasibility of estimating ice

thickness and ice bottom surface roughness from snow surface measurements. Snow surface elevation is an obvious parameter, but its measurement by laser altimeters generally contains errors arising from uncertainty of flight altitude and estimation of sea levels (Ishizu and others, 1999). Hence we also examine snow surface roughness as a parameter for predicting ice thickness and ice bottom surface roughness, as roughness measures fluctuations about a mean value and is not affected by the accuracy of absolute snow elevation. With the new data, we are able to examine interannual (autumn 1995 and autumn 1998) and interseasonal (autumn 1995, 1998 and summer 1999) variations in sea ice roughness, and variations in the relationships between the snow surface and ice thickness and ice bottom surface roughness.

1.3 STUDY AREA AND FIELD METHODS

The data used in this study were obtained during three cruises on the R.V. Nathaniel B. Palmer (Fig. 1.1). Cruises NBP 95-3 and NBP 98-3 were in the western Ross Sea during austral autumn 1995 and 1998, respectively, and parts of their cruise tracks overlapped. NBP 99-1 was in the eastern Ross Sea during austral summer 1999. In all three studies, data were collected by drilling at 1 m intervals along 50 to 150 m long transects. Only transects ≥ 100 m in length were analysed. The number of transects and the total number of drill holes on each cruise are summarised in Table 1.1. At each drill hole, snow thickness (z_s) , ice thickness (z_i) and freeboard (z_f) were measured (Fig. 1.2). From these data, snow elevation ($h_s=z_s+z_f$) and draft ($z_d=z_i-z_f$) were calculated.

1.4 DATA AND ANALYSIS

1.4.1 Roughness variance

Roughness of the ice surface can be quantified by the roughness variance, $\sigma_x^{\,2}$ (Andreas and others, 1993). The roughness variance defined for an elevation variable, h_{xn} (where x

can be replaced by s to denote snow surface, t for ice top surface or b for ice bottom surface) is defined as

$$\sigma_x^2 = \frac{1}{N}\sum_{n=1}^{N}(h_{xn} - \bar{h}_x)^2 \tag{1.1}$$

where $\bar{h}_x$ is the mean elevation (distance from sea level) of surface x, N is the number of points on the transect and σ_x is the root-mean-square (rms) elevation roughness.

1.4.2 Data reduction

Ridges on each floe were distinguished from unridged ice (Fig. 1.2) using methods similar to those applied to submarine sonar profiles under Arctic ice (Wadhams and Horne, 1980). Modifications were made for the NBP Ross Sea data sets as they were shorter in length, contained thinner ice and contained more high frequency fluctuations. A ridge was defined by the presence of a ridge keel underwater (Fig. 1.2). The Rayleigh criterion defines a pressure ridge keel as one where the draft minima (troughs) on either side of the local maximum (crest) descend at least halfway toward the local level ice. In the present analysis, overlapping keels were considered as part of the same ridge. Local level horizon was defined using the D2 definition (Wadhams and Horne, 1980). A level ice point is one whose draft differs by less than 0.25 m from every point within 10 m on either side. A ridge keel must also be deeper than a minimum draft, called the cutoff value; 5 m and 9 m cutoffs were frequently used for the Arctic sonar profiles. These values were inappropriate for the NBP Ross Sea data set, since the maximum draft measured was only 2.5 m and the mean draft was 0.80 m. The size difference between Arctic and Antarctic ridges was also noted by Worby and others (1996), who reduced the cutoff heights for ridge sails to 0.5 m from the usual values of 0.75 – 1 m to allow for the smaller ridges in the Amundsen and Bellingshausen Seas. We tested the NBP Ross Sea data set with cutoff values of 1 m, 0.75 m and 0.5 m for ridge keels. We found that cutoff values of 0.75 m and 1 m missed a significant portion of ridges (72% and 55%

respectively) while a cutoff value of 0.5 m captured 80% of the ridges. Hence, we adopted the definition that a ridge keel is an underwater feature which satisfies the Rayleigh criterion and is at least 0.5 m deep.

Each identified ridge is represented as an individual data point in the following analysis. Once the ridges were removed, each one of the remaining regions is classified as unridged ice (Fig. 1.2) and is represented as an individual data point.

1.5 RESULTS

1.5.1 Mean thickness and roughness

The mean thickness and roughness values were reasonably similar for the two autumn cruises (NBP 95-3 and NBP 98-3) and these cruises were dissimilar from the summer cruise (NBP 99-1) (Table 1.2). Summer ice was thicker and had a deeper snow cover. As a result of the heavy snow load, the summer snow/ice interface was often submerged below sea level and mean summer freeboard was –0.04 m. The roughness of the summer ice and snow surfaces were around twice as great as those of autumn ice. For the autumn cruises, there was slightly thicker ice, thinner snow and rougher surfaces in 1998 than in 1995.

Ridges contained thicker ice, deeper snow and rougher ice bottom surfaces than unridged regions (Table 1.2). At the ice bottom surface, ridges were nearly four times as rough as unridged regions, but ice top surface and snow surface were similar in roughness. Mean freeboards of both ridges and unridged regions were at or close to zero.

1.5.2 Linear regressions

Linear regressions were performed between mean snow elevation, h_s, and mean ice thickness, z_i (Figs. 1.3a-f); snow surface roughness, σ_s, and mean ice thickness, z_i (Figs. 1.4a-f); snow surface roughness, σ_s, and ice bottom roughness, σ_b (Figs. 1.5a-f); and snow

surface roughness, σ_s, and ice top surface roughness, σ_t (Figs. 1.6a-c). The majority of correlations are significant at the 99% confidence level.

Cruises varied in the strength of correlation between each pair of variables. For example, correlation between h_s and z_i was considerably stronger in NBP 99-1 than in NBP 95-3 or NBP 98-3 (Figs. 1.3a-c); correlation between σ_s and z_i was stronger in NBP 95-3 and NBP 98-3 than in NBP 99-1 (Figs. 1.4a-c); and scatter between σ_s and σ_b was considerable on all three cruises (Figs. 1.5a-c). However, for each pair of variables, the data points from all three cruises converge relatively well along a linear trend (Figs. 1.3d, 1.4d and 1.5d). The strongest correlation was between h_s and z_i (R~0.85, Fig. 1.3d) while the correlations between σ_s and z_i (Fig. 1.4d), and σ_s andσ_b (Fig. 1.5d) were slightly weaker and similar in strength (R~0.71). Despite the similarity in correlation coefficients, scatter between σ_s and σ_b was considerably greater than between σ_s and z_i.

Regressions for ridges and unridged regions differed among the variable pairs. There was stronger correlation between h_s and z_i for both ridges and unridged regions (Figs. 1.3e-f). Weaker correlation and large data scatter were found for both ridges and unridged regions between σ_s and z_i, σ_s andσ_b, σ_s and σ_t (Figs. 1.4e-f, 1.5e-f and 1.6b-c), with the correlation being considerably stronger over ridges than unridged regions.

1.6 DISCUSSION

1.6.1 Mean thickness and roughness

Interseasonal, regional and interannual variations were observed in the thickness and roughness of Ross Sea ice. Ice and snow were thicker and surfaces were rougher in NBP 99-1 than in NBP 95-3 and NBP 98-3. The autumn ice in NBP 95-3 and NBP 98-3 contained a higher fraction of thin, new ice than the summer ice in NBP 99-1. By the summer, the ice cover had had time to thicken both dynamically and thermodynamically, and to accumulate snow. NBP 99-1 took place in the eastern Ross Sea where winds are more variable and ice export is less effective than in the western Ross Sea (Marshall and

Turner, 1997), where katabatic winds of high directional constancy and the cyclonic circulation of the Ross Sea maintain efficient ice export (Jacobs and Comiso, 1989). Consistently high concentrations of sea ice (Sturman and Anderson, 1986) and variable winds (Marshall and Turner, 1997) in the eastern Ross Sea promote dynamic thickening and roughening of ice surfaces. The snow surface in this region could also roughen as a result of variable winds, floe rotation (Massom and others, 1997) and increased ice deformation. Interannual variability was observed between NBP 95-3 and NBP 98-3, which took place in the same season and similar geographical locations, with 1998 being a year of less snow accumulation and greater ice thickness and roughness.

Ridges and unridged regions exhibited different characteristics, with ridges having a rougher ice bottom, greater ice thickness and accumulating more snow. Despite the differences in snow loading and ice stresses, isostatic balance was maintained across both ridges and unridged regions, as reflected by their mean freeboards of zero.

1.6.2 Comparison of surface roughness with other Antarctic regions

Sea ice roughness values from various studies were compared according to geographical location, season and ice type (Table 1.3). Roughness values fell into two categories according to the age of ice floes. Early season (autumn to spring) first year ice was low in roughness (Table 1.3). Late season (summer) first year ice was similar to multiyear ice (Table 1.3) where roughness was up to 3 times that of early season first year ice. From NBP 95-3, NBP 98-3 and NBP 99-1, we observed interannual, regional and interseasonal variability in sea ice roughness (Table 1.2). When the comparison was expanded to include 8 other cruises from previous studies in other parts of Antarctica, we found that interseasonal variations stood out over interannual and regional variability for first year ice (Table 1.3). For the multiyear ice in the western Weddell Sea, roughness values were consistent among measurements made in different years and seasons (Table 1.3). This suggests that processes which create sea ice roughness are independent of year and location, and that ice floe age and deformation history are the most important factors in

determining roughness.

1.6.3 Linear regression

In the linear regressions between h_s and z_i; σ_s and z_i; and σ_s and σ_b, we observed variations between cruises and over ridges and unridged regions (Figs. 1.3a-f, 1.4a-f and 1.5a-f). Despite the differences in data scatter and linear regression, a good linear trend emerged for each pair of variables when all profiles from the cruises were combined. This suggests that processes maintaining the relationships between snow elevation and ice thickness; snow surface roughness and ice thickness; and snow surface roughness and ice bottom roughness, are independent of season, year, location and deformation history of the ice floes.

Correlation between h_s and z_i over ridges and unridged regions (Figs. 1.3e-f) were stronger than correlations between σ_s and z_i (Figs. 1.4e-f), and σ_s and σ_b (Figs. 1.5e-f). This difference is primarily due to the different mechanisms that determine h_s and σ_s.

1.6.3.1 Mean snow elevation, h_s

The stronger correlation between h_s and z_i in NBP 99-1 as compared to NBP 95-3 and NBP 98-3 can be attributed to the presence of slush. Slush is the layer of saturated snow between the snow/ice interface and the sea level on a flooded ice floe, where $z_f < 0$. As explained below, slush enhances the capability of predicting z_i from h_s by separating h_s from z_i, and by making little contribution to buoyancy.

The isostatic balance of a non-flooded ice floe ($z_f \geq 0$) is as follows:

$$\rho_s z_s + \rho_i z_f = z_d(\rho_w - \rho_i) \qquad \text{for } z_f \geq 0 \qquad (1.2)$$

where ρ_s is the density of snow, ρ_i is the density of sea ice (assumed to be 900 kg m^{-3}, Massom and others, 1998), and ρ_w is the density of seawater (1024 kg m^{-3}). Mean ρ_s

values for NBP 95-3, NBP 98-3 and NBP 99-1 were 340, 320 and 520 kg m^{-3} respectively (Sturm and others, 1998; Morris and Jeffries, 2001). Isostatic balance in a non-flooded ice floe is maintained between h_s ($=z_s+z_f$), which contains snow and some ice, and z_d. Translation between z_d and z_i also depends on the isostatic balance and the multiple dependencies make the relationship between h_s and z_i complex and scattered.

The isostatic balance of a flooded ice floe ($z_f<0$) is as follows:

$$\rho_s(z_s + z_f) = z_i(\rho_w - \rho_i) + z_f(\rho_w - \rho_{sl}) \qquad \text{for } z_f < 0 \qquad (1.3)$$

where z_f here indicates the thickness of the slush layer and ρ_{sl} is density of slush, which is estimated to be close to that of seawater (0.96 kg m^{-3}) (Adolphs, 1998), although field measurements arrive at lower values (0.70 kg m^{-3}) (Adolphs, 1998) as seawater is invariably lost during the measurement procedure. The small difference between ρ_{sl} and ρ_w means that the effect of slush on buoyancy is small. As a result, the isostatic balance is maintained between h_s and z_i, allowing z_i to be predicted effectively from h_s.

Variability in the ratio z_i : h_s can be explained by the differences in the relative densities and proportions of ice and snow above sea level. We observed a higher z_i : h_s ratio in NBP 99-1 (4:1) than in NBP 98-3 (3:1), which was, in turn, higher than in NBP 95-3 (2:1, Figs. 1.2a-c). Snow density in NBP 99-1 was highest, being 1.5 times greater than in NBP 95-3 and NBP 98-3. For the same h_s, the heavier load in NBP 99-1 required a greater buoyancy force created by a larger ice volume below the sea level. Hence the ratio of z_i : h_s was greatest in NBP 99-1. Between NBP 95-3 and NBP 98-3, there was only 6% difference in ρ_s, and h_s was the same for both years. However, there was 0.02 m more ice freeboard in NBP 98-3 than in NBP 95-3, and since the ice was three times more dense than snow, the load for the same h_s increased. An increased load required a larger ice volume to provide the buoyancy force and hence the z_i : h_s ratio was greater in NBP 98-3 than in NBP 95-3.

1.6.3.2 Snow surface roughness, σ_s

Snow surface roughness is primarily determined by ice top surface topography and wind redistribution. Snow preferentially collects in depressions. Winds at speeds greater than 6-8 m s^{-1} are able to redistribute the snow (Andreas and Claffey, 1995), building it up in the lee of sails, filling in between sails and keeping the tops of sails bare (Lange and Eicken, 1991). A snow surface with a hard crust would require higher winds to initiate redistribution (Andreas and Claffey, 1995). Snow drifts on ice floes are often omnidirectional because of floe rotation and changes in prevailing wind direction (Massom and others, 1997). The snow surface amplifies the roughness of the ice top surface and the amplification is stronger in unridged regions than in ridges (Fig. 1.6a-c). Analysis of the frequency of snow surface roughness reveals that, although the magnitude of ice roughness has been amplified, the frequency of roughness features has been decreased, resulting in a smoothing effect over the ice top surface (Andreas and Claffey, 1995, Massom and others, 1997).

The poor correlation between σ_s and z_i and σ_b over unridged regions (Figs. 1.4e and 1.5e) can be attributed to the large discrepancy between σ_s and σ_t decoupling the snow surface from the processes determining z_i and σ_b. Why does a large discrepancy between σ_s and σ_t exist in the unridged regions and not in ridges (Figs. 1.6b,c)? We suggest that the modification of ice top surface roughness, effects of nearby ridges and nucleation of roughness features on the snow surface are possible reasons. After the snow cover has been laid down, ice top surface can be smoothed by formation of snow ice. Snow ice is formed by the freezing of snow and floodwater at the interface between snow and ice, and this new ice layer smooths out small perturbations on the ice top surface, thereby reducing σ_t. Hence, σ_t that is measured subsequent to snow ice formation is less than the value when the snow cover was first laid down (Worby and others, 1996). In ridges, σ_t is dominated by the crest of the keel or sail, with its large deviation from the mean surface. Flooding and subsequent smoothing of troughs by the growth of snow ice has a relatively small effect on the σ_t over the entire ridge.

Wind redistributes snow so that it builds up in the lee of ridge sails, and snow drifts have been observed up to 10 m away from a ridge (Sturm and others, 1998). The roughness of this wind-drifted snow is independent of the ice top surface roughness. As a result, σ_s and σ_i are decoupled close to ridges and unridged regions can have a disproportionately large σ_s. On flat level ice surface, σ_s can also be decoupled from σ_i, as small icy nodules with sub-centimeter diameters can act as the foci for the formation of extensive dune features which can be up to 1m high and 35m long (Massom and others, 1997; Sturm and others, 1998).

1.7 CONCLUSIONS

Interseasonal, regional and interannual variations were observed in the thickness and roughness of Ross Sea ice. Variability was reduced to season, or age of ice floe, when sea ice roughness values from around Antarctica were compared. This suggests that processes which create sea ice roughness are independent of year and location, and that ice floe age and deformation history are the most important components in determining roughness. We found statistically significant correlations between mean snow elevation and mean ice thickness; snow surface roughness and mean ice thickness; and snow surface roughness and ice bottom roughness, over profiles of ≥100m in length. The correlations appeared to be independent of season, location and deformation history of ice floes. The predictive capability of snow elevation and snow surface roughness is promising. The presence of slush improves the capability to predict ice thickness from snow surface elevation by keeping all ice below sea level and by making little contribution to buoyancy.

To improve and further understand the predictive capability of snow elevation and snow surface roughness, more data in the high thickness and roughness range (mean ice thickness > 1.5 m, snow surface roughness > 0.15 m and ice bottom roughness > 0.75 m) is needed. Monitoring the effects of wind on snow surface roughness and the modification of the ice top surface through the season will improve our understanding of

the mechanisms which determine snow surface roughness. Finally, similar studies in other parts of the Southern Ocean can tell us whether a single relationship between snow elevation and snow surface roughness with ice thickness and ice bottom roughness can be applied for all ice covered waters in Antarctica. The bottom surface of Antarctic sea ice has only been studied by moored upward looking sonars (Strass and Fahrbach, 1998) or by drilling profiles (e.g., Lange and Eicken, 1991; Worby and others, 1996) and data are limited in spatial coverage. Unless autonomous underwater vehicles or civilian submersibles become available for research under the Antarctic sea ice cover, the established methods are the only ways to directly obtain information on ice thickness, ice bottom roughness and ice bottom topography. The ability to predict subsurface quantities from airborne or even spaceborne measurements will provide us with an indirect method that has good spatial and temporal coverage to study the thickness and underside of Antarctic sea ice.

1.8 ACKNOWLEDGEMENTS

This work was supported by NSF grants OPP 9316767 and OPP 9614844. We are grateful to the many members of the science teams and Antarctic Support Associates personnel who dug snow, drilled holes and made measurements. We also thank Captain Joe Borkowski, the officers and crew of the R.V. Nathaniel B. Palmer for their vital contribution. Thanks also to reviewers C. Haas and S. Ackley, and editor T. Tucker for providing invaluable suggestions that helped to improve the paper.

1.9 FIGURES

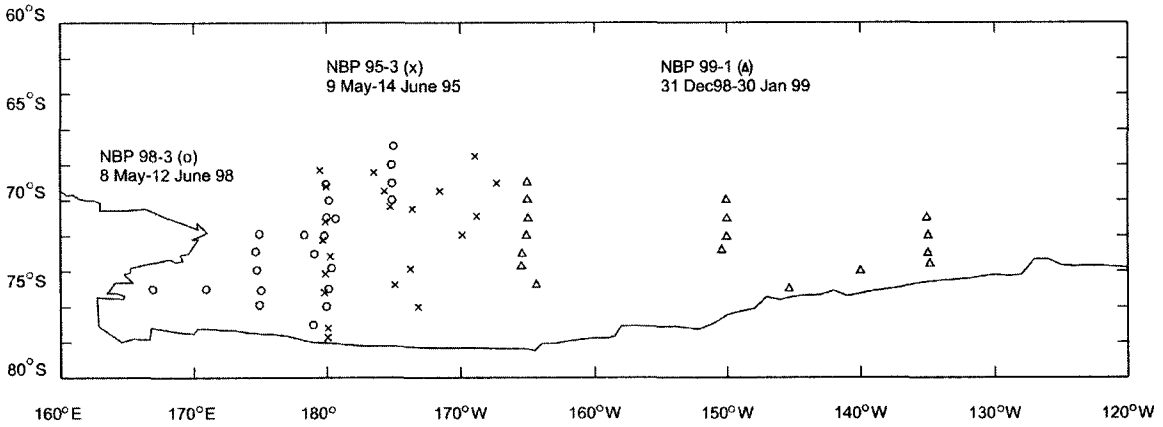

Figure 1.1 Cruise tracks of NBP 95-3, NBP 98-3 and NBP 99-1 in the Ross Sea.

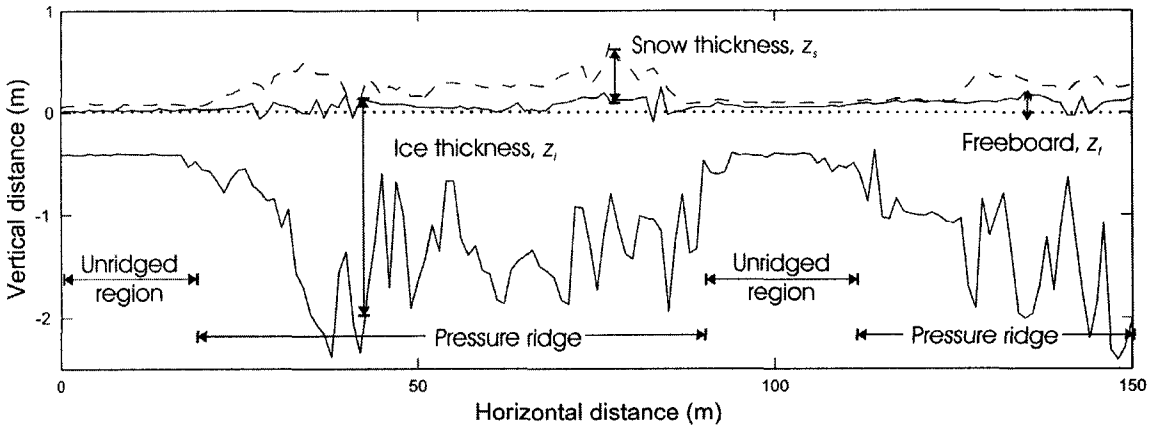

Figure 1.2 A typical snow depth and ice thickness profile obtained during NBP 98-3. Annotations indicate quantities and features described in the text.

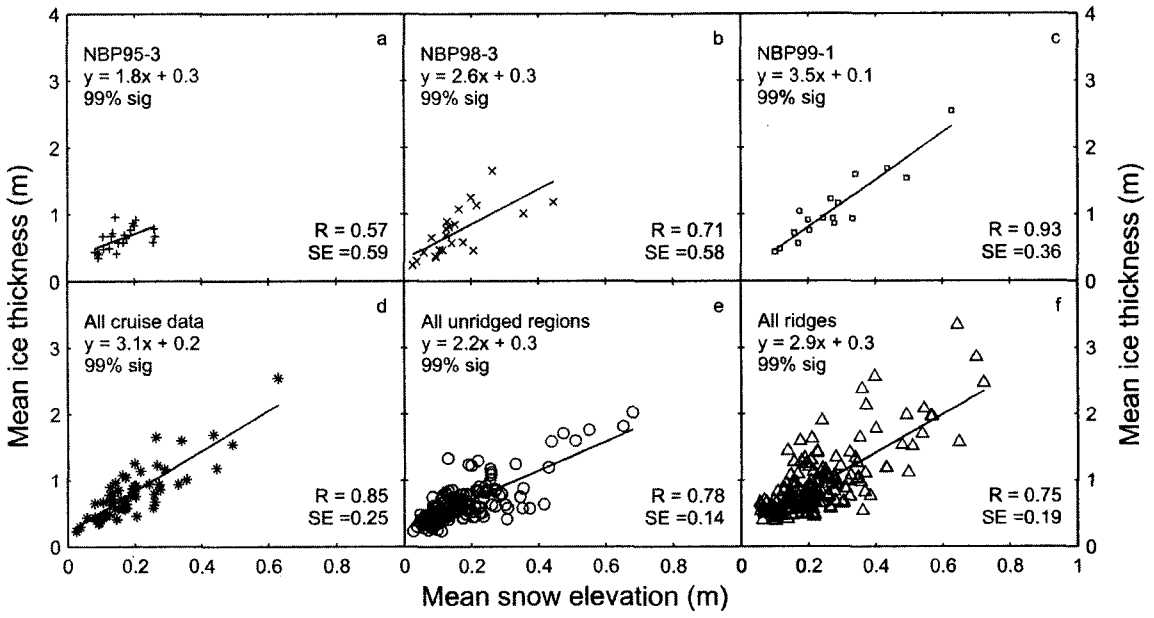

Figure 1.3 Linear regression between mean snow elevation and mean ice thickness. (a)-(c) roughnesses averaged over each entire profile for individual cruises; (d) linear regression of all cruise data combined; (e) and (f) roughnesses over individual unridged regions and ridges respectively. The correlation coefficient (R), the significance level (% sig) and the standard error (SE) of the slope of the regression are given in each graph. Plus/minus 2SE corresponds to 95% confidence interval of the regression.

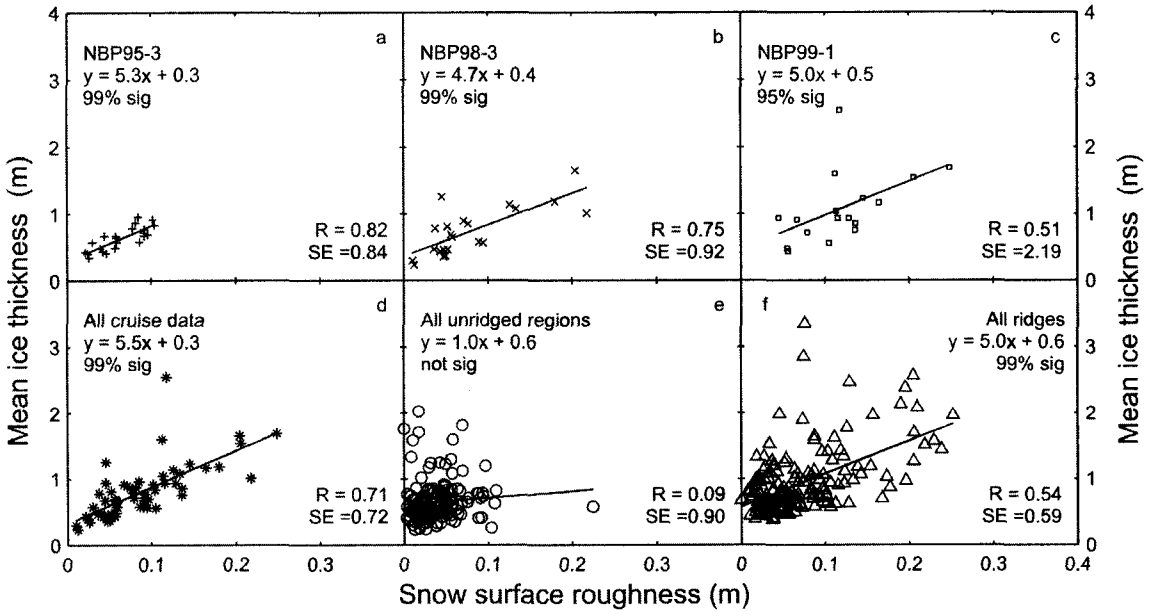

Figure 1.4 Linear regression between snow surface roughness and mean ice thickness. (a)-(c) roughnesses averaged over each entire profile for individual cruises; (d) linear regression of all cruise data combined; (e) and (f) roughnesses over individual unridged regions and ridges respectively.

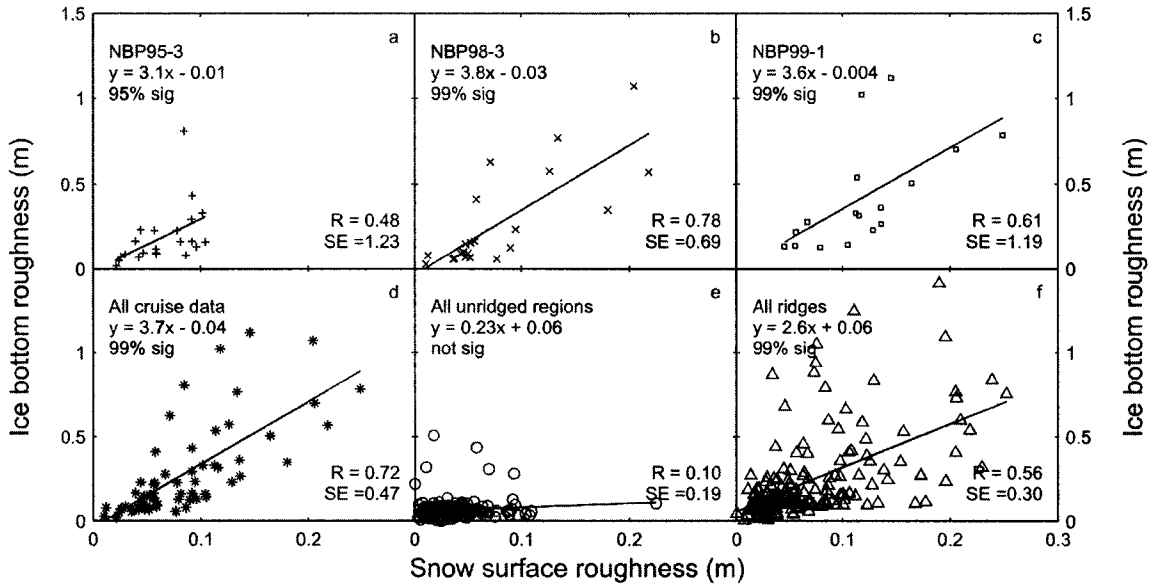

Figure 1.5 Linear regression between snow surface roughness and ice bottom roughness. (a)-(c) roughnesses averaged over each entire profile for individual cruises; (d) linear regression of all cruise data combined; (e) and (f) roughnesses over individual unridged regions and ridges respectively.

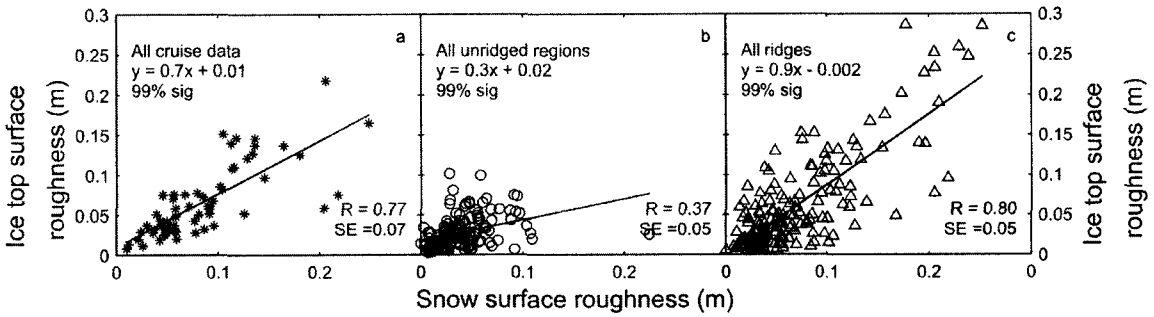

Figure 1.6 Linear regression between snow surface roughness and ice top surface roughness (σ_i). (a) linear regression of all cruise data combined; (b) and (c) roughnesses over individual unridged regions and ridges respectively.

1.10 TABLES

Table 1.1 Summary of drilling operations

Cruise	Number of transects	Number of drill holes
NBP 95-3	22	2221
NBP 98-3	22	3131
NBP 99-1	17	2517

Table 1.2 Mean values of snow and ice thickness and roughness of ice floes.

	NBP 95-3 Autumn 1995	NBP 98-3 Autumn 1998	NBP 99-1 Summer 1999	All unridged regions	All ridges
Snow thickness, z_s (m)	0.14	0.12	0.32	0.17	0.22
Snow elevation, h_s (m)	0.16	0.16	0.28	0.17	0.23
Freeboard, z_f (m)	0.02	0.04	-0.04	0.00	0.01
Ice thickness, z_i (m)	0.63	0.74	1.08	0.65	0.92
Snow surface roughness, σ_s (m)	0.06	0.08	0.12	0.04	0.07
Ice bottom surface roughness, σ_b (m)	0.19	0.27	0.42	0.07	0.23
Ice top surface roughness, σ_t (m)	0.04	0.05	0.12	0.03	0.06

Table 1.3 Comparison of rms snow and sea ice roughness values in Antarctica. Studies in italics contain early season first year ice. Studies in bold contain late season first year ice and multiyear ice.

				Rms roughness		
Reference	Location	Season	Ice types	Snow surface, σ_s (m)	Ice bottom surface, σ_b (m)	Ice top surface, σ_t (m)
NBP Ross Sea data set of the present study						
NBP 95-3	*Ross Sea (West)*	*Autumn*	*First Year*	*0.06*	*0.19*	*0.04*
NBP 98-3	*Ross Sea (West)*	*Autumn*	*First Year*	*0.08*	*0.27*	*0.05*
NBP 99-1	**Ross Sea (East)**	**Summer**	**First Year**	**0.12**	**0.42**	**0.12**
Previous studies						
Fisher and Lytle, 1998[1].	*Weddell Sea (East)*	*Winter*	*First Year*	*0.07*	-	*0.04*
Adolphs, 1999[a].	*Ross, Amundsen and Bellingshausen Seas*	*Winter*	*First Year*	*0.08*	*0.25*	*0.04*
Andreas and other, 1993[a].	*Weddell Sea (East and West)*	*Spring*	*First Year*	*0.09*	*0.27*	*0.07*
Fisher and Lytle, 1998[2]**.**	**Weddell Sea (West)**	**Autumn**	**Multiyear**	**0.13**	-	**0.09**
Fisher and Lytle, 1998[3]**.**	**Weddell Sea (West)**	**Autumn**	**Multiyear (single floe)**	**0.12**	-	**0.12**
Andreas and other, 1993[a]**.**	**Weddell Sea (West)**	**Spring**	**Multiyear**	**0.08**	**0.38**	**0.13**

[1] Referred to as NBP 94 in Fisher and Lytle, 1998.

[2] Referred to as NBP 92 in Fisher and Lytle, 1998.

[3] Referred to as ISW in Fisher and Lytle, 1998.

[a] Mean values estimated from graphs.

1.11 REFERENCES

Ackley, S.F., W.D. Hibler III, F.K. Kugzruk, A. Kovacs and W.F. Weeks. 1976. Thickness and roughness variations of Arctic multi-year sea ice. *CRREL Rep.* 76-18.

Adolphs, U. 1998. Ice thickness variability, isostatic balance and potential for snow ice formation on ice floes in the south polar Pacific Ocean. *J. Geophys. Res.*, **103**(C1), 24,675-24,691.

Adolphs, U. 1999. Roughness variability of sea ice and snow cover thickness profiles in the Ross, Amundsen, and Bellingshausen Seas. *J. Geophys. Res.*, **104**(C6), 13,577-13,591.

Andreas, E.L. and K.J. Claffey. 1995. Air-ice drag coefficients in the western Weddell Sea 1. Values deduced from profile measurements. *J. Geophys. Res.*, **100**(C3), 4821-4831.

Andreas, E.L., M.A. Lange, S.F. Ackley and P. Wadhams. 1993. Roughness of Weddell Sea ice and estimates of the air-ice drag coefficient. *J. Geophys. Res.*, **98**(C7), 12,439-12,452.

Fisher, R. and V.I. Lytle. 1998. Atmospheric drag coefficients of Weddell Sea ice computed from roughness profiles. *Ann. Glaciol.*, **27**, 455-460.

Granberg, H.B. and M. Leppäranta. 1999. Observations of sea ice ridging in the Weddell Sea, *J. Geophys. Res.*, **104**(C11), 25,735-25,745.

Haas, C. 1998. Evaluation of ship-based electromagnetic-inductive thickness measurements of summer sea-ice in the Bellingshausen and Amunsen Seas. *Cold Reg. Sci. Technol.*, **27**(1), 1-16.

Haas, C., Q. Liu and T. Martin, 1999. Retrieval of Antarctic sea-ice pressure ridge frequencies from ERS SAR imagery by means of in-situ laser profiling and usage of a neural network. *Int. J. Rem. Sens.*, **20**(15&16), 3111-3123.

Ishizu, M., K. Mizutani and T. Itabe. 1999. Airborne freeboard measurements of sea ice and lake ice at the Sea of Okhotsk coast in 1993-5 by a laser altimeter. *Int. J. Remote Sensing*, **20**(12), 2461-2476.

Jacobs, S.S. and J.C. Comiso. 1989. Sea ice and oceanic processes on the Ross Sea continental shelf. *J. Geophys. Res.*, **94** (C12), 18195-18211.

Lange, M.A. and H. Eicken. 1991. The sea ice thickness distribution in the northwestern Weddell Sea. *J. Geophys. Res., 96(C3), 4821-4837.*

Marshall, G.J. and J. Turner. 1997. Katabatic wind propagation over the western Ross Sea observed using ERS-1 scatterometer data. *Antarct. Sci.*, **9**(2), 221-226.

Massom, R.A., M.R. Drinkwater and C. Haas. 1997. Winter snow cover on sea ice in the Weddell Sea. *J. Geophys. Res.*, **102**(C1), 1101-1117.

Massom, R.A., V.I. Lytle, A.P. Worby and I. Allison. 1998. Winter snow cover variability on East Antarctic sea ice. *J. Geophys. Res.*, **103**(C11), 24,837-24,855.

Morris, K. and M.O. Jeffries, 2001. Seasonal contrasts in snow cover characteristics on Ross Sea ice floes. *Ann. Glaciol.*, **33**, 61-68.

Strass, V.H. and E. Fahrbach. 1998. Temporal and regional variation of sea ice draft and coverage in the Weddell Sea obtained from upward looking sonars. *In* Jeffries M.O., *ed. Antarctic sea ice: physical processes, interactions and variability.* Washington, DC, American Geophysical Union, 123-139. (Antarctic Research Series 74.)

Sturm, M., K. Morris and R. Massom. 1998. The winter snow cover of the west Antarctic pack ice: its spatial and temporal variability. *In* Jeffries M.O., *ed. Antarctic sea ice: physical processes, interactions and variability.* Washington, DC, American Geophysical Union, 1-18. (Antarctic Research Series 74.)

Sturman, A.P. and M.R. Anderson. 1986. On the sea-ice regime of the Ross Sea, Antarctica. *J. Glaciol.*, **32**(110), 54-59.

Wadhams, P. and R.J. Horne. 1980. An analysis of ice profiles obtained by submarine sonar in the Beaufort Sea. *J. Glaciol.*, **25**(93), 401-424.

Wadhams, P., W.B. Tucker III, W.B. Krabill, R.N. Swift, J.C. Comiso and N.R. Davis. 1992. Relationship between sea ice freeboard and draft in the Arctic basin, and implications for ice thickness monitoring. *J. Geophys. Res.*, **97**(C12), 20,325-20,334.

Williams, E., C. Swithinbank and G. de Q. Robin. 1975. A submarine sonar study of

Arctic pack ice. *J. Glaciol.*, **15**(73), 349-362.

Worby, A.P., M.O. Jeffries, W.F. Weeks, K. Morris and R. Jaña. 1996. The thickness distribution of sea ice and snow cover during late winter in the Bellingshausen and Amundsen Seas, Antarctica. *J. Geophys. Res.*, **101**(C12), 28441-28455.

Worby, A.P., P.W. Griffin, V.I. Lytle and R.A. Massom, 1999. On the use of electromagnetic induction sounding to determine winter and spring sea ice thickness in the Antarctic. *Cold Reg. Sci. Tech.*, **29**(1), 49-58.

Chapter 2

Quantitative identification of Antarctic first year pressure ridges*

2.1 ABSTRACT

We developed a quantitative scheme for identifying Antarctic first year ridge sails and keels from 204 drill profiles obtained from the Weddell, Ross, Amundsen and Bellingshausen Seas. A sail is defined as a non-level section on the top surface which has at least one point which is >0.3m above the surrounding level top surface. A keel is defined as a non-level section on the bottom surface which has at least one point which is >2.25 times as thick as the surrounding mean level ice thickness. From nearly 19km of drill data we identified 48 ridges. Almost 65% of them are not associated with any sails, while a small proportion overlap with two sails. The ratio between maximum snow sail height and maximum ice keel depth is 1:3.6. Estimating the volume of a ridge by assuming it has the same thickness as the surrounding level ice, underestimates the total ice mass by approximately 40%. Estimation of mass contained within keels from snow sail statistics must take into account the probability of a keel being associated with a sail and the ratios between the snow sail and ice keel.

2.2 INTRODUCTION

Pressure ridges are deformation features in the sea ice cover which contain a significant amount of ice mass. Knowledge of their morphology and improvement in their detection will aid in our estimation of the ice thickness distribution, parameterization of sea ice variables in climate models and choice of shipping routes. The Antarctic Sea-Ice

---

* Tin, T. and M.O. Jeffries. 2001. Proceedings of 16th International Conference on Port and Ocean Engineering under Arctic Conditions, Aug. 12-17, 2001, Ottawa, ON, Canada. Vol.3, 1455-1464.

Processes and Climate (ASPeCt) programme has been promoting a standardized ice observation protocol for collecting data on snow and ice thicknesses from ships traveling through the ice pack (Worby and Ackley, 2000). An accurate estimation of the ice thickness distribution depends on the ability to use observations of ridge sail statistics and level ice thickness to estimate the mass contained within ridge keels. The formulation currently used for estimating keel mass has been developed from snow and ice thickness data of ridges identified visually from nine drill profiles from the East Antarctic ice pack (Worby and Allison, 1999). The objective of our study is to verify and extend this formulation with data from 204 drill profiles from the Weddell, Ross, Amundsen and Bellingshausen Seas. Our results will be useful for interpreting top surface measurements, including airborne laser profiling as well as ship observations. The focus of this paper is to prepare the groundwork by developing a quantitative scheme to identify first year ridge sails and keels unambiguously from drill data, and to present preliminary results on the morphology of first year Antarctic pressure ridges.

2.3 DATA

The data used for this study were obtained by drilling on ice floes. Drilling was conducted along line transects, each 50m to 150m in length. The transects were set out to sample features representative of the surrounding ice cover. Holes were drilled at 1m intervals, and snow depth, ice thickness and freeboard were measured. Only data collected on first year floes along transects ≥50m in length are used. This amounts to approximately 19km of drill data from 8 cruises (Table 2.1).

2.4 EXISTING RIDGE IDENTIFICATION SCHEMES

Pressure ridge studies can be roughly divided into the morphology or the counting categories. In a ridge morphology study, a ridge is identified visually from a prominent sail on the top surface of the ice, prior to data collection. This is followed by extensive drilling or other surveying measurements to provide data on the shapes, dimensions and relationships between sail and keel. Numerous studies have been conducted in the Arctic Ocean and the Baltic Sea, over first year ridges (e.g., Høyland and Løset, 1999; Kankaanpää, 1997), multi-year ridges (e.g., Timco and Burden, 1997; Weeks et al., 1971) and rubble fields (Melling et al., 1993).

In a ridge counting study, ridges are identified quantitatively from either laser altimeter measurements of the top surface or submarine sonar measurements of the bottom surface. Ridges are counted to derive statistics on the distribution of ridges. Numerous studies have been conducted above and below the Arctic ice cover (e.g., Hibler et al., 1972; Wadhams et al., 1992). To date, Antarctic ridges have only been quantified from above (e.g., Haas et al., 1999; Granberg and Leppäranta, 1999). The Rayleigh criterion has been the most commonly used quantitative identification scheme. According to this criterion, an individual ridge sail or keel is a feature containing a crest (a local maximum) enclosed by troughs (local minima) on both sides which descend at least half way towards the local level ice horizon (Lowry and Wadhams, 1979). In addition, the sail (or keel) must be higher (or deeper) than a cutoff value.

In order to apply the Rayleigh criterion, the local level ice horizon needs to be defined. Three methods have been used on submarine sonar data for this purpose. The most straightforward method is to assume that a fixed quantity applies to the entire data track. Wadhams and Horne (1980) arbitrarily chose a draft of 2.5m as the level ice horizon for 1400km of submarine sonar data obtained in the Beaufort Sea. The other two methods iteratively compare the difference in draft between points against a height limit, H, and a point of interest (POI) is considered as non-level if the height limit is exceeded.

In what we will call the Implicit Gradient method, the difference in draft is assessed

between two points across a gauge length, D, essentially testing against an implied gradient of H/D. Williams et al. (1975) found that a gauge length of 8m, centered on the POI, testing against an implied gradient of 0.025, was optimal for defining level ice from their 10km long sections of submarine sonar data obtained from the Arctic Ocean. According to this definition, a POI at x m along the transect, with a draft of $h(x)$, is non-level if

$$\left|h\left(x+\frac{D}{2}\right)-h\left(x-\frac{D}{2}\right)\right| \geq H \tag{2.1}$$

where D = 8m and H = 0.2m.

Wadhams and Horne (1980) relaxed this definition by increasing the gauge length and placing the POI at the end of it. A POI at x m along their 50km long sections obtained from the Beaufort Sea is non-level if

$$|h(x+D)-h(x)\geq H| \quad \text{or} \quad |h(x-D)-h(x)\geq H| \tag{2.2a, 2.2b}$$

where D = 10m and H = 0.25m.

This essentially tests against an implied gradient of 0.025 on either side of the POI.

In what we will call the Every Point method, the difference in draft is assessed between the POI and every point within a guage length range, d. A POI at x m is non-level if

$$|h(x+d)-h(x)\geq H| \tag{2.3}$$

where d = -10 to +10 m and H = 0.25m (Wadhams and Horne, 1980).

This is equivalent to testing an implied gradient decreasing from 0.25 towards 0.025 with increasing distance from the POI. It is considered to be a more stringent scheme

(Wadhams and Horne, 1980), whereby it does not see all the level ice but the ice that it sees is almost certainly level ice, i.e., the scheme is not exhaustive but is precise.

A cutoff value is chosen to exclude small scale surface features which are not associated with pressure ridging. In submarine sonar studies under the Arctic ice cover, 5m and 9m have been used as cutoff drafts for keel identification (Davis and Wadhams, 1995). In laser profiling studies, sail cutoff heights have ranged from 0.3m over the Baltic Sea (Leppäranta and Palosuo, 1981) to 1.2m over the continental shelves of the Beaufort and Chukchi Seas (Tucker et al., 1979). The range between 0.8 and 0.9 m has been commonly used in laser profiling studies over the Antarctic ice pack (e.g., Lytle and Ackley, 1991; Dierking, 1995).

2.5 RIDGE BUILDING EXPERIMENTS

Ridge building is not often witnessed in the field. Ice tank experiments allow the ridge building process to be observed and monitored, and can provide the connection between the profile of the top and bottom ice surfaces with the dynamic processes that shape them. This information can then be used for identifying ridges from drill profiles.

Tuhkuri et al. (1998 and 1999) reported on a series of ice tank experiments in which model ice sheets of varying thickness ratios were compressed, and the development of rafts and ridges was observed. Ridges formed from non-uniform ice sheets as ice blocks broke off and accumulated in piles. Rafts formed from uniform ice sheets of equal thickness as the sheets overrode one another and no piling up or down occurred. At the end of the experiments, three types of cross sections were observed:

Type A: Deformation features – Sail and keel;
Dynamic process – Ridging;
Surface profiles – Blocks piled above and below water surface.

Type B: Deformation features – Keel only;
Dynamic process – Ridging;

Surface profiles – Blocks piled underwater. Flat top surface.

Type C: Deformation features – Raft;
Dynamic process – Simple rafting;
Surface profiles – Flat top and bottom surfaces. Possibility of steps underwater where ice thickness doubles due to overriding.

2.6 RIDGE IDENTIFICATION SCHEME

2.6.1 Background

The focus of this paper is on developing a quantitative scheme to identify ridge sails and keels unambiguously from drill data. Visual identification alone, such as that used in previous ridge morphology studies will not be adequate, as it is not consistently reproducible. We will also use the identified sails and keels to characterize the morphology of first year Antarctic pressure ridges. The Rayleigh criterion recognizes a ridge by a trough-crest-trough structure, which presumes a triangular profile and can introduce a bias in the morphology of the identified ridges.

We develop a new ridge identification scheme based on the experimental results of Tuhkuri et al. (1998 and 1999). Extrapolating from their experiments, we can imagine an ideal initial situation where all ice sheets have thickened thermodynamically and have flat top and bottom surfaces prior to deformation. Deformation of such ice sheets, will result in three types of surface profiles:

Type 1: Surface profiles – Piles of blocks;
Dynamic process – Ridging.

Type 2: Surface profiles – Flat surface with the possibility of steps where ice thickness increases in multiples of parent ice thickness;
Dynamic process – Rafting.

Type 3: Surface profiles – Flat surface;
Dynamic process – None.

Consequently, any feature on the top and bottom surface profiles which is not level is potentially a sail or a keel.

The first step in identifying sails and keels is to identify non-level sections. However, the conditions of the ice pack are far from the ideal conditions described above. Prior to deformation, differential thermodynamic growth and melting and local isostatic imbalance can cause undulations on the ice surfaces. Ice floes formed from consolidation of pancakes contain a large quantity of small scale roughness elements. Deformation can occur as a combination of ridging and rafting. As a result, not all non-level features in the ice pack are associated with ridging and not all undeformed ice has flat surfaces. Our task is to relax the constraint on a flat surface and find a level ice definition which would satisfactorily identify sails and keels as non-level sections. Non-level sections which exceed the cutoffs will subsequently be identified as sails and keels. Identification of sails and keels following this scheme depends on the presence of level ice. Sails and keels within rubble fields with no level ice will not be identified. Hence, this identification scheme is not exhaustive, but with the careful choice of parameters and cutoffs, is precise.

2.6.2 Non-level ice identification

We develop a non-level ice identification scheme, the Explicit Gradient method, which combines the gradient test implied in the Implicit Gradient Point method and the rigour of testing every point within the gauge length in the Every Point method. According to this method, a POI at x m is non-level if

$$\frac{\left|h(x \pm d) - h(x)\right|}{d} \geq G \tag{2.4}$$

where d is the gauge length range within which the gradients between all points and the POI are assessed, and G is the gradient limit, which, when exceeded, renders the POI non-level.

We ran a series of tests, with different values of d (-2 to +2m, -5 to +5m, and –10 to +10m) and G (0.01 to 1.00 in steps of 0.01), in order to find optimal values for these parameters. Test results show that a small G (e.g., 0.05, Fig. 2.1a) has a similar effect as a large d (e.g., d = -10 to +10m, Fig. 2.2c) and is over stringent, as it identifies too little level ice, leaving a large amount of level ice to be potentially included in a ridge. A large G (e.g., 0.2, Fig. 2.1c) or a small d (e.g., d = -2 to +2m, Fig. 2.2a) is over relaxed, as it considers ridged ice as level.

We found that a combination of d = -5 to +5m and G = 0.09 provide the optimal values for identifying non-level ice from our data (Figs. 2.1b and 2.2b). We found it to be the best compromise between exhaustiveness and precision.

2.6.3 Cutoff values

For consistency, the non-level ice identification scheme and optimal parameter values described above are used to identify both sails and keels. However, due to the distinct difference in their sizes and in the reasons for identifying them, separate cutoff values are necessary for sail and keels.

Under the objective of using sail statistics to estimate the mass contained within keels, the focus on the sail is on its detectability, i.e., its height above the surrounding level surface. We define a sail as a non-level section on the top surface which has at least one point which is >0.3m above the surrounding level top surface. The sail cutoff value of 0.3m is chosen to match with the ASPeCt ice observations data, where sail heights as low as 0.3-0.4m may be included (Worby et al., 1995).

The focus on the keel is on its contribution of mass to the ice cover, and the purpose of the keel cutoff is to exclude rafted features and features which do not contain significantly greater volume than the surrounding level ice. Although conditions and occurrence of rafting may vary, modeling and experimental results have shown that uniform ice sheets of roughly equal thickness favour rafting (Hopkins et al., 1999).

Simple rafting, where the ice thickness is doubled, is likely to occur between uniform

ice sheets while multiple layering occurs between non-uniform ice sheets. Consequently, we base our keel cutoff on requiring the maximum ice thickness within the non-level section to be greater than a non-integer multiple of the surrounding level ice thickness. Due to the high sensitivity of the number of identified keels and the mean volume per identified keel to cutoff values, the latter should be as low as possible (Fig. 2.3). Therefore, we define a keel as a non-level section on the bottom surface which has at least one point which is >2.25 times as thick as the surrounding mean level ice thickness.

2.7 CONCLUSIONS

In this study, we developed a quantitative scheme for identifying ridge sails and keels from drill profiles obtained on first year Antarctic ice floes. A sail is defined as a non-level section on the top surface which has at least one point which is >0.3m above the surrounding level top surface. A keel is defined as a non-level section on the bottom surface which has at least one point which is >2.25 times as thick as the surrounding mean level ice thickness. A point of interest (POI) is non-level if the gradient between the POI and any point within 5m before or after the POI is greater than 0.09. Top surface measurement techniques, such as laser profiling or ship observations, can detect the snow sail from the snow surface and not the ice sail which is buried underneath the snow layer.

This study prepares the groundwork for extending the formulation to estimate keel volume from top surface measurements of the snow sail. It also forms the basis of a comprehensive study of the morphology of Antarctic first year pressure ridges, which includes comparisons with Arctic and Baltic ridges and studying seasonal and regional variations of ridge morphology.

2.8 ACKNOWLEDGEMENTS

This work was supported by NSF grant number OPP 9614844. We are grateful to Dr. Hajo Eicken for providing the data from the WWGS and EPOS cruises and Dr. Jukka Tuhkuri for invaluable comments. We also thank Captain Joe Borkowski, the officers and crew of the R.V. Nathaniel B. Palmer, the members of the science teams and Antarctic Support Associates personnel who contributed to the success of the NBP cruises.

2.9 FIGURES

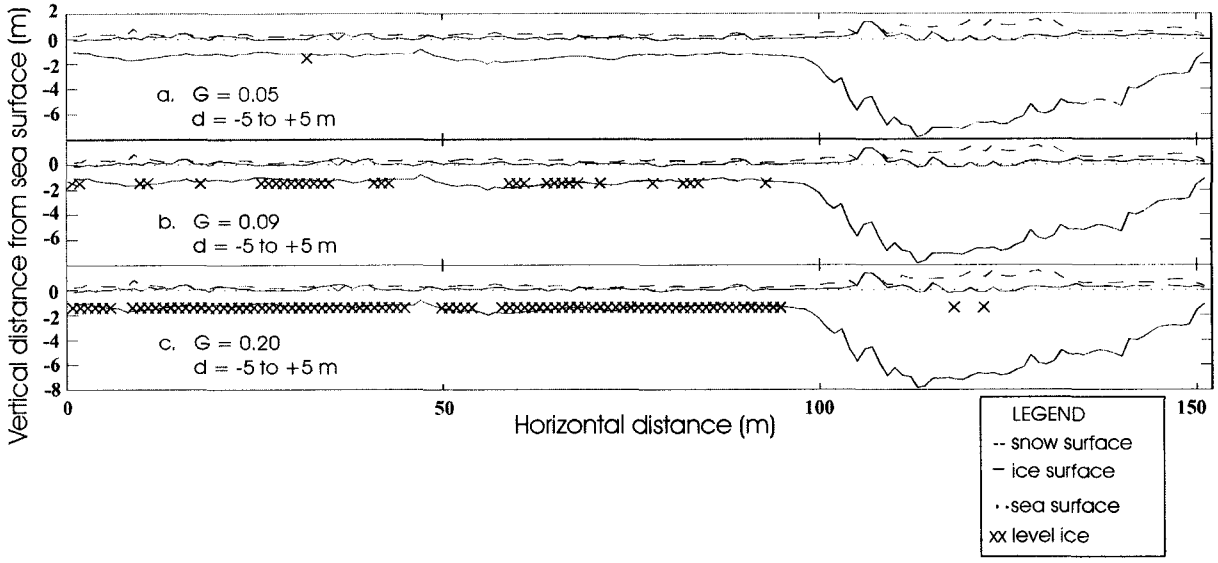

Figure 2.1 Examples of effects of increasing gradient limits, *G*, on keel identification. Gauge length ranges, *d*, are maintained at *d* = -5 to +5 m, while *G* increases from 0.05 (a), to, 0.09 (b), to, 0.20 (c).

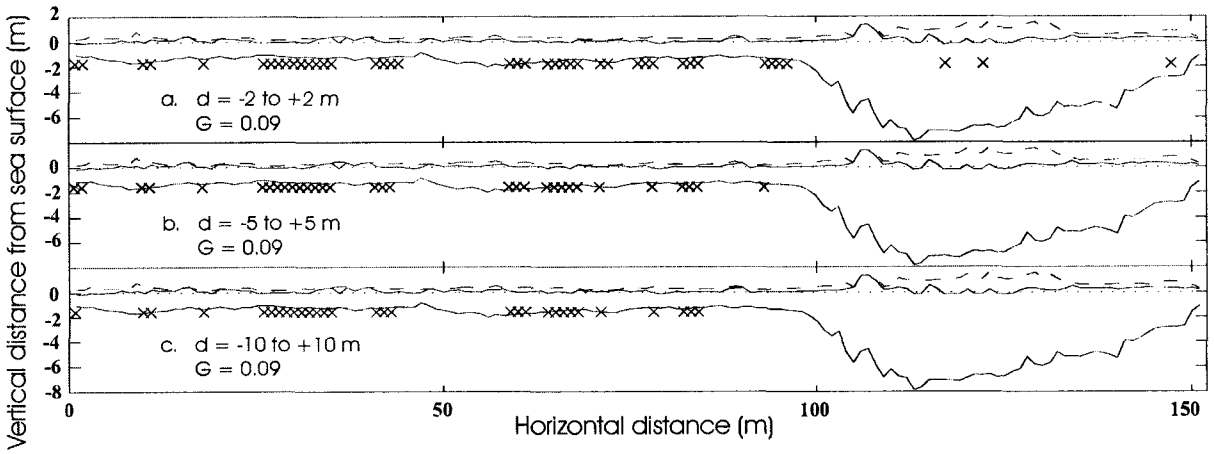

Figure 2.2 Examples of effects of increasing gauge length range, **d**, on keel identification. Gradient limits, *G*, are maintained at $G = 0.09$, while *d* increases from –2 to +2 m (a), to –5 to _5 m (b), to –10 to +10 m (c).

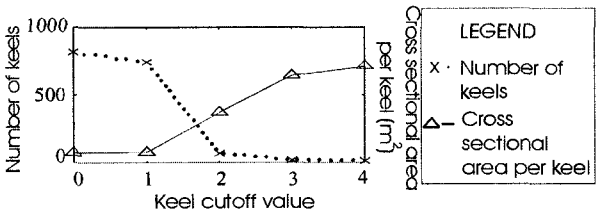

Figure 2.3 Effect of keel cutoff values on number and area of identified keels. Variation of number of identified keels and cross sectional area per identified keel

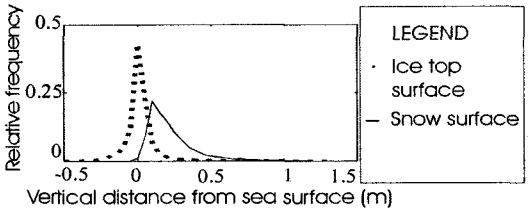

Figure 2.4 Frequency distribution of heights of ice top and snow surfaces above sea level. Relative frequency distribution of heights of ice top surface and snow surface above sea level for all 18 864 drill holes.

2.10 TABLES

Table 2.1 Summary of data used in this study

Cruise	Month	Year	Region	No. of profiles	Length of profiles
NBP99-1	Jan	1999	Ross / Amundsen Seas	19	2719m
NBP 95-3	May – June	1995	Ross Sea	49	3592m
NBP 98-3	May – June	1998	Ross Sea	24	3253m
WWGS 92	July	1992	Weddell Sea	2	124m
NBP 95-5a	Aug	1995	Ross Sea	28	2081m
NBP 95-5b	Aug – Sep	1995	Amundsen / Bellingshausen Seas	26	1928m
WWGS 89	Sep – Oct	1989	Weddell Sea	49	4562m
EPOS	Oct – Nov	1988	Northwest Weddell Sea	7	605m
TOTAL				**204**	**18 864m**

2.11 REFERENCES

Davis, N.R. and Wadhams, P. 1995. A statistical analysis of Arctic pressure ridge morphology. *J. Geophysical Research*, 100(C6), 10,915-10,925.

Dierking, W. 1995. Laser profiling of the ice surface topography during the Winter Weddell Gyre Study 1992. *J. Geophysical Research*, 100(C3), 4,807-4,820.

Granberg, H.B. and Leppäranta, M. 1999. Observations of sea ice ridging in the Weddell Sea. *J. Geophysical Research*, 104(C11), 25,735-25,745.

Haas, C., Liu, Q. and Martin, T. 1999. Retrieval of Antarctic sea-ice pressure ridge frequencies from ERS SAR imagery by means of *in situ* laser profiling and usage of a neural network. *Intl. J. Remote Sensing*, 20(15 & 17), 3111-3123.

Hibler, W.D. III, Weeks, W.F. and Mock, S.J. 1972. Statistical aspects of sea-ice ridge distributions. *J. Geophysical Research*, 77(3), 5954-5970.

Hopkins, M.A., Tuhkuri, J. and Lensu, M. 1999. Rafting and ridging of thin ice sheets. *J. Geophysical Research*, 104(C6), 13,605-13,613.

Høyland, K.V. and Løset, S. 1999. Measurements of temperature distribution, consolidation and morphology of a first-year sea ice ridge. *Cold Regions Science and Technology*, 29, 59-74.

Kankaanpää, P. 1997. Distribution, morphology and structure of sea ice pressure ridges in the Baltic Sea. *Fennia*, 175(2), 139-240.

Leppäranta, M. and Palosuo, E. 1981. Studies of sea ice ridging with a ship-borne laser profilometer. *Proc.6th POAC Conf.* Quebec, Canada. Vol. II, 1031-1038.

Lowry, R.T. and Wadhams, P. 1979. On the statistical distribution of pressure ridges in sea ice. *J. Geophysical Research*, 84(C5), 2,487-2,494.

Lytle, V.I. and Ackley, S.F. 1991 Sea ice ridging in the Eastern Weddell Sea. *J. Geophysical Research*, 96(C10), 18,411-18,416.

Melling, H., Topham, D.R. and Riedel, D. 1993. Topography of the upper and lower surfaces of 10 hectares of deformed sea ice. *Cold Regions Science and Technology*, 21, 349-369.

Timco, G.W. and Burden, R.P. 1997. An analysis of the shapes of sea ice ridges. *Cold*

Regions Science and Technology, 25, 65-77.

Tucker, W.B. III, Weeks, W.F. and Frank, M. 1979. Sea ice ridging over the Alaskan continental shelf. *J. Geophysical Research*, 84(C8), 4,885-4,897.

Tuhkuri, J., Lensu, M. and Hopkins, M.A. 1998. Laboratory and field studies on ridging of an ice sheet. *Proc. 14th IAHR Ice Symp.* Balkema, Rotterdam. Vol I, 397-404.

Tuhkuri, J., Lensu, M. and Saarinen, S. 1999. *Proc. 15th POAC Conf.* Helsinki, Finland. Vol III, 1,118-1,129.

Wadhams, P. and Horne, R.J. 1980. An analysis of ice profiles obtained by submarine sonar in the Beaufort Sea. *J. Glaciology*, 25(93), 401-424.

Wadhams, P., Tucker, W.B. III, Krabill, W.B., Swift, R.N., Comiso, J.C. and Davis, N.R. 1992. Relationship between sea ice freeboard and draft in the Arctic basin, and implications for ice thickness monitoring. *J. Geophysical Research*, 97(C12), 20,325-20,334.

Weeks, W.F., Kovacs, A. and Hibler, W.D. III. 1971. Pressure ridge characteristics in the Arctic coastal environment. *Proc. 1st POAC Conf.* Trondheim, Norway. Vol. I, 152-183.

Williams, E., Swithinbank, C. and de Q. Robin, G. 1975. A submarine sonar study of Arctic pack ice. *J. Glaciology*, 15(73), 349-362.

Worby, A.P. and Ackley, S.F. 2000. EOS, Transactions, American Geophysical Union, 81(17),181-185.

Worby, A.P. and Allison, I. 1999. A technique for making ship-based observations of Antarctic sea ice thickness and characteristics. Part I Observational technique and results. *Antarctic CRC Research Report No. 25.*

Worby, A.P., Jeffries, M.O., Weeks, W.F., Morris, K. and Jaña, R. 1996. The thickness distribution of sea ice and snow cover during late winter in the Bellingshausen and Amundsen Seas, Antarctica. *J. Geophysical Research*, 101(C12), 28,441-28,455.

Chapter 3

Morphology of deformed first year sea ice features in the Southern Ocean*

3.1 Abstract

A total of 42 deformed sea ice features were identified in almost 19 km of drill profile data from the Ross, Amundsen, Bellingshausen and Weddell seas. The features were classified according to the shapes of their keels underwater and the presence of a sail on the surface. Coupled ridges have triangular keels and sails and, with mean maximum keel depth of 3.61 m, they are the most massive of the deformed ice features. Widowed ridges have a triangular keel similar to those of coupled ridges but do not have a prominent ice sail. With a mean ridge width of 15 m, they are the narrowest of the deformed ice features. Rubble piles are the widest, but they contribute least to the total ice mass. Ignoring the ice mass of deformed ice features and approximating their thickness by surrounding level ice underestimates the total ice mass by 44% to 55%. First year ridges in the Antarctic are flatter and less massive than those in the Arctic. We propose that the differences in morphology are due to differences in sampling strategies, parent ice characteristics and the magnitude and duration of driving forces. For the purpose of estimating ice thickness from surface observations, we believe hydrostatic equilibrium is a fair assumption on large scales, but statistical relationships between variables that can be observed from the surface and variables that are hidden from the surface are not sufficiently strong and consistent for the estimation of ice thickness. In all cases, the fact that not all keels are associated with a sail and not all sails are associated with a keel should be addressed when estimating ice thickness from surface observations.

---

* Tin, T. and M.O. Jeffries. 2003. Cold Regions Science and Technology, 36(1-3), 141-163.

3.2 Introduction

A thorough knowledge of the sea ice thickness distribution and the total sea ice mass is essential for understanding the response of the ice cover to climate variability and change, and for the validation of dynamic-thermodynamic sea ice and climate models. The estimation of the total ice mass requires data on the frequency and morphology of deformed ice features such as pressure ridges. The importance of ridges in the Arctic is exemplified by studies that show that while they occupy 50% of the surface area they contribute 68% to 73% of the total ice mass in the winter Beaufort Sea (Melling and Riedel, 1995).

Arctic and sub-Arctic ridge frequency and morphology, including height, depth, width and slope angle of the sail (the part of the ridge above sea level) and the keel (the part of the ridge underwater), have been well documented by airborne laser, submarine sonar and moored upward looking sonar (e.g., Leppäranta and Palosuo, 1981; Tucker et al., 1979; Wadhams and Davy, 1986; Melling and Riedel, 1995), and drilling (e.g., Kovacs, 1972; Burden and Timco, 1995). Antarctic ridge frequency has been investigated using airborne laser (Weeks et al., 1989; Dierking, 1995; Granberg and Leppäranta, 1999), ship-based optical rangefinder (Lytle and Ackley, 1991) and aerial photography and synthetic aperture radar (Lytle et al., 1998). Each of these studies has shown that Antarctic ridge sails are not as high as those in the Arctic, but we know little else about Antarctic ridge morphology.

Moored upward-looking sonars have been deployed in Antarctica to obtain information on the sea ice thickness distribution (Strass and Fahrbach, 1998), but much of the current knowledge is based on direct measurement by drilling on ice floes (e.g., Wadhams et al., 1987; Lange and Eicken, 1991; Adolphs, 1999) and ship-based observations (e.g., Wadhams et al., 1987; Allison et al., 1993). Ship-based observations are increasingly based on standardized protocols developed by the ASPeCt (Antarctic Sea Ice Processes and Climate) program of SCAR GLOCHANT (Scientific Committee on Antarctic Research, Global Change and Antarctic program) (Worby and Ackley, 2000).

According to the ASPeCt protocols, the thickness of unridged sea ice and its snow cover are estimated as floes turn on their sides next to the ship. However, ridges are made

of piles of ice blocks with varying amounts of cohesion. When consolidated, ridges tend not to completely turn on their sides and when they are unconsolidated they often disintegrate upon impact by the ship, making it difficult to estimate ridged ice thickness. Thus, in addition to estimating the unridged ice thickness, the ASPeCt protocols require the estimation of ridge height and areal extent, and the three variables are used to calculate ridged ice thickness based on a geometrical model of a typical Antarctic pressure ridge (Allison and Worby, 1994). Using this approach, it has been estimated that the 25% of the Bellingshausen and Amundsen Seas pack ice that is ridged contains 50-75% of the total ice mass, for example (Worby et al., 1996).

The large amount of Antarctic sea ice thickness data that have been obtained by drilling since the 1980s makes it possible now to undertake a first quantitative investigation of the morphological variability of pressure ridges and other deformed ice features. A better knowledge of the morphology of deformed ice features is essential for improving the estimation of their thickness and contribution to the total ice mass. One issue of particular interest is the relationship between surface features and ice thickness. Since the Southern Ocean sea ice cover is blanketed under a deep and extensive snow cover for most of the year, is the feature on the snow surface, as recorded by ship-based, airborne or satellite observations, such as from CRYOSAT or ICESAT in the future, related to ice deformation? Is there any relationship between the feature on the snow surface and ice thickness or dimensions of deformed ice features? Another issue of interest is the scale at which the assumption of hydrostatic equilibrium is valid. It has been assumed in numerous studies that each ridge sail is hydrostatically balanced by a keel underwater. Subsequently the total ice volume is estimated from the volume of the sail (e.g., Zubov, 1963, Kirillov, 1957, Hibler et al., 1974, Leppäranta, 1981, Allison and Worby, 1994). Although hydrostatic equilibrium must be maintained on all floating ice floes, field studies have shown that local imbalance is common (e.g., Weeks et al., 1978). At what scale does the imbalance become insignificant, and hence, at what scale can hydrostatic equilibrium be used to estimate ice thickness? A final issue of interest relates to studies in which ridged ice thickness is estimated from ridge frequencies and an ideal

ridge cross-section (e.g., Hibler et al., 1974, Steiner et al., 1999). Little is known about the cross-section of the typical Antarctic deformed ice feature and, therefore, ice volume in regions of the Southern Ocean has often been estimated from a combination of Antarctic ridge frequencies and Arctic ridge cross-section (Dierking, 1995, Lytle et al., 1998). This leads to the question of: what is the shape of the typical Antarctic deformed ice feature and how does it compare with the geometry of Arctic deformed ice features?

We believe that an understanding of the morphology of deformed ice features, their states of hydrostatic equilibrium and the relationships between surface features and ice thickness are essential for accurate estimates of ice volume on the Southern Ocean. The need for such information is the motivation for this study, which uses drilling data obtained since 1989 during eight cruises in the Ross, Amundsen, Bellingshausen and Weddell seas. In this paper we (1) examine the morphology of deformed ice features, including their shape, size and state of hydrostatic equilibrium, (2) derive a shape for the typical Antarctic deformed ice feature, (3) explore the consequences of morphology on the estimation of deformed ice thickness from ship-based observations of surface features, and (4) place our findings in a wider context by comparing them with the morphology and formation mechanisms of deformed ice features in the Arctic sea ice cover.

In this study, we use the term ridging to refer to the deformation mechanism whereby adjacent floes are pushed toward each other, break by flexure or buckling and finally form features composed of piles of ice blocks (Parmerter and Coon, 1972). We use the term pressure ridge to refer to a type of feature that is formed by the mechanism of ridging, and is commonly associated with a structure of a triangular sail and keel (e.g., Parmerter and Coon, 1972; Wittmann and Schule, 1967; Kankaanpää, 1997). Sea ice can deform via other mechanisms too, such as rafting and shearing (Parmerter, 1975; Tucker et al., 1985) but for the purpose of improving the estimates of ice thickness from ship observations we are only interested in features formed from the process of ridging. In this study, these features are referred to as deformed ice features or deformation features, and include, but are not limited to, pressure ridges.

3.3 Data and data considerations

Table 2.1 lists the sources of the drilling data used in this study. Drilling was conducted along line transects, each between 50 and 150 m in length. Holes were drilled at 1 m intervals and snow depth (z_s), ice thickness (z_i), and freeboard (z_f) were measured at each hole.

The primary goal of the drilling programs was to establish the ice thickness distribution. Therefore transects were set out to sample features representative of the surrounding ice cover, which may include surface features such as ridge sails or sastrugi. This sampling design differs from that of earlier ridge morphology studies. Earlier studies were frequently motivated by the needs of winter navigation (e.g., Kovacs, 1972; Kankaanpää, 1989) and design of vessels and offshore structures (e.g., Tucker et al., 1985; Melling et al., 1993; Surkov, 2001), and hence concentrated on large ridges and were located in the vicinity of prominent sails. An advantage of our data is that the sampling is more random and hence the sample is more representative of the true population. However, there are shortcomings associated with using data which were not specifically targeted towards the examination of deformed ice features. Since ice and snow thicknesses were the primary variables of interest in the drilling program, no data were collected on the internal structure of the deformed ice features, including block size and the size of voids between blocks. The examined transect is only a snapshot in time and space and there is no information on the thickness of the parent ice sheet or the forces involved in the formation of the deformed ice feature. Common to other field studies, collection of our data involves the usual difficulties and complications of studying a snapshot of a dynamic system. Drill data only provides information along a single transect and only one transect was sampled along each deformed ice feature. However, deformed ice features are three-dimensional features and may extend hundreds of kilometers longitudinally while its cross-section may differ along its longitudinal axis. They are also jumbles of ice blocks which can make accurate positioning and drilling difficult. Young features tend to be unconsolidated and ice blocks may move during sampling. The distribution and thickness of snow are highly variable and depend on a

wide range of factors, such as wind direction, floe rotation and precipitation. These issues increase the uncertainty in the assessment of hydrostatic equilibrium and interpretation of the formation history of these features.

While the readers should be aware of the shortcomings of the data, they should also be aware that currently there are no available data on the three-dimensionality, internal structure or formation history of Antarctic deformed ice features. Despite the shortcomings, our data are the most complete set of drill transects of 1-m spacing collected from the Southern Ocean to date, and can provide some first insights into the morphology of Antarctic deformed ice features.

3.4 Identification of deformed ice features from drill profiles

The first task is to systematically identify deformed ice features in drill profiles. In the past, researchers have identified pressure ridges from surface profiles either visually for examining their morphology (Worby and Allison, 1999), or by the Rayleigh criterion for examining their spatial statistics (e.g. Adolphs, 1998; Dierking, 1995). According to the Rayleigh criterion, an individual ridge sail or keel is a feature containing a crest (a local maximum) enclosed by troughs (local minima) on both sides, which descend at least halfway towards the local level ice horizon (Lowry and Wadhams, 1979). In addition, the sail (or keel) must be higher (or deeper) than a cutoff value. When applied to Antarctic drill profiles, the Rayleigh criterion identifies narrow peaks within an extensive feature as individual ridges but is not able to identify the extensive feature which is surrounded by level ice as one ridge (Fig. 3.1). One of the goals of our study is to derive the shape of the typical Antarctic deformed ice feature. We want to avoid prescribing the shape of the feature that we want to derive. However, the Rayleigh criterion picks out ridges from a minimum-maximum-minimum progression of the surface profile, thereby prescribing an intrinsic minimum-maximum-minimum or peak-like structure for all identified ridges. Fig. 3.1 supports the idea suggested by Melling and Riedel (1995) that the Rayleigh criterion is identifying the component blocks of keels as keels when the vertical scale of

the block substructure of the keel becomes comparable to the vertical scale of the keel itself. In their analysis of 348 km of sea ice draft obtained from moored subsea sonars, Melling and Riedel (1995) concluded that the Rayleigh criterion is not an effective discriminator of keels for drafts below 5 m. Our data falls within this regime since the mean draft for all 204 profiles used in our study is only 0.82 m. Therefore we need to develop a new identification scheme which would better suit our purpose.

A quantitative scheme for identifying deformed ice features for the purpose of morphology studies has been developed by Tin and Jeffries (2001). According to this identification scheme, a sail is a non-level section on the top surface that has at least one point which is ≥0.3 m above the higher of the adjacent level top surfaces. A keel is a non-level section on the ice bottom surface that has at least one point which is ≥2.25 times more thick than the thicker of the adjacent level ice sections. In addition, a sail or a keel must be flanked on both sides by level ice, or if it is at the end of a profile, the thickness of the point at the end of the profile must be within 10% of that of the level ice on the other side. A point of interest (POI) is non-level if the gradient between the POI and any point within 5 m before or after the POI is greater than 0.09. A sail cutoff height of 0.3 m is chosen to match with the Antarctic ship observation data, where a surface feature as low as 0.3-0.4 m may be counted as a sail (Worby et al., 1996). A cutoff thickness of 2.25 times that of surrounding level ice is chosen in order to exclude small keels which contribute little in volume, and to exclude rafted features which are likely to be an integer number of times the thickness of level ice. No other assumptions of the shape of sails and keels are made.

Fig. 3.2 shows the result of applying this identification scheme to a floe profile. It shows that the new identification scheme works better than the Rayleigh criterion (Fig. 3.1) in identifying deformed ice features for the purpose of deriving the shape of the typical Antarctic deformed ice feature.

3.5 Data analysis

3.5.1 Classification of keel shapes

Pressure ridges have often been idealized as a two-component feature, comprising a small triangular sail and a deep and wide triangular keel (e.g., Wittmann and Schule, 1967; Kankaanpää, 1997; Timco and Burden, 1997). The shapes of deformed ice features identified in the Antarctic drill profiles vary widely, with some components being triangular and others being irregular and made up of multiple peaks. In order to facilitate comparison with previous studies of ridge morphology, we develop a scheme to classify the keels of our Antarctic deformed ice features as triangular or non-triangular.

The exact definition of whether a keel is triangular is derived from its curve of cumulative normalized cross-sectional area versus normalized horizontal distance along the keel. Starting from the left end of the keel, the cumulative cross-sectional area of the keel, normalized to a total of unit keel area, is calculated. This is plotted against the horizontal distance from the left end of the keel, normalized to a total of unit keel width. In the case of a perfect triangle, the cumulative percentage area curve has a strong point of inflexion, marked by a significant perpendicular distance between the two limbs of the curve before and after the point of inflexion (Fig. 3.3a). We use the Inclusive Graphic Standard Deviation as a measure of the distance between the two limbs of the curve and hence the "strength" of the inflexion. The Inclusive Graphic Standard Deviation, σ_I, is used in sedimentology as a measure of the uniformity of a non-normal distribution (Folk and Ward, 1957), and is defined as

$$\sigma_I = \frac{W_{84\%} - W_{16\%}}{4} + \frac{W_{95\%} - W_{5\%}}{6.6} \qquad (3.1)$$

where, in the case of a deformed sea ice feature, $W_{X\%}$ represents the percentage of keel width at the X^{th} percentile of the cumulative percentage area. A perfect triangle has σ_I of 0.20 (Fig. 3.3a). In the case of a perfect rectangle, there are no points of inflexion on the cumulative percentage area curve and σ_I is 0.30 (Fig. 3.3b).

For the keel of each deformed ice feature identified in the Antarctic drill profiles, a smoothed cumulative percentage area curve is first computed from the raw cumulative percentage area curve, which is compiled from the drill data. Using a 3-point moving average, the smoothed cumulative percentage area at a POI is equal to the mean of the raw cumulative percentage area of the POI and the points before and after the POI. We chose σ_I of 0.23 on the smoothed cumulative percentage area curve to differentiate between triangular and non-triangular keels since results using this value matched most closely those from visual classification. A keel with $\sigma_I < 0.23$ is considered as triangular (Figs. 3.4a and b). A keel with $\sigma_I \geq 0.23$ is considered as non-triangular (Fig. 3.4c).

3.5.2 Calculation of slope angles

The widths and slope angles of ridge sails and keels are calculated based on a triangular approximation as outlined in Fig. 3.5. Essentially, each ridge sail and keel is approximated by a triangle with the apex at the point of maximum vertical distance from the level surface and which has the same cross-sectional area as the sail or keel contained by level ice on both sides. This is similar to the definition used by Kankaanpää (1997) on Baltic Sea pressure ridges and is used here as it appears to be a fair description of the Antarctic data (Figs. 3.4a and b) and facilitates comparison with existing Arctic data.

3.5.3 Assessment of hydrostatic equilibrium

An accurate assessment of the net hydrostatic equilibrium depends on accurate values of snow and ice densities and porosities and an understanding of the loading of the ice floe in three dimensions. Since not all of these data are available from our two-dimensional transects, we make a best first order assessment of the hydrostatic equilibrium of our deformed ice features by using the most appropriate assumptions of density and porosity values, incorporating a reasonable error margin, and assuming

negligible longitudinal effects. Although it is impossible to make an accurate assessment, similar results from other studies have provided useful insight into the structure of deformed ice features (e.g., Bowen and Topham, 1996; Leppäranta and Hakala, 1992; Kovacs, 1972).

Hydrostatic equilibrium occurs when weight (acting downward) and buoyancy (acting upward) balance. Weight, W, is the sum of the weights of snow, ice, and any slush. Buoyancy, B, is equivalent to the weight of seawater displaced by the volume of submerged ice and slush. These forces are given by

$$W = \{\rho_s z_s + \rho_i(1-\alpha)z_i\}g \qquad \text{for } z_f \geq 0 \qquad (3.2a)$$

$$W = \{\rho_s(z_s + z_f) - \rho_{sl}z_f + \rho_i(1-\alpha)z_i\}g \qquad \text{for } z_f < 0 \qquad (3.2b)$$

$$B = \{\rho_w(1-\alpha)(z_i - z_f)\}g \qquad \text{for all } z_f \qquad (3.2c)$$

where ρ_s, ρ_i, ρ_{sl} and ρ_w are the densities of snow, ice , slush and water respectively, z_s is snow thickness, z_i is ice thickness, z_f is freeboard, α is the total porosity of the ice and g is gravitational acceleration.

Theoretically, equilibrium only exists when the difference between weight and buoyancy is zero. In practice, there is considerable variability and uncertainty in the values of snow and ice densities and porosities, leading to the calculated value of net force being a rough estimate of the true value. Hence, it is more appropriate to denote equilibrium with a range of values instead of a single value. Assuming that level ice has not been ridged and is in hydrostatic equilibrium, we establish an equilibrium range between the mean calculated net force across all level ice ± two standard deviations of the mean calculated net force. This range encompasses the calculated net force measured across 95% of all level ice sections. In order that the equilibrium range maintains a scale comparable to the deformed ice features, only level ice of at least 5 m in length is considered, as the smallest identified deformed ice feature is 5 m wide.

For the purpose of examining the hydrostatic equilibrium of the identified deformed ice features, density values are taken from measurements made on the same ice floes as the drill transects, when possible. When such data are not available, density values are

borrowed from previous studies. The values of ρ_s used for each cruise are listed in Table 3.2. In most cases, the value of ρ_s represents a bulk mean value measured in snow pits on each cruise. In the case of two cruises, the value of ρ_s has been extrapolated from bulk mean snow and ice thickness and freeboard of each cruise, on the assumption that hydrostatic equilibrium holds, on average, on a large scale. The values of ρ_w and ρ_i are not measured as often, but they also do not vary as much as ρ_s; therefore, values of 1 030 kg m^{-3} and 920 kg m^{-3}, which are commonly assumed for the Southern Ocean (e.g., Eicken et al., 1994) are used. Accurate measurements of ρ_{sl} are difficult to obtain and Adolphs (1998) has defined a maximum possible slush density, $\rho_{sl/max}$, assuming that all the vesicles in the snow are filled with water:

$$\rho_{sl/\max} = \rho_w - \left(\frac{\rho_w - \rho_i}{\rho_i}\right)\rho_s \qquad (3.3)$$

In practice, air may be trapped inside the slush, hence a value of ρ_{sl} which assumes a 10% air content and, therefore, is 90% of $\rho_{sl/max}$, is used for the calculations.

Another key parameter in the assessment of hydrostatic equilibrium is the total porosity, α, of ridged and unridged ice. The total porosity is a combination of macro porosity, which arises from structural voids between ice blocks in ridged ice, and material porosity, which is made up of air and water pockets in the ice (Høyland, 2002). There are no published data on the total porosity of Antarctic sea ice. Therefore, for the subsequent calculations, we make the assumption that the total porosity for unridged ice is zero and the total porosity for ridged ice is 0.35. By including an error margin of 20%, the porosity of ridged ice used in the calculations ranges from 0.28 to 0.46 and encompasses the values that have been measured in Arctic and Baltic ridges (Kovacs, 1972; Kankaanpää, 1997; Høyland and Løset, 1999). In addition, error margins are also included in values of density and thickness in order to account for uncertainties in their measurement. An error margin of 20% is assumed for ρ_{sl}, ρ_s, z_s and z_f and a margin of 5% is assumed for ρ_w and ρ_i.

3.6 Morphology of Antarctic deformed ice features

3.6.1 New terminology

The existing terminology for deformed ice features was originally developed out of the necessity to describe features in the Arctic ice cover. In our examination of deformed features in the Antarctic ice cover we have found different conditions and features that necessitate the introduction of some new terminology.

In the literature, the boundary between a sail and a keel has always been represented by sea level. However, the Antarctic ice cover has a large snow load relative to ice thickness and the ice top surface is often submerged below the sea surface. A submerged sail with negative cross-sectional area has little physical meaning. Therefore, in this study, except when comparing with Arctic data, sails and keels are defined with respect to the surrounding level surface, as shown in Fig. 3.6. This avoids inconsistencies due to differences in snow accumulation.

We define a feature, called an "ice sail", as a feature on the ice top surface that satisfies the sail identification scheme (Fig. 3.6). The boundary between ice sail and the ice keel is at the ice top surface of adjacent level ice. Both the ice sail and the ice keel are predominantly composed of ice. The shape of the ice sail is a result of deformation and, to a lesser effect, subsequent thermal modification beneath the snow cover.

We define a feature, called a "snow sail", as a feature on the snow surface that satisfies the sail identification scheme (Fig. 3.6). The term snow sail refers to a feature which looks like a sail as viewed from a ship and does not imply that it is formed by the deformation processes that create ice sails and ice keels. Observers on ships may not be able to distinguish between snowdrift and deformed ice features; hence, some of these observed snow sails may be formed by wind redistribution, such as sastrugi or dunes, and not related to the ridging process which produces keels. The snow sail is an important feature since, unlike the ice sail which is obscured by the snow cover, it can be detected by top surface measurements by ship-based, airborne and satellite sensors. Therefore, its relationship with the hidden parts of the deformed ice feature are particularly important.

The boundary between snow sail and the mixed keel is at the snow surface of adjacent level ice. The snow sail is composed of snow and ice. The mixed keel is composed of ice, snow and slush, the proportions of which depend on the amount of surface flooding of the ice floe. We define a sail as "associated" with a keel, and hence as part of the same feature, when they overlap in horizontal extent.

Following on from the classification of triangular and non-triangular keels, we classify features with triangular keels as pressure ridges (Figs. 4a and b) and features with non-triangular keels as rubble piles (Fig. 3. 4c). Pressure ridges with an associated ice sail are classified as coupled ridges (Fig. 3.4a). Pressure ridges without an associated ice sail are classified as widowed ridges (Fig. 3.4b). As a result, coupled ridges have a keel that slope downwards from the ends to a single prominent peak near the center of the keel, and a prominent ice sail on the surface (Fig. 3.4a and 3.7a). Widowed ridges have a triangular keel similar to those of coupled ridges but do not have a prominent ice sail (Fig. 3.4b and 3.7b). Rubble piles have a keel that is made up of multiple peaks distributed throughout the width of the keel (Fig. 3.4c). These peaks can be deep or shallow, but the maximum depth of the peaks is usually a small fraction of the total keel width. Keels of rubble piles are more similar in shape to that of a rectangle than a triangle (Fig. 3.7c). The width of a rubble pile is defined as the closest separation between the flanking level ice sections.

3.6.2 General morphology

From 204 drill profiles, a total of 42 keels, 72 ice sails and 57 snow sails were identified. Not all keels are associated with sails and not all sails are associated with keels: 16 (22%) of the ice sails and 14 (25%) of the snow sails overlap with a keel. Out of the 42 keels, 40% are represented by an ice sail on the top surface and 33% are represented by a snow sail. Each keel and any associated snow or ice sail is considered as a deformed ice feature. In a total of 42 deformed ice features, there were 12 (29%) coupled ridges, 13 (31%) widowed ridges and 17 (40%) rubble piles.

The dimensions of the three types of deformed ice features, with idealized cross-sections, are presented in Fig. 3.7. Coupled ridges are the most massive of the three categories. They have a mean thickness or area per unit ridge width which is more than 50% of either widowed ridges or rubble piles. The ice sail is small compared to the ice keel in a coupled ridge: the width of the ice sail is only 30% that of the keel, and the mean height of the ice sail, or sail area per unit sail width, is less than 10% of the mean depth, or area per unit width of the keel. On average, the crest of the ice keel is located close to the center of the ridge, with the crest of the ice sail located within a distance of 1% of the keel width from the crest of the keel. If the contribution of ice mass from a coupled ridge is ignored and the ice mass is only approximated by surrounding level ice, the underestimation of total ice mass is approximately 55%, as estimated from

$$\frac{\sum^{W} z_i - LW}{\sum^{W} z_i} \tag{3.4}$$

where L is the surrounding level ice thickness, W is the width of the ridge and z_i is the measured ice thickness at each drill hole.

Widowed ridges are the narrowest of the three types of deformed ice features. Their triangular keels are shallower and flatter than those of coupled ridges. Rubble piles are the widest, but they contribute least to the total ice mass. However, approximating the thickness of a rubble pile by surrounding level ice still underestimates the total ice mass by nearly 40%.

3.6.3 Aspects of morphology pertinent to the estimation of ice thickness

Ridged ice thickness can be estimated from ship-based observations by using statistical relationships between the snow sail and ice thickness or by assuming hydrostatic equilibrium. In this section, we examine how these two methods can be used to estimate the total mass of our Antarctic deformed ice features.

3.6.3.1 Snow sails

As first defined in Section 5.1, the term snow sail refers to a feature which looks like a sail as viewed from a ship and does not imply that it is formed by the deformation processes that create ice sails and ice keels. Observers on ships may not be able to distinguish between snowdrift and deformed ice features, and hence, some of the observed sails may be formed from wind redistribution, such as sastrugi, and not related to the ridging process which produces keels. The shape of the snow sail is a result of the underlying ice top surface, snow accumulation and wind redistribution; as a result, snow sails can exist independently of an ice sail or the keel. Of the 57 identified snow sails, 14 (25%) overlap with a keel, 33 (58%) overlap with an ice sail, and 10 (18 %) overlap with an ice sail and a keel simultaneously. Snow sails are wider and flatter than ice sails (Fig. 3.8). The mean maximum height of the snow sail above the level snow surface is about 0.2 m less than the mean maximum height of the ice sail above the level top ice surface, while the snow sail is more than twice as wide as the ice sail. As a result, the slope angles of the snow sail are about half those of ice sails.

Since snow sails are the only features that can be detected by top surface measurements, such as by ship-based, airborne and satellite sensors, their relationships with hidden parts of the deformed ice feature are particularly important. In order to examine the possibility of using statistical relationships between snow sail and ice thickness to estimate the thickness of deformed ice features, Fig. 3.9 plots a set of surface variables: snow sail width, snow sail maximum height, snow sail area and level ice thickness, against a set of hidden variables: ice keel width, ice keel maximum height, ice keel area, underestimation of level approximation (as defined by Eqn. 3.4) and mean ridge thickness (or ridge area per ridge width). All plots exhibit considerable scatter and correlation between variables is strongly influenced by outliers. In order to look for strong correlations which are independent of outliers, we calculated the correlation coefficients before and after the removal of the largest outlier, defined as the data point which has the highest value in the hidden variable. In the cases where snow sail dimensions were the

surface variables, these calculations were repeated after the removal of each of the five subsequent outliers. Where level ice thickness was the surface variable the calculations were repeated for ten outliers since the sample sizes were larger in these cases. It was not possible to establish a strong and consistent correlation between any surface and hidden variables, as correlation coefficients fluctuated depending on the presence or absence of the largest outlier and none of the correlation coefficients remained consistently above 0.7.

3.6.3.2 Hydrostatic equilibrium

In previous studies, it has been common practice to assume each ridge sail is hydrostatically balanced by a keel and to estimate the total ice volume from the volume of the sail (e.g., Zubov, 1963; Allison and Worby, 1994). However, although hydrostatic equilibrium must be maintained on all floating ice floes, local imbalance is common. In this section, we attempt to find the scale at which hydrostatic equilibrium can be used to estimate ice thickness by examining the hydrostatic equilibrium of deformed ice features at the different scales of the sail, the keel and the drill profile.

From a total of 10 km of level ice, we found a mean net downward force of -17 N m^{-2} and a standard deviation (σ) of 202 N m^{-2}. The mean ± two standard deviations gives an equilibrium range of -422 to 388 N m^{-2}, which we assume as the range within which hydrostatic equilibrium is maintained for our drill data. We picked out the part of the deformed ice features as denoted by the width of the ice sail (Fig. 3.10a), the snow sail (Fig. 3.10b), and the keel (Fig. 3.10c) and assessed the mean net force over these sections of deformed ice features against the equilibrium range. This was also performed for the mean net force over the entire length of the transect (Fig. 3.10d). Fig. 3.10 shows that when only the sections denoted by either the ice sail or the snow sail are assessed, approximately 25% of the deformed ice features are in hydrostatic equilibrium. When the mean net force is calculated over the width of the keel and for the length of the transect, this increases to 71%. The extreme cases of including error margins of 20% for ρ_{sl}, ρ_s, z_s,

z_f and α, and 5% for ρ_w and ρ_I indicate a similar trend, which shows that hydrostatic equilibrium is more likely on the scale of the keel width (average of 30 m) or transect length (50 – 150 m) than on the scale of sail width (average of 8 m).

Of the deformed ice features which are out of hydrostatic equilibrium, three are coupled ridges, three are widowed ridges and six are rubble piles (Fig. 3.10c). They are all placed out of equilibrium by excess downward force, which is a result of excess snow and sail loading. None of the features are placed out of equilibrium due to excess buoyancy. Buoyancy is easily balanced even without a prominent sail, as indicated by the large proportion (77%) of widowed ridges which are in equilibrium. With a mean maximum keel depth of 1.82 m (Fig. 3.7), keels of widowed ridges only need to be balanced by an ice freeboard of 0.18 m. With a mean keel width of 15 m (Fig. 3.7), this can easily be achieved by arching of an intact ice sheet at an angle of <2°, or by small scale surface roughness which may not be identified as a sail.

3.6.4 Implications of ridge morphology on the estimation of ice thickness

Although hydrostatic equilibrium clearly holds over large areas, we found that 71% of deformed ice features were in hydrostatic equilibrium at the scale of their keel widths (average 30 m), but only 25% were in hydrostatic equilibrium on the scale of their sail widths (average 8 m). Melling et al. (1993) have examined the hydrostatic equilibrium of a contiguous region instead of a linear transect and have shown that hydrostatic equilibrium is maintained at a scale of 200 m. We believe that hydrostatic equilibrium is a fair assumption over large areas but we caution against applying hydrostatic equilibrium over the surface area occupied by individual ridge sails to estimate ice thickness. Since the keel is typically 3.5 times wider than the sail (Fig. 3.7), hydrostatic equilibrium is maintained between the keel, its sail and the surrounding level ice above the keel. If the amount of ice underwater is estimated to be the volume that is needed to hydrostatically balance the sail alone, the amount of ice underwater tends to be underestimated, because

the hydrostatic effect of the surrounding level ice has been ignored.

Apart from using the assumption of hydrostatic equilibrium, which is based on the physics of the ice floe, another method that can be used to estimate thickness of deformed ice features is to use the statistical relationships between surface and hidden variables. However, as shown in Fig. 3.9, these relationships derived from existing data, are weak, and more data are needed to establish strong and consistent relationships between surface and hidden variables if they are to be used to estimate ice thickness. Last, but not least, regardless of whether a statistical or physical argument is used to estimate ice thickness from surface observations, the effect that not all keels are associated with a sail and not all sails are associated with a keel should be addressed.

3.7 Arctic and Antarctic comparisons

Previous studies have reported that Arctic ridges are usually composed of large numbers of small blocks; sails are typically up to 2 m high; keels are over 10 m deep; and the ridges may extend linearly for over hundreds of kilometers (Wadhams, 1998). Studies in the Antarctic indicate that ridges in the Southern Ocean appear to be more point type roughness features like hillocks (Fig. 3.11a; Lytle and Ackley, 1991), or are in the form of short linear features which delineate the edges of ice floes (Fig. 3.11b; Jeffries and Weeks, 1992). They also appear to be composed of a small number of fairly thick blocks (Fig. 3.11a). For a more quantitative comparison, we make use of the reports of Burden and Timco (1995) and Timco and Burden (1997) which described the morphology of 112 first year pressure ridges in the Arctic. Their data were obtained by drilling, surveying and sonar profiling during 22 different studies. They divided the ridges into two categories according to their locations: "temperate" ridges were found in the Labrador Sea, Baltic Sea, Northumberland Strait and the south Bering Sea; and "Beaufort" ridges were from the Beaufort Sea in the Arctic Ocean. There were a total of 66 temperate and 46 Beaufort first year ridges. In addition, Davis and Wadhams (1995) also described the morphology of 729 ridge keels, as measured by side scan and upward looking sonars in the Arctic

Basin, between the North Pole and the Greenland Sea. We will refer to these as "Greenland" keels and use them in the following section as an illustration of the morphology of keels from other parts of the Arctic Basin. Due to the lack of information on the surface profile above sea level and the knowledge of the age of the keels in the study of Davis and Wadhams, our comparison will be mainly based on the results of Timco and Burden (1995) and Burden and Timco (1997). For the purpose of maintaining consistency between the different data sets, sea level is used to mark the boundary between the sail and the keel for this part of the study. In addition, all references to the sail refer to the ice sail.

The dimensions of Antarctic and Arctic first year pressure ridges are presented in Table 2.3. The dimensions of Antarctic pressure ridges are smaller than Beaufort ridges, but similar to those of Arctic temperate ridges. However, the sails and keels of both Beaufort and Arctic temperate ridges have steeper angles than Antarctic ridges. The mean maximum keel depth of Antarctic coupled ridges is nearly 70% of that of temperate Arctic ridges but less than 30% of that of Beaufort ridges. The mean maximum sail height of Antarctic pressure ridges is approximately 50% of that of temperate Arctic ridges and only 20% of that of Beaufort ridges. Antarctic and temperate Arctic sails and keels are similar in width but Beaufort sails are nearly 3 times as wide as Antarctic sails. Beaufort and Greenland keels are similar in width and are 200% to 500% as wide as Antarctic keels. Antarctic sails and keels are flatter than their Arctic counterparts, with slope angles nearly half those of all Arctic ridges: temperate, Beaufort and Greenland. The area in Antarctic sails is less than 15% of that in Arctic sails, while the area in Antarctic keels is close to half that in Arctic keels. As a result, the ratio between keel area and sail area is nearly 4 times higher in Antarctic ridges than in Arctic ridges.

3.8 Hypotheses on the differences in ridge morphology

Our results indicate that Antarctic ridges have larger keel area to sail area ratios than Arctic ridges; sails and keels of Antarctic ridges are also flatter than the Arctic ones; and

the dimensions of Antarctic ridges are significantly less than those of Arctic ridges from the Beaufort Sea, but are close to those from the Arctic temperate regions. Antarctic deformed ice features vary too: widowed ridges, unlike coupled ridges, lack prominent sails, and keels of rubble piles are wider and flatter than keels of coupled or widowed ridges. These findings beg the question of what causes such differences.

It is difficult to answer this question because data on the conditions during ridging are sparse. Here, we will first examine the various factors which may contribute to the observed differences in ridge morphology and then formulate a number of hypotheses which highlight the types of data which should be examined in the future to explain the observed differences in ridge morphology.

We propose that differences in the morphology of the deformed ice features arise from three main factors:

- sampling: choice of ridge, location of transect on ridge
- parent ice characteristics: ice strength, as determined by thickness, consolidation, homogeneity and crystal structure; and friction of surfaces
- driving forces: duration and magnitude

3.8.1 Sampling

Interest in Arctic deformed ice features has frequently been motivated by the needs of winter navigation (e.g., Kovacs, 1972; Kankaanpää, 1989), and design of vessels and offshore structures (e.g., Tucker et al., 1985; Melling et al., 1993; Surkov, 2001). Therefore, studies have been concentrated on large deformed ice features and were located in the vicinity of prominent ice sails. This differs from the Antarctic ridges examined in the present study which have been extracted from data aimed at sampling representative sections of the ice cover and where there has been no prior bias toward sampling ridges of a certain morphology. The difference in sampling can bias the data set of Arctic ridges towards large ridges with prominent ice sails and the data set of Antarctic ridges towards average ridges with or without sails. Another issue concerns the

assessment of sail and keel angles from a cross-section of a deformed ice feature. The angle of a sail or a keel to the horizontal (as defined in Fig. 3.7) is highly dependent on the obliqueness at which the cross-section is obtained from the ridge. A cross-section taken perpendicular to the longitudinal direction of the ridge will result in smaller sail and keel angles than a cross-section taken oblique to the longitudinal direction of the ridge. However, since it is not possible to quantitatively assess the effects of these sampling issues with the present data, we proceed with the discussion of the possible causes of the observed differences in ridge morphology assuming that the effects due to sampling are negligible.

3.8.2 Driving forces and ice strength

3.8.2.1 Effects on ridge morphology

Ridging takes place when the internal stress in an ice floe exceeds its strength (Melling and Riedel, 1996). The force balance for an ice floe is a balance between its momentum and internal stress, atmospheric and oceanic stress, ocean tilt and Coriolis force. Since the driving forces provide the energy for ridge building, both magnitude and duration of the forces can affect ridge morphology, with weaker and shorter periods of forcing resulting in smaller ridges.

While driving forces provide the energy, the strength of the ice floes provides resistance to ridge building. The strength of parent ice floes limits the size of the forces that can be transmitted through it, and hence limits the size of the ridge, with stronger parent ice resulting in larger sails and keels (Parmerter and Coon, 1972; Hopkins, 1998; Melling and Riedel, 1996). On the other hand, the strength of the regional ice cover can also play a similar role in limiting ridge size. The amount of work required to increase the size of a ridge increases with the size of the ridge (Hopkins, 1994). As a result, energetics may favour initiating ridging at another location in a weak ice cover, instead of enlarging an existing ridge (Tuhkuri et al., 1999), thus resulting in a large number of small ridges, instead of a small number of large ridges.

3.8.2.2 Arctic and Antarctic comparisons

The large difference between Antarctic and Beaufort ridges and similarity between Antarctic and Arctic temperate ridges can largely be attributed to parent ice thickness. In the central Arctic, including the Beaufort Sea, undeformed first year ice reaches a thickness of 1.6 – 2 m (Wadhams, 1998) and ridges are often formed by breaking of thin refrozen lead ice as it is pushed against thicker first year or multi-year floes (Tucker et al., 1984; Hopkins, 1998). The thicker floe is strong; hence it serves as a platform for the building of a sail and is able to break the lead ice into small blocks. This mechanism results in long linear features that are composed of a large number of relatively thin blocks (Wadhams, 1998). It has been observed in the Weddell (Wadhams, 1998) and Ross seas (Fig. 3.7) that undeformed first year ice has an average thickness of 0.6 – 0.7 m and ridges are composed of few relatively large blocks which are likely to be formed from the deformation of first year ice floes of similar thickness (Fig. 3.11a ; Wadhams, 1998). This is similar to the formation of ridges in the Baltic Sea (Tuhkuri et al., 1998), where level ice thickness reaches 0.4 – 0.7 m (Kankaanpää, 1997) and rafting is an integral part of the ridging process (Hopkins et al., 1999). As a result, the dimensions of Antarctic ridges are more similar to those of Arctic temperate ridges than those of Beaufort ridges.

What other differences are there in the Arctic and Antarctic pack ice in terms of ice strength and driving forces? The internal structure of pack ice from the Southern Ocean and from the central Arctic Ocean is very different. Antarctic ice floes have a complex growth history: frazil (granular) ice in the open water collides and coagulates to form small pancake floes; ocean swell and winds open water up in different regions and increase the chances of rafting which introduces slush, voids and discontinuities in the composite floes (Worby et al., 1998). As a result, granular ice makes up approximately 60% of the sea ice volume in the Southern Ocean (Jeffries et al., 1998; Worby et al., 1998; Lange and Eicken, 1991). This is in sharp contrast to ice from the Arctic Ocean, which is usually more than 70% congelation ice (e.g., Tucker et al., 1985; Weeks and Ackley, 1982) since conditions are calmer due to the land-locked nature of the Arctic Basin and the presence of thick perennial ice (Weeks, 1998). As laboratory experiments

on samples of multiyear sea ice ridges have indicated that structural failure is commonly associated with the presence of large voids and structural discontinuities (Cox and Richter-Menge, 1985), it is likely that Antarctic pack ice floes, composed of discontinuous layers of slush and ice which are not fully frozen together, is weaker than Arctic floes of the same thickness but formed from a single piece of thermodynamically thickened ice. It has been suggested that the calmer conditions in the Arctic Basin are conducive to building up large internal stresses in the ice pack, in contrast to the situation in the Southern Ocean, where the open northern ice edge of the ice pack allows ice to move and dissipate internal forces (Weeks, 1998; Wadhams, 1998).

Is it possible that the differences observed in the morphology of Arctic and Antarctic pressure ridges are due to lower ice strength and lower internal stresses in the Antarctic ice pack? Although there have been a few laboratory studies of the tensile strength of Antarctic sea ice (e.g. Kivimaa, 1999; Richter-Menge et al., 1990) and various field measurements of atmospheric and oceanic stress and ice drift (e.g. Geiger et al., 1998; McPhee et al., 1996; Martinson and Wamser, 1990) there has been no field measurement of the strength or internal stress of Antarctic ice floes. Even though there are insufficient data to fully assess our hypothesis, we follow other studies and use the relationship between keel depth, H_k, and parent ice thickness, t, as a proxy, to compare parent ice strength and ridging forces with studies in the Arctic.

According to Tucker et al. (1984), buckling failure would result in sail height, H_s, being a square root function of parent ice thickness, t:

$$H_s = C\, t^{0.5} \qquad (3.5)$$

where a high value of C indicates a large ridge for a given parent ice thickness, t, and may arise from a high parent ice strength (Melling and Riedel, 1996) or strong driving forces (Kankaanpää, 1997). Fig. 3.12 plots keel depth, H_k, and level ice draft, L, from the Antarctic deformed ice features examined in this study. This is compared to relationships of H_s and block size, b, from other studies, assuming that $H_k = 5\ H_s$, $L = 0.9\ b$ and $b = t$, following Melling and Riedel (1996). The best-fit square root relationship for Antarctic ridges is far lower than those found in studies in the Beaufort and Baltic Seas. Although

differences in sampling may contribute to the observed differences in the relationship between H_k and L, the large discrepancy between Arctic and Antarctic values points strongly towards additional causes and the need for further investigation of the hypothesis that ice strength and driving forces are lower in the Southern Ocean.

3.8.3 Friction of surfaces

Another characteristic of the ice floe is the friction of its surfaces. In a series of simulations in which a thin lead ice sheet is pushed against a thick ice floe, Hopkins (1994) found that ridges with high keel area to sail area ratios were caused by a high above-water friction coefficient. Above-water friction limits sail growth and ice blocks from the buckling of the parent ice sheets are incorporated into the keel, resulting in a high keel area to sail area ratio. Can this mechanism explain the higher keel area to sail area ratio in Antarctic ridges? Based on the assumptions that Antarctic pressure ridges are formed from the deformation of ice floes of similar thickness and that Arctic pressure ridges are formed from the deformation of refrozen lead ice, it is possible that a difference in above-water friction coefficient can arise as a result of the difference in age and formation mechanisms of Antarctic ice floes and Arctic lead ice. The complex and dynamic growth history of ice floes in the Southern Ocean (see section 7.2) results in a large amount of small scale roughness on the surface of ice floes. Snow may also add to the above-water friction by increasing contact area. The above-water friction of a new sheet of lead ice without any significant deformation or snow accumulation is likely to be low. Under this scenario, it is possible that the above-water friction is high when old Antarctic ice floes are ridged and the above-water friction is low when young Arctic lead ice is ridged, resulting in ridges with larger keel area to sail area ratios in the Antarctic.

3.8.4 Other considerations

Although there is no strong evidence for a plausible cause of the differences in slope

angles, an issue that should be considered is the number of blocks within ridges. Large piles of granular material exhibit consistent slope angles (or angle of repose) due to the balance between friction, weight and, in the case of submerged ice blocks, buoyancy. However, in the extreme case of a ridge sail composed of a single block of ice, its slope angles, as defined by the angle between the horizon and it apex, does not reflect the angle of repose and should not be compared to slope angles of ridge sails made of a large number of blocks. There are currently no quantitative data on the number of blocks in Arctic or Antarctic ridges, but if Antarctic ridges are indeed composed of a few relatively large blocks and Arctic ridges are composed of many relatively small blocks, then values of Antarctic ridge slope angles and comparison with those from Arctic ridges may not be meaningful.

It is important to bear in mind that, although the results of the present study have shown differences in the morphology of Antarctic pressure ridges and Arctic pressure ridges, it does not necessarily mean that small ridges and ridges with no sails, similar to those in the Antarctic, do not exist in the Arctic. Compared to the average or the large ridge, these ridges pose little difficulty to traffic and offshore structures and perhaps, as a result, they are of little interest and are seldom studied.

The formation of a coupled ridge or a widowed ridge is likely to be determined by the homogeneity of the parent ice sheets. This is supported by laboratory experiments which show that ice sheets which are homogeneous in terms of strength or internal structure are more likely to remain intact over the keel, instead of fracturing and forming an ice sail (Tuhkuri et al., 1998).

3.9 Conclusions

From drilling profile data obtained in the Ross, Amundsen, Bellingshausen and Weddell seas, we identified snow sails, ice sails and keels from the snow, ice top surface and ice bottom surfaces, respectively, and found that not all keels are associated with sails and not all sails are associated with keels. We identified 42 deformed ice features, each

comprised of a keel and any associated sails, and classified them into three types according to their shapes. Coupled ridges have triangular keels and sails and, with a mean maximum keel depth of 3.61 m, they are the most massive of the deformed ice features. Widowed ridges have a triangular keel similar to those of coupled ridges but do not have a prominent ice sail. With a mean ridge width of 15 m, they are the narrowest of the deformed ice features. Rubble piles are the widest, but they contribute least to the total ice mass. However, approximating the thickness of a rubble pile by surrounding level ice still underestimates the total ice mass by nearly 40%. For the purpose of estimating ice thickness from surface observations, we believe hydrostatic equilibrium is a fair assumption on large scales. However we caution against applying hydrostatic equilibrium over the surface area occupied by individual ridge sails to estimate ice thickness, as hydrostatic equilibrium is not maintained on the scale of sails. Until more data are available, statistical relationships between variables that can be observed from the surface and variables that are hidden from the surface are not sufficiently strong and consistent for the estimation of ice thickness. Last but not least, the effect that not all keels are associated with a sail and not all sails are associated with a keel should be addressed when estimating ice thickness from surface observations, regardless of whether a physical or statistical argument is used.

Comparisons between Antarctic and Arctic first year ridges indicate that Antarctic ridges are flatter and less massive than their Arctic counterparts. Differences are greater when compared to ridges in the Beaufort Sea than those in the Arctic temperate regions. We propose a number of hypotheses which, in addition to differences arising from sampling strategies, may explain the differences between the morphology of Arctic and Antarctic ridges. First, Arctic temperate and Antarctic ridges are both formed by the rafting and ridging of first year floes; therefore they are similar in size and smaller than the ridges in the Beaufort Sea, which are built from young lead ice as it is pushed against thick first year or multi-year floes. Second, higher surface friction on Antarctic parent ice causes a higher keel area to sail area ratio in Antarctic pressure ridges than in Arctic pressure ridges. Third, lower ice strength and driving forces result in smaller and flatter

ridges in the Southern Ocean.

3.10 Acknowledgments

This study was funded by National Science Foundation grant OPP-9614844 and a Global Change Student Research Grant from the Center for Global Change and Arctic System Research, University of Alaska Fairbanks. The authors are grateful to H. Eicken for providing the data from the WWGS and EPOS cruises. Thanks to the crew and officers of the R.V. Polarstern and the R.V. Nathaniel B. Palmer for the success of the WWGS, EPOS and NBP cruises. Many thanks to all those who participated on these cruises and helped to drill and measure 18 864 holes. These include but are not limited to: P. Wadhams, M.P. Casarini, K. Claffey, C. Garrity, T. Maksym, N. Kozlenko, K. Morris and Antarctic Support Associates personnel. Sincere thanks to K. Echelmeyer and H. Eicken for their comments on earlier drafts, J. Tuhkuri, M. Hopkins, B. Hibler, and A. Kovacs for their thought-provoking discussions, and two anonymous reviewers for their help in refereeing this paper.

3.11 Figures

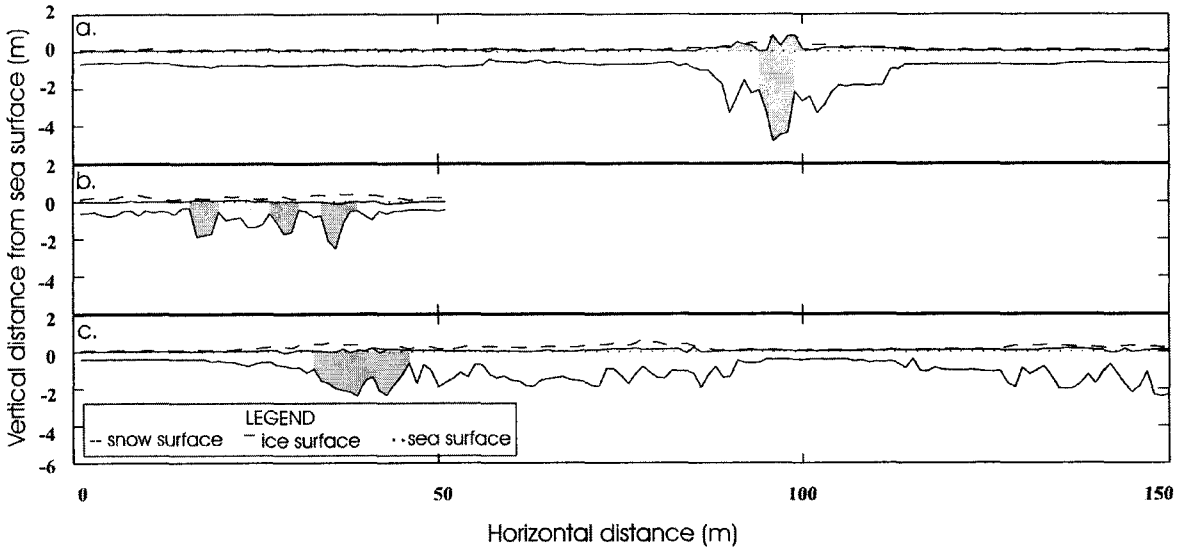

Figure 3.1 Application of the Rayleigh criterion to drill profiles. The three drill profiles were obtained from the Ross Sea. Shaded areas indicate sail and keel areas as defined by the Rayleigh criterion.

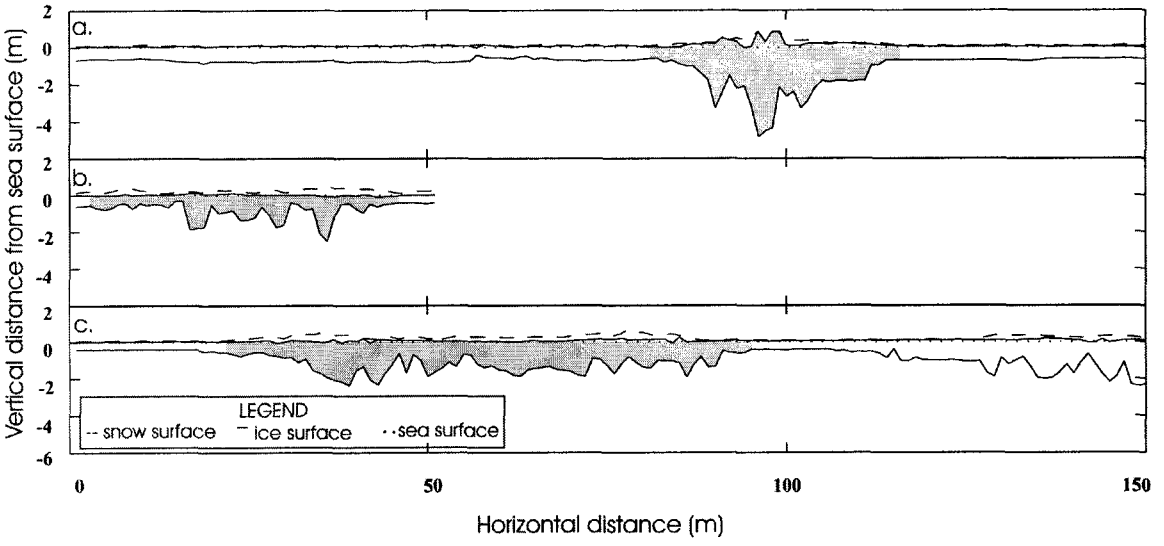

Figure 3.2 Application of the ridge identification scheme used in this study, to drill profiles. Shaded areas indicate sail and keel areas as defined by the identification scheme

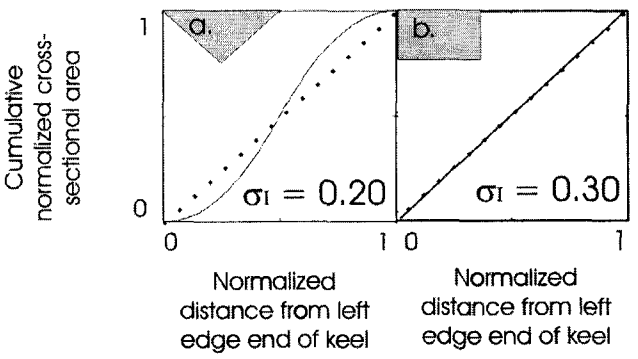

Figure 3.3 Inclusive Graphic Standard Deviations for idealized geometrical shapes. Curves of cumulative normalized cross-sectional area versus normalized horizontal distance along the keel and Inclusive Graphic Standard Deviation, σ_I, for **a.** a perfect triangle, and **b.** a perfect rectangle.

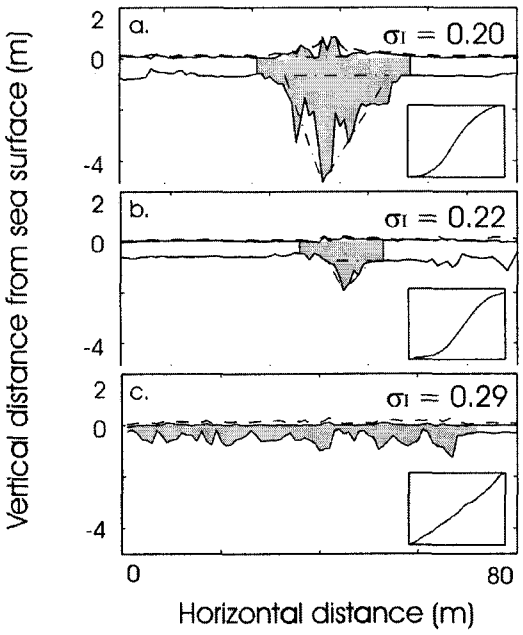

Figure 3.4 Inclusive Graphic Standard Deviations for deformed ice features. Curves of cumulative normalized cross-sectional area versus normalized horizontal distance along the keel and Inclusive Graphic Standard Deviations, σ_I, for **a.** a coupled ridge with a triangular keel, **b.** a widowed ridge with a triangular keel, and **c.** a rubble pile with a non-triangular keel.

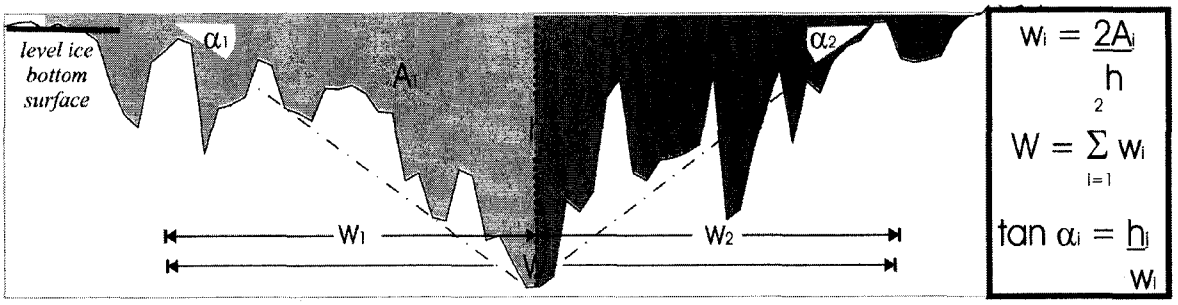

Figure 3.5 Definition of keel width, *W*, and slope angles, α, following Kankaanpää (1997). Sail widths and slope angles are calculated similarly from features above level ice top surface.

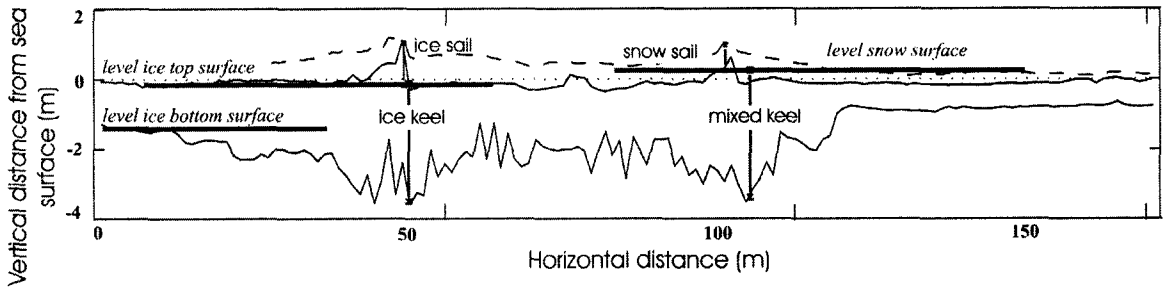

Figure 3.6 Definition of sails, keels and level surfaces as used in this study.

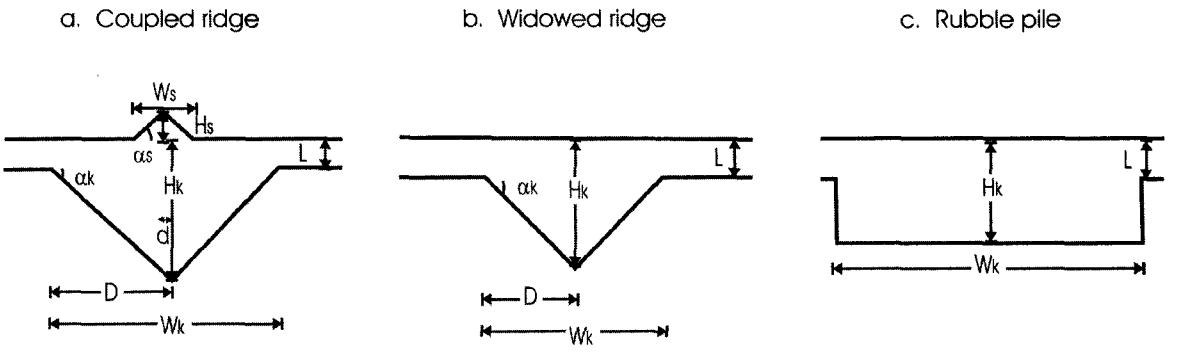

Variable	Coupled ridge	Widowed ridge	Rubble pile
Ice keel width, W_k (m)	27±17	15±10	43±22
Maximum ice keel depth, H_k (m)	3.61±1.82	1.82±0.48	2.14±0.88
Mean ice keel depth (m)	2.41±1.02	1.40±0.34	1.12±0.54
Distance of keel crest from left edge, D (W_k)	0.46±0.17	0.52±0.14	-
Ice keel angles, α_k (°)	15±8	12±5	-
Ice sail width, W_s (m)	8±3	-	9±3
Maximum ice sail height, H_s (m)	0.62±0.28	-	0.69±0.31
Mean ice sail height (m)	0.22±0.13	-	0.26±0.13
Distance between sail crest and keel crest, d (W_k)	0.01±0.13	-	-
Ice sail angles, α_s (°)	10±5	-	-
Mean level ice thickness (m)	0.75±0.28	0.57±0.14	0.65±0.23
Mean thickness of feature (m)	2.58±1.11	1.54±0.35	1.19±0.57
% underestimation by level approximation (%)	55±17	44±13	39±18
Number of samples	12	13	17

Figure 3.7 Morphology of Antarctic deformed ice features. Ideal cross-sectional profiles of Antarctic deformed ice features and summary of their physical dimensions. Physical dimensions are described by mean and +/- 1 standard deviation.

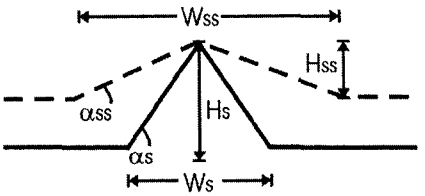

Variable	Snow sails which are associated with an ice sail, ss	Ice sails which are associated with a snow sail, s
Width, W (m)	17±11	8±4
Maximum height, H (m)	0.51±0.31	0.70±0.30
Mean height (m)	0.07±0.06	0.25±0.16
Angles, α (°)	6±3	12±4
Area (m^2)	1.3±1.5	2.4±2.5

Figure 3.8 Summary of physical dimensions of snow and ice sails.

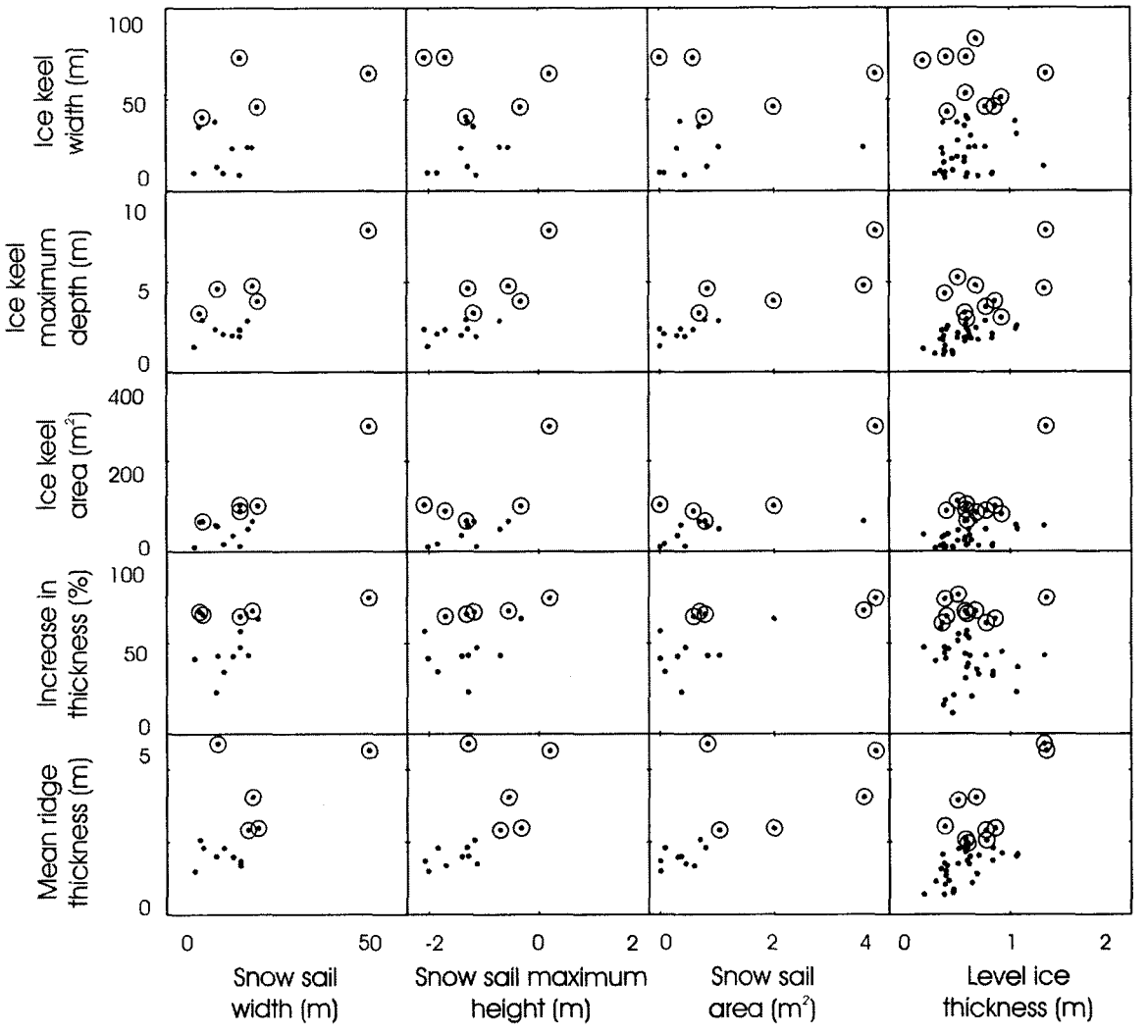

Figure 3.9 Scatterplots of the relationships between surface variables and hidden variables. Surface variables are on the horizontal axis while hidden variables are on the vertical axis. Circles indicate the five or ten largest outliers in the hidden variable in each case.

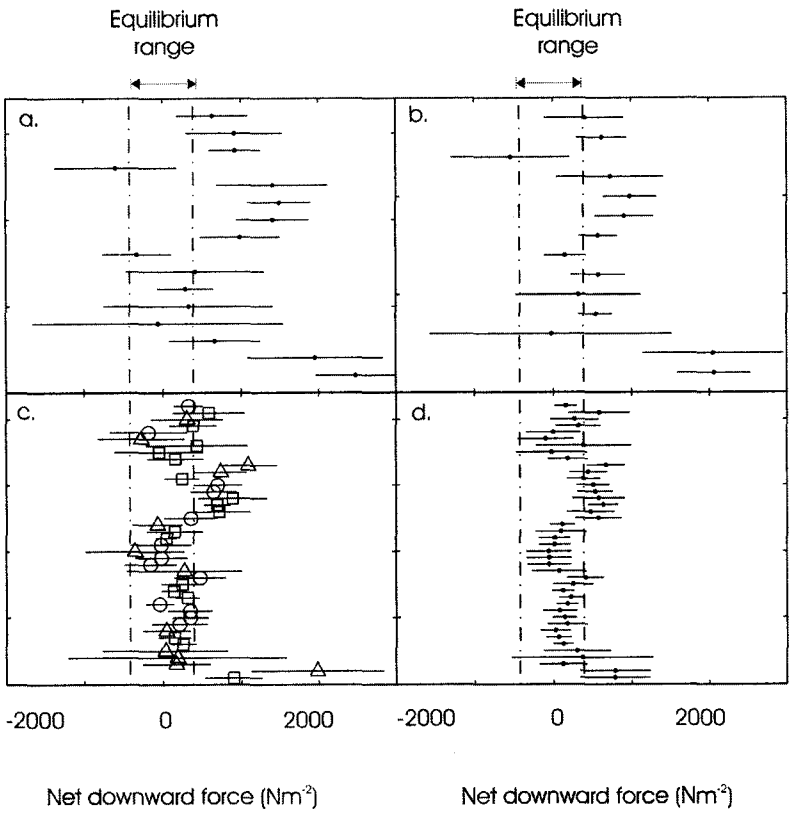

Figure 3.10 The net force over different parts of deformed ice features. Fig. **a.** denotes the net force over the part of the deformed ice features denoted by ice sail. Fig. **b.** denotes the net force over the part of the deformed ice features denoted by snow sail. Fig. **c.** denotes the net force over the part of the deformed ice features denoted by keel. Fig **d.** denotes the net force over the entire length of transect. (•) indicates mean net force over each deformed ice feature. (△), (○) and (□) indicate mean net force over a coupled ridge, widowed ridge and rubble pile respectively. Error bars indicate net forces including an error margin of 20% for ρ_{sl}, ρ_s, z_s, z_f and α, and 5% for ρ_w and ρ_i.

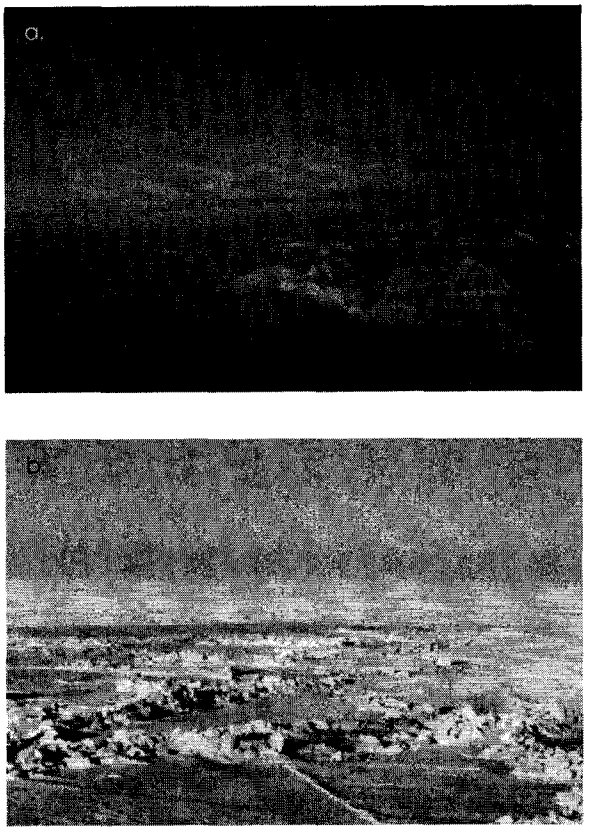

Figure 3.11 Examples of pressure ridges in the Southern Ocean sea ice cover. Fig. **a.** is taken in the Ross Sea. Ridges appear to be point type roughnesses with a small number of fairly thick blocks. Fig. **b.** is taken in the East Antarctic. Ridges appear to be short linear features which delineate the edges of ice floes. Fig. b from Worby et al. (1999).

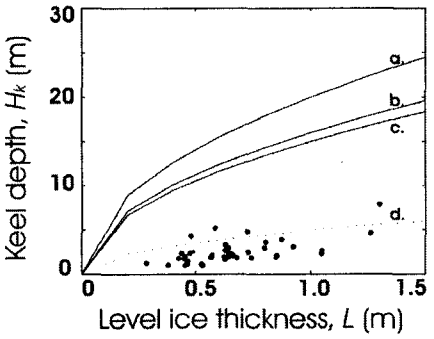

Figure 3.12 Relationships between keel depth, H_k, and level ice thickness, L. Curve **a.** indicates $H_k = 20\ L^{0.5}$, which is the best-fit for a set of ridges in the Beaufort Sea (Tucker et al., 1984). Curve **b.** indicates $H_k = 16\ L^{0.5}$, which is the best-fit for a set of ridges in the Beaufort Sea (Melling and Riedel, 1996). Curve **c.** indicates $H_k = 15\ L^{0.5}$, which is the best-fit for a set of ridges in the Baltic Sea (Kakaanpää, 1997). Curve **d.** indicates $H_k = 5\ L^{0.5}$, which is the best-fit for the Antarctic deformed ice features in this study. (•) indicate values for each Antarctic deformed ice feature.

3.12 Tables

Table 3.1 Summary of data sources

Cruise	Season	Month	Year	Region	No. of first year profiles ≥ 50m	Total length of first year profiles ≥ 50m (m)
NBP99-1	Summer	Jan	1999	Ross / Amundsen seas	19	2719
NBP 95-3	Autumn	May – June	1995	Ross Sea	49	3592
NBP 98-3	Autumn	May – June	1998	Ross Sea	24	3253
WWGS 92	Early winter	July	1992	Weddell Sea	2	124
NBP 95-5a	Winter	Aug	1995	Ross Sea	28	2081
NBP 95-5b	Late winter / Early spring	Aug – Sep	1995	Amundsen / Bellingshausen seas	26	1928
WWGS 89	Early spring	Sep – Oct	1989	Weddell Sea	49	4562
EPOS	Spring	Oct – Nov	1988	Northwest Weddell Sea	7	605
TOTAL					**204**	**18 864**

Table 3.2 Values of ρ_s used for examining isostasy

Cruise	ρ_s (kg m^{-3})	Source
NBP99-1	400	Morris and Jeffries, 2001
NBP 95-3	350	Adolphs, 1998
NBP 98-3	311	Morris and Jeffries, 2001
WWGS 92	342	estimated from Eicken et al., 1994[a]
NBP 95-5a	400	Adolphs, 1998
NBP 95-5b	370	Adolphs, 1998
WWGS 89	302	Eicken et al., 1994
EPOS	341	estimated from Eicken et al., 1994[a]

[a] Values of ρ_s estimated, assuming hydrostatic equilibrium, from the mean values of z_s, z_i, z_f, given for all the drill data taken from the cruise.

Table 3.3 Dimensions of Antarctic and Arctic pressure ridges

Variable	Antarctic		Arctic[a]	
	Coupled ridge	Widowed ridge	Temperate	Beaufort
Keel width, W_k (m)	27±17	15±10	21±11	62±29
Maximum keel depth, H_k (m)	3.65±1.82	1.85±0.49	5.40±3.08	12.76±5.96
Keel angle, α_k (°)	15±8	12±5	28±14	26±14
Keel area, A_k (m^2)	73±72m	23±18	113±126	162±61
Associated sail width, W_s (m)	8±4	-	7±5	21±14
Maximum associated sail height, H_s (m)	0.65±0.29	-	1.27±0.70	3.11±1.59
Associated sail angle, α_s (°)	10±5	-	21±11	33±10
Associated sail area, A_s (m^2)	2±2	-	16±17	25±22
Level ice thickness (m)	0.75±0.28	0.57±0.14	0.79±0.46	1.52±1.20
Keel depth / Associated sail height, H_k/H_s	5.6±1.8	-	4.8±2.2	4.5±1.3
Keel area / Associated sail area, A_k/A_s	35.8±17.3	-	9.8±8.8	8.6±3.7
Keel width / Keel depth, W_k/H_k	8.0±4.7	7.7±3.2	5.3±2.4	4.4±2.0
Keel width / Associated sail height, W_k/H_s	43.1±24.4	-	20.6±10.8	19.6±7.2

[a] after Burden and Timco (1995)

3.13 References

Adolphs, U. 1999. Roughness variability of sea ice and snow cover thickness profiles in the Ross, Amundsen, and Bellinghausen Seas. J. Geophys. Res., 104(C6), 13,577-13,591.

Adolphs, U. 1998. Ice thickness variability, isostatic balance and potential for snow ice formation on ice floes in the south polar Pacific Ocean. J. Geophys. Res., 103(C11), 24,675-24,691.

Allison I. and Worby A. 1994. Seasonal changes of sea-ice characteristics off East Antarctica. Ann. Glaciol., 20, 195-201.

Allison, I., Brandt, R.E. and Warren, S.E. 1993. East Antarctic sea ice: albedo, thickness distribution, and snow cover. J. Geophys. Res., 98(C7), 12,417-12,429.

Bowen, R.G. and Topham, D.R. 1996. Study of the morphology of a discontinuous section of a first year arctic pressure ridge. Cold Reg. Sci. Technol., 24(1), 83-100.

Burden, R.and Timco, G.W. 1995. A catalogue of sea ice ridges. National Research Council of Canada Report TR-1995-27, Ottawa, Ontario.

Cox, G.F.N. and Richter-Menge, J.A. 1985. Tensile strength of multiyear pressure ridge sea ice samples. J. Energy Resources Technol., 107(3), 375-380.

Davis, N.R. and Wadhams, P. 1995. A statistical analysis of Arctic pressure ridge and morphology. J. Geophys. Res., 100(C6), 10,915-10,925.

Dierking, W. 1995. Laser profiling of the ice surface topography during the Winter Weddell Gyre Study 1992. J. Geophys. Res., 100(C3), 4,807-4,820.

Eicken, H., Lange, M.A., Hubberten, H.-W., Wadhams, 1994. Characteristics and distribution patterns of snow and meteoric ice in the Weddell Sea and their contribution to the mass balance of sea ice. Annales Geophysicae, 12, 80-93.

Folk, R.A. and Ward, W.C. 1957. Brazos river bar: a study in the significance of grain size parameters. J. Sedimentary Petrology, 27(1), 3-26.

Geiger, C.A., Ackley, S.F. and Hibler, W.D. III. 1998. Sea ice drift and deformation processes in the western Weddell Sea. In: M. O. Jeffries (ed.) Antarctic sea ice:

physical processes, interactions and variability, 141-160.

Granberg, H.B. and Leppäranta, M. 1999. Observations of sea ice ridging in the Weddell Sea. J. Geophys. Res., 104(C11), 25,735-25,745.

Hibler, W.D. III, Mock, S.J. & Tucker, W.B. III. 1974. Classification and variation of sea ice ridging in the western Arctic Basin. J. Geophys. Res., 79(18), 2 735-2 743.

Hopkins, M.A. 1998. Four stages of pressure ridging. J. Geophys. Res., 103(C10), 21,883-21,891.

Hopkins, M.A. 1994. On the ridging of intact lead ice. J. Geophys. Res., 99(C8), 16,351-16,360.

Hopkins, M.A., Tuhkuri, J. and Lensu, M. 1999. Rafting and ridging of thin ice sheets J. Geophys. Res., 104(C6), 13,605-13,613.

Høyland, K.V. 2002. Simulations of the consolidation process in first-year sea ice ridges. Cold Reg. Sci. Technol., 34, 143-158.

Høyland, K.V. and Løset, S. 1999. Measurements of temperature distribution, consolidation and morphology of a first-year sea ice ridge. Cold Reg. Sci. Technol., 29, 59-74.

Jeffries, M.O. and Weeks, W.F. 1992. Structural characteristics and development of sea ice in the western Ross Sea. Ant. Sci. 5 (1), 63-75.

Jeffries, M.O., Li, S., Jaña, R.A., Krouse, H.R. and Hurst-Cushing, B. 1998. Late winter first-year ice floe thickness variability, seawater flooding and snow ice formation in the Amundsen and Ross seas. In: M.O. Jeffries (ed.) Antarctic sea ice: physical processes, interactions and variability, 69-87.

Kankaanpää, 1997. Distribution, morphology and structure of sea ice pressure ridges in the Baltic Sea. Fennia, 175(2), 139-240.

Kankaanpää, 1989. Structure of first year pressure ridges in the Baltic Sea. Proc. 10th International Conf. on Port and Ocean Engineering under Arctic Conditions. POAC '89, June 12-16. Lulea, Sweden. Vol. 1, 87-102.

Kirillov, A.A. 1957. Correction for hummocking in the calculation of ice volume. [Uchet

torosistosti pri opredelenii ob"ema l'da] *Problemy Arktiki*, No. 2, 53-58.

Kivimaa, S. 1999. Field experiments on uniaxial compressive strength of sea ice in the Weddell Sea, Antarctica. Proc. 15th International Conf. on Port and Ocean Engineering under Arctic Conditions. POAC '99, August 23-26, 1999, Espoo, Finland. Vol.3, 964-973.

Kovacs, A. 1972. On pressured sea ice. Proc. of International Conf. on Sea Ice, May 10-13, 1971. Reykjavik, Iceland, 276-295.

Lange, M.A. and Eicken, H. 1991. The sea ice thickness distribution in the northwestern Weddell Sea. J. Geophys. Res., 96(C3), 4,821-4,837.

Leppäranta, M. 1981. Statistical features of sea ice ridging in the Gulf of Bothnia. *Research report no. 32, Winter Navigation Research Board.* Helsinki Government Printing Office. 46pp.

Leppäranta, M. and Hakala, R. 1992. The structure and strength of first-year ice ridges in the Baltic Sea. , Cold Reg. Sci. Technol., 20(3), 295-311.

Leppäranta, M. and Palosuo, E. 1981. Studies of sea ice ridging with a ship-borne laser profilometer. Proc. 6th International Conf. on Port and Ocean Engineering under Arctic Conditions, POAC '81, July 27-31, Québec, Canada, 1,031-1,037.

Lowry, R.T. and Wadhams, 1979. On the statistical distribution of pressure ridges in sea ice. J. Geophys. Res., 84(C5), 2,487-2,494.

Lytle, V.I. and Ackley S.F. 1991. Sea ice ridging in the Eastern Weddell Sea. J. Geophys. Res., 96(C10), 18,411-18,416.

Lytle, V.I., Worby, A.P. and Masson R.A. 1998. Sea-ice pressure ridges in East Antarctica. Ann. Glaciol. 27, 449-454.

Martinson, D.G. and Wamser, C. 1990. Ice drift and momentum exchange in winter Antarctic pack ice. J. Geophys. Res. 95 (C2), 1,741-1,755.

McPhee, M.G., Ackley, S.F., Guest, P., Huber, B.A., Martinson, D.G., Morison, J.H., Muench, R.D., Padman, L. and Stanton, T.P. 1996. The Antarctic Zone Flux Experiment, Bull. of Am. Met. Soc. 77 (6), 1,221-1,232.

Melling,H. and Riedel, D.A. 1996. Development of seasonal pack ice in the Beaufort Sea during the winter of 1991-1992: a view from below. J. Geophys. Res., 101(C5), 11,975-11,991.

Melling, H. and Riedel, D.A. 1995. Underside topography of sea ice over the continental shelf of the Beaufort Sea in the winter of 1990. J. Geophys. Res., 100(C7), 13,641-13,653.

Melling, H., Topham, D.R. and Riedel, D.A. 1993. Topography of the upper and lower surfaces of 10 hectares of deformed sea ice. Cold Reg. Sci. Technol., 21(4), 349-369.

Morris, K. and Jeffries, M.O. 2001. Seasonal contrasts in snow cover characteristics on Ross Sea ice floes. Ann. Glaciol. (33), 61-68.

Parmerter, R.R. and Coon, M.D. 1972. Model of pressure ridge formation in sea ice. J. Geophys. Res., 77(33), 6,565-6,575.

Parmerter, R.R. 1975. Model of simple rafting in sea ice. J. Geophys. Res., 80(15), p.1948-1952.

Richter-Menge, J.A., Ackley, A.F. and Lange, M.A. 1990. Comparison of the compressive strength of Antarctic frazil ice and laboratory-grown columnar ice. CRREL Monograph, 90-1, 79-84. U.S. Army Cold Regions Research and Engineering Laboratory Hanover, New Hampshire.

Steiner, N., Harder, M. and Lemke, P. 1999. Sea-ice roughness and drag coefficients in a dynamic-thermodynamic sea-ice model for the Arctic. Tellus, 51A(5), 964-978.

Strass, V.H. and Fahrbach, E. 1998. Temporal and regional variation of sea ice draft and coverage in the Weddell Sea obtained from upward looking sonars. In: M. O. Jeffries (ed.) Antarctic sea ice: physical processes, interactions and variability, 123-139.

Surkov, G.A. 2001. Internal structure of first-year hummocks. Proc. 11th International Offshore and Polar Engineering Conf. ISOPE 2001, June 17-22, 2001, Stavanger, Norway. Vol. 1, 796-798.

Timco, G.W. and Burden, R.1997. An analysis of the shapes of sea ice ridges. Cold Reg. Sci. Technol., 25, 65-77.

Tin, T. and Jeffries, M.O. 2001. Quantitative identification of Antarctic first year pressure ridges and preliminary results on ridge morphology. Proc. 16th International Conf. on Port and Ocean Engineering under Arctic Conditions. POAC '01, August 12-17, 2001, Ottawa, Canada. Vol. 3, 1,455-1,464.

Tucker, W.B., Gow, A.J. and Weeks, W.F. 1985. Pressure ridge morphology and physical properties of sea ice in the Greenland Sea. Proc. Arctic Oceanography Conf. and Workshop, June 11-14, 1985, Hattiesburg, MS. 214-223.

Tucker, W.B., Sodhi, D.S. and Govoni, J.W. 1984. Structure of first-year pressure ridge sails in the Prudhoe Bay region. In: P. Barnes, D.M. Schell and E. Reimnitz (eds.) The Alaskan Beaufort Sea: ecosystems and environments, Orlando, Academic Press, 115-135.

Tucker, W.B., Weeks, W.F. and Frank, M.D. 1979. Sea ice ridging over the Alaskan continental shelf. J. Geophys. Res., 84 (C 8), 4,885-4,897.

Tuhkuri, J., Lensu, M. and Saarinen, S. 1999. Laboratory and field studies on the mechanics of ice ridge formation. Proc. 15th International Conf. on Port and Ocean Engineering under Arctic Conditions. POAC '99, August 23-26, 1999, Espoo, Finland. Vol. 3, 1,118-1,129.

Tuhkuri, J., Lensu, M. and Hopkins, M.A. 1998. Laboratory and field studies on ridging of an ice sheet. Proc. 14th IAHR Ice Symp., Balkema, Rotterdam. Vol. 1, 397-404.

Wadhams, P. 1998. Sea ice morphology. In: M. Leppäranta (ed.) Physics of ice-covered seas: lecture notes from a summer school in Savonlinna, Finland 6-17 June, 1994. University of Helsinki, Department of Geophysics, 1998, Vol. 1, 231-287.

Wadhams, and Davy, T. 1986. On the spacing and draft distributions for pressure ridge keels. J. Geophys. Res. 91(C9), 10,697-10,708.

Wadhams, P. and Horne, R.J. 1980. An analysis of ice profiles obtained by submarine sonar in the Beaufort Sea. *J. Glaciol.*, 25(93), 401-424.

Wadhams, P., Lange, M.A. and Ackley, S.F. 1987. The ice thickness distribution across the Atlantic sector of the Antarctic ocean in midwinter. J. Geophys. Res. 92(C13),

14,535-14,552.

Weeks, W.F. 1998. Growth conditions and the structure and properties of sea ice. In: M. Leppäranta (ed.) Physics of ice-covered seas: lecture notes from a summer school in Savonlinna, Finland 6-17 June, 1994. University of Helsinki, Department of Geophysics, 1998, Vol. 1, 25-104.

Weeks, W.F. and Ackley, S.F. 1982. The growth, structure, and properties of sea ice. CRREL monograph, 82- 1, U.S. Army Cold Regions Research and Engineering Laboratory Hanover, New Hampshire. 130pp.

Weeks, W.F., Ackley, S. F. and Govoni, J. 1989. Sea-ice ridging in the Ross Sea, Antarctica, as compared with sites in the Arctic. J. Geophy. Res., 94(C4), 4,984-4,988.

Weeks, W.F., Kovacs, A. and Hibler, W.D. III 1978. Pressure ridge characteristics in the Arctic coastal environment. Proc. 1st International Conference on Port and Ocean Engineering under Arctic Conditions. POAC '71, August 23-30, 1971, Trondheim, Norway. Vol. 1,152-183.

Williams, E., Swithinbank, C. and de Q. Robin, G. 1975. A submarine sonar study of Arctic pack ice. J. Glaciol., 15(73), 349-362.

Wittmann, W.I. and Schule, J.J., Jr. 1967. Comments on the mass budget of Arctic pack ice. Proc. of Symp. on the arctic heat budget and atmospheric circulation. Dec. 1966, 215-246.

Worby, A.1999. Observing Antarctic sea ice: A practical guide for conducting sea ice observations from vessels operating in the Antarctic pack ice. A CD-ROM produced for the Antarctic Sea Ice Processes and Climate (ASPeCt) program of the Scientific Committee for Antarctic Research (SCAR) Global Change and the Antarctic (GLOCHANT) program, Hobart, Australia.

Worby, A. and Ackley, S.F. 2000. Antarctic research yields circumpolar sea ice thickness data. Eos Transactions, American Geophysical Union, 81(17):181, 184-185.

Worby, A. and Allison, I. 1999. A technique for making ship-based observations of

Antarctic sea ice thickness and characteristics. Part I Observational technique and results. Antarctic CRC Research Report, No. 25.

Worby, A.P., Massom, R.A., Allison, I., Lytle, V.I. and Heil, P. 1998. East Antarctic sea ice: a review of its structure, properties and drift. In: M.O. Jeffries (ed.) Antarctic sea ice: physical processes, interactions and variability, Antarctic Research Series (74), 41-67, AGU, Washington, DC.

Worby, A., Jeffries, M.O., Weeks, W.F., Morris, K. and Jaña, R. 1996. The thickness distribution of sea ice and snow cover during late winter in the Bellingshausen and Amundsen Seas, Antarctica. J. Geophys. Res., 101(C12), 28,441-28,455.

Zubov, N. N. 1963. Arctic ice. U.S. Navy Electronics Laboratory, San Diego, CA. 491 pp.

Chapter 4

Estimating the thickness of ridged sea ice from ship observations in the Ross Sea, Antarctica*

4.1 Abstract

Ship-based observations of sea ice thickness using the Antarctic Sea Ice Processes and Climate (ASPeCt) protocol provide information on ice thickness distribution at relatively low cost. This protocol uses a simple formula to calculate the mass of ice in ridges based on surface observations. We present two new formulae and compare these with results from the "Original" formula using data obtained in the Ross Sea in autumn and winter. The new "r-star" formula uses a more realistic ratio of sail and keel areas to transform dimensions of sails to estimates of mean keel areas. As a result, estimates of "equivalent thickness" (i.e., mean thickness of ice in ridged areas) increased by over 200%. The new "Probability" formula goes one step further, by incorporating the probability that a sail is associated with a keel underwater, and the probability that keels may be found under level surfaces. This resulted in estimates of equivalent thickness comparable with the Original formula. Estimates of equivalent thickness at one or two degree latitude resolution are sufficiently accurate for validating sea ice models. Although ridges are small features in the Ross Sea, we have shown that they constitute a significant fraction of the total ice mass.

4.2 Introduction

A thorough understanding of the sea ice thickness distribution around Antarctica is essential for validating climate models and for detecting any responses of sea ice to

* Tin, T., Jeffries, M.O., Lensu, M. and J. Tuhkuri. 2003. Antarctic Science 15(1), 47-54.

climate change. Field expeditions dedicated to measuring sea ice thickness in the Southern Ocean are expensive and relatively infrequent, but observations of ice thickness can be made from any vessel traveling through the ice pack, and can provide information on the ice thickness distribution at relatively low cost, and potentially comprehensive spatial and temporal coverage. With the goal of defining a climatology of the sea ice thickness distribution in the Southern Ocean, the Antarctic Sea Ice Processes and Climate (ASPeCt) program of the Scientific Committee on Antarctic Research (SCAR) Global Change and the Antarctic Program (GLOCHANT) developed a standard protocol for recording snow and ice thickness observations from ships (Worby 1999, Worby & Ackley 2000). According to this protocol, the thicknesses of level ice and snow cover are estimated as ice floes turn on their sides next to the ship. However, the thickness of pressure ridges cannot be estimated directly, as they tend to break apart rather than turn on their sides. It is therefore necessary to infer the mean thickness of ice in ridged areas, which we refer to as the "equivalent ice thickness", from the size and shape of surface features.

The aim of our study is to modify the existing formula (the "Original formula") for estimating equivalent thickness from ASPeCt ship observations data (Worby & Allison 1999). The modifications are based on previously unavailable information on pressure ridge morphology. The new formulae use a more realistic ratio of sail and keel areas to transform dimensions of sails to estimates of mean keel areas, and also incorporate the probability that a sail is associated with a keel underwater, and the probability that keels may be found under level surfaces. We then apply the Original and the new formulae to ship observations data and compare the estimate of equivalent thickness from the different formulae to examine the effects of incorporating the new information on ridge morphology on equivalent thickness.

4.3 Previous work and existing methodology

4.3.1 Previous work

Estimating the amount of sea ice underwater from surface observations has been a long-standing problem. In studies where concurrent measurements of freeboard and ice thickness were not available, it was common practice to assume that each ridge sail was hydrostatically balanced by a keel and then estimate the volume of the keel from the volume of the sail (e.g., Zubov 1944, Kirillov 1957, Hibler et al. 1974, Leppäranta 1981). Snow and ice densities and sail and keel porosities are key parameters in these calculations but field-derived values were not always available in these studies.

In studies where concurrent measurements of freeboard and ice thickness were available, the mean state of hydrostatic equilibrium is represented by the ratio between mean draft and freeboard obtained from field data, removing the need for parameterization of densities and porosities. These ratios were first quantified for 20 and 50 km sections of coincident airborne laser/lidar and submarine sonar data for Arctic ice (Comiso et al., 1991, Wadhams *et al.* 1992). Subsequently they have been derived from drill data obtained around ridges only and applied to geometrical models of individual ridge sails to estimate equivalent thickness from laser profiling data (Dierking 1995) and ship observations data (Worby & Allison 1999).

Sails, as recorded by surface observations, are features on the ice surface in the absence of snow, and are features on the snow surface in the presence of snow. In all previous studies, the presence of a sail on the top surface (a feature we refer to as the "snow sail") was taken to imply the presence of a sail on the ice surface (a feature we refer to as the "ice sail") and the presence of a keel. In a few studies, the volume of snow in the snow sail was explicitly calculated and removed when estimating the amount of ice in the ridge (e.g., Leppäranta 1981) but in most studies, the volume of snow was assumed to be negligible (e.g., Wadhams *et al.* 1992).

4.3.2 ASPeCt protocols and the Original formula for estimating equivalent thickness

According to the ASPeCt protocol, a standard set of observations is made hourly by an observer on the ship's bridge. These include the ship's position and total ice concentration, and an estimate of the areal coverage, thickness, floe size, topography (i.e., areal coverage and mean height of ridge sails) and snow cover of the three thickest ice types within a radius of approximately 1 km of the ship. The mean thickness of ice in ridged areas is estimated from the areal coverage and mean height of snow sails, and the surrounding level ice thickness. The geometric model that is used is shown in Fig. 4.1. Each unit area of a ridged floe comprises three distinct components: a base layer of level ice thickness, z_u, a sail represented by a triangle with a height, S, and areal coverage, R; and a keel of no prescribed shape. The cross-sectional area of the snow sail is $0.5RS$ and the cross-sectional area of the keel is r' times that of the snow sail. The average, or equivalent, thickness, z_r, can then be calculated according to

$$z_r = 0.5RS(r'+1) + z_u \qquad [4.1]$$

The amount of ice in the snow sail is exactly $0.5RS$ when there is no snow. The parameter r' is the ratio of ice below and above the sea level in ridged areas, as derived from drill hole measurements around ridges on ice floes, and is used as a proxy for the ratio of ice below and above the base layer (Worby & Allison 1999). It is a representation of the average state of hydrostatic equilibrium in ridged areas and has been calculated to be 4.3 for the East Antarctic sea ice cover (Worby & Allison 1999).

4.4 New aspects of ridge morphology

4.4.1 Limitations of hydrostatic equilibrium

Field studies have shown that although local hydrostatic imbalance is common (e.g., Weeks et al. 1971), hydrostatic equilibrium must be maintained on all floating ice floes

(Bowen & Topham 1996). Since keels are wider than snow sails (e.g., Kovacs 1972, Timco & Burden 1995, Kankaanpää 1997), hydrostatic equilibrium across a keel is maintained between the keel, its sail and the surrounding level ice above the keel. If the amount of ice underwater is estimated to be the volume that is needed to hydrostatically balance the sail alone, the amount of ice underwater tends to be underestimated, because the hydrostatic effect of the surrounding level ice has been ignored. This is illustrated in Fig. 4.2, which compares keel cross-sectional areas calculated from the dimensions of snow sails assuming hydrostatic equilibrium, with keel areas obtained by summing the amount of ice below sea level across the extent of each keel. The majority of the calculated keel areas are less than the measured keel areas. Therefore, in order to estimate the volume of keels from the height and areal coverage of snow sails, we need a ratio between snow sail and keel volume which is scaled for unit surface area covered by sails.

4.4.2 Evidence for snow sail/keel dissociation

Previous studies have all assumed that the presence of a snow sail implied the presence of an ice sail and a keel (Fig. 4.3a) (e.g., Kirillov 1957, Worby & Allison 1999). However, drill data from the Ross Sea show evidence that not every ice sail is associated with a keel (Fig. 4.3b), not every keel is associated with an ice sail (Fig. 4.3c), and not every snow sail is associated with an ice sail (Figs. 4.3d and e). Keels without ice sails have also been reproduced in laboratory experiments and experiment results showed that these keels tended to form from ice sheets with heterogeneous internal structure (Tuhkuri and Lensu, in press). On the other hand, observers on ships may not be able to distinguish between snowdrift and deformation features, and hence, some of the observed sails may be formed from wind redistribution and not related to the ridging process which produces keels. Therefore, in order to estimate keel cross-sectional area from dimensions of the observed sail, we need to account for the relationship between the presence of a snow sail and the presence of a keel.

4.5 Data

Two different types of data were used in this study. The first type of data was obtained by drilling on Antarctic first year sea ice floes at 1 m intervals along transects 50 to 150 m long. At each drill hole, snow thickness, z_s, ice thickness, z_i, and freeboard, z_f, were measured. The mean values for each variable were used to derive values for the parameters in the formulae for estimating equivalent thickness, i.e., the probability of snow sail/keel dissociation and the ratio between snow sail and keel cross-sectional areas per unit snow sail width. The data were obtained on three cruises in the Ross Sea in autumn and winter 1995 (cruises NBP 95-3 and NBP 95-5a) and autumn 1998 (cruise NBP 98-3) (Fig. 4.4).

Snow sails and keels were identified from the snow and ice bottom surfaces respectively, following the identification scheme presented in Tin and Jeffries (2001). Since we are interested in snow sails as features which can be observed from ships, the identification scheme identifies snow sails as features which protrude significantly (≥0.3m) above the surrounding level snow surface. Keels are identified as features which are significantly more voluminous than (≥2.25 times thicker than) the surrounding level ice.

The second type of data was obtained from ship observations following the ASPeCt protocol on the same cruises. The formulae for estimating equivalent thickness were applied to observations made along the southbound legs of each cruise, which closely followed longitude 180° (Fig. 4.4). Limiting the study to data obtained along 180° simplifies the comparison of the results obtained with each of the formulae. The data were edited to exclude observations within 11.1 km (6 nautical miles) of the previous observations to prevent biasing in areas of heavy ice where the ship's speed was reduced (Worby & Allison 1999).

4.6 New formulae

The Original formula is modified in two steps. In the r-star formula, the parameter of r' is replaced by r^* which is the ratio between the cross-sectional area of the snow sail and the cross-sectional area of the keel per unit snow sail width. The r-star formula is then modified to include the probability that a snow sail is associated with a keel underwater, and the probability that keels may be found under level surfaces to form the Probability formula.

4.6.1 The r-star formula

Assuming the same geometrical model as the Original formula (Fig. 4.1), the r-star formula is

$$z_r = 0.5RS(r^*+1) + z_u \qquad [4.2]$$

where

$$r^* = \frac{\sum_{i=1}^{m} A_{k_i}}{\sum_{i=1}^{m} A_{s_i}} \qquad [4.3]$$

and A_k is the cross-sectional area of a manifest keel (a keel associated with a snow sail); A_s is the cross-sectional area of the associated snow sail calculated from its width and height, assuming a triangular cross-section as in the geometrical model of Fig. 4.1; and m is the number of manifest keels.

4.6.2 The Probability formula

Building on the r-star formula, we develop the Probability formula to include the effects of snow sail/keel dissociation. The equivalent thickness, z_r, comprises of the equivalent

thickness of observed features, Oz_r, and the equivalent thickness of inferred features, Iz_r.

$$z_r = Oz_r + Iz_r \qquad [4.4]$$

Observed features are those that can be seen from a ship, i.e., the snow sail and the base layer.

$$Oz_r = 0.5RS + z_u \qquad [4.5]$$

Inferred features are those that can only be inferred from the observations. The equivalent thickness of inferred features comprises of the equivalent thickness of manifest keels, Mz_r, and the equivalent thickness of hidden keels (keels not associated with snow sails), Hz_r.

$$Iz_r = Mz_r + Hz_r \qquad [4.6]$$

Each manifest keel has an area r^* times that of the snow sail above. However, not every snow sail is associated with a keel. Therefore, we factor in p_R, the probability that a snow sail is associated with a keel, to obtain a mean estimate of the equivalent thickness of a manifest keel.

$$Mz_r = p_R r^* 0.5RS \qquad [4.7]$$

The probability p_R is derived from drill data as

$$p_R = \frac{\sum_{i=1}^{n_1} W_{\bar{s}_i}}{\sum_{i=1}^{n_2} W_{s_i}} \qquad [4.8]$$

where $W_{\bar{s}}$ is the entire width of a snow sail which fully or partially overlaps with a keel; W_s is the width of a snow sail; n_1 is the number of snow sails which fully or partially overlaps with a keel; and n_2 is the number of snow sails. The probability p_R is a function of the characteristics and conditions of the ice floes, such as their strength, the atmospheric and oceanic forcing acting on them, and the aeolian distribution of snow on their surfaces.

The mean estimate of the equivalent thickness of a hidden keel can be obtained by multiplying the average thickness of such a keel, K_L, by the probability that a keel is below a level snow surface, p_L.

$$Hz_r = X[p_L(1-R)K_L] \qquad [4.9]$$

where X = *1* for $R > 0.05$; X = *0* for $R \leq 0.05$

The average thickness of a hidden keel, K_L, is derived from the drill data as

$$K_L = \frac{\sum_{i=1}^{q} A_{k'_i}}{\sum_{i=1}^{q} W_{k'_i}} \qquad [4.10]$$

where $A_{k'}$ is the keel area of a hidden keel, $W_{k'}$ is the width of the keel and q is the number of hidden keels.

The probability of p_L is defined as

$$p_L = \frac{\sum_{i=1}^{t_1} W_{\bar{u}'_i}}{\sum_{i=1}^{t_2} W_{u'_i}} \qquad [4.11]$$

where $W_{\bar{u}'}$ is the entire width of a contiguous section of the snow surface which is not part of any snow sail and does not overlap with any manifest keel but which overlaps with hidden keels; $W_{u'}$ is the width of a contiguous section of the surface which is not part of any snow sail and does not overlap with any manifest keel; t_1 is the number of contiguous sections of the snow surface which is not part of any snow sail and does not overlap with any manifest keel but which overlaps fully or partially with hidden keels; and t_2 is the number of contiguous sections of the surface which is not part of any snow sail and does not overlap with any manifest keel. The probability p_L is a function of the homogeneity of the ice floes and the atmospheric and oceanic forcing acting on them. It is the probability that unit area of level surface overlies part of a hidden keel, and contains information on the number of hidden keels per unit distance, i.e., the frequency of hidden keels. Only long transects of concurrent top and bottom surface profiling can provide accurate information on the frequency of snow sails and keels on a large scale. This type of data is not available in our study, so we derive an approximate value of p_L from the short transects of drill data and use it to demonstrate its application in the Probability formula.

The probability that there is a keel underneath a level surface is related to the amount of deformation in the region, which is most closely parameterized in terms of the areal coverage of sails, R. The relationship between p_L and R cannot be derived from the existing data. Therefore, in order to avoid overestimating the equivalent thickness in young ice regions, p_L is only considered when R is greater than 5%, as a first approximation of the relationship between p_L and R.

The resultant Probability formula is thus

$$z_r = 0.5RS + z_u + p_R r^* 0.5RS + X[p_L(1-R)K_L] \qquad [4.12]$$

where X = *1* for $R > 0.05$; X = *0* for $R \leq 0.05$

4.7 Statistical methods

4.7.1 Propagation of variances

In order to assess the equivalence of estimates of equivalent thickness from different formulae, we need to quantify variances of the estimates linked to measurement and observation errors. For a function V where,

$$V = V(x,y) \qquad [4.13]$$

the variance in V, s_v^2, is defined as a function of the independent and uncorrelated errors in x, s_x, and y, s_y, as:

$$s_v^2 = \left(\frac{dV}{dx}s_x\right)^2 + \left(\frac{dV}{dy}s_y\right)^2 \qquad [4.14]$$

(Beers 1962, Neuilly 1999). Variances in estimates of equivalent thickness arose from variances in the measurements of z_s, z_f and z_i on the drill transects, and from variances in the visual estimates of R, S, z_u, and ice concentration, c, from the ship observations. Table 4.1 lists the mean variances for observations and drill measurements, estimated from data bin sizes and accuracy of measurement instruments respectively. The variances of r', r^* and K_L were estimated from the propagation of measurement and observation variances following Eqn. 4.8b. The variance of the probabilities p_L and p_R were calculated from

$$s_p^2 = \frac{p(1-n)}{n} \qquad [4.15]$$

where s_p^2 is the variance of the probability p and n is the number of samples (Lapin 1983). These variances were propagated through the Original, r-star and Probability formulae following Eqn. 4.14 to obtain the variances of the estimates of equivalent thickness for the different formulae.

4.7.2 Statistical tests

Two-sample Student's t-tests were used to quantify equivalence of the estimates of equivalent thickness within the variance linked to measurement and observation variances (Moore & McCabe 1993). A minimum sample size of five is required to ensure the robustness of the two-sample t-test; therefore observations were analyzed in groups of two degrees of latitude, which contained six to sixteen observations. For each group, estimates from the r-star and Probability formulae were tested against estimates from the Original formula. F-tests were first used to assess the equivalence of variances. In the cases where variances were statistically different, the Welch statistic was calculated to modify the degrees of freedom of the group before the t-test was performed (Swan & Sandilands 1995).

4.8 Results

4.8.1 Derivation of parameters

Drill data from NBP 95-3, NBP 98-3 and NBP 95-5a amounted to 8 926 drill holes along 101 transects. A total of 24 keels were completely sampled by the transects, and 5 of them overlapped with snow sails. The derived values of r^*, p_R, p_L, K_L and r' are listed in Table 4.2.

4.8.2 Comparing equivalent ice thickness

Fig. 4.5 plots estimates of equivalent thickness by each formula for each two degree latitude band. The estimates from the Original formula are consistently the lowest in value and variance, while those from the r-star formula are always the highest. T-tests did not show any statistical evidence to suggest that mean Probability estimates averaged over two degrees of latitude were different from mean Original estimates. On the other hand, r-star estimates are different from the Original estimates at the 95% significance level for all two degree latitude bands, except the northernmost band on each of the three cruises.

The differences between the three formulae arise from the estimate of the cross sectional area of the keel. In the Original formula, the mean keel area is calculated as r', which is 3.58 times that of the snow sail area (Table 4.2). In the r-star formula, r' is replaced by r^* and the mean keel area is then nearly 8 times that of the snow sail area, which was more than twice that of the Original formula. In the Probability formula, the mean keel area is calculated as r^* times that of the snow sail area but the probability that a snow sail is associated with a keel, p_R, is factored in. This lowers the estimate of the mean keel area significantly to 3.93 times that of the snow sail area, which is close to the r' value used in the Original formula. Incorporating the low probability that keels may be found under level surfaces, p_L, raises the estimates of equivalent thickness only slightly, since p_L is small (0.07) and less than 15% of p_R. As a result, the estimates from the Original formula are very similar to those from the Probability formula.

4.9 Discussion and Conclusions

4.9.1 Use of formulae

Of the three formulae, the Probability formula provides the most accurate physical model for the estimate of equivalent thickness, and should be used to derive estimates of

equivalent thickness where there are sufficient data to derive values for the parameters r^*, K_L, p_L and p_R. However, data on pressure ridges in the Southern Ocean data are sparse and in regions where there are insufficient data to derive values for the parameters, the r-star formula, with its realistic ratio of snow sail and keel area, should be used. Nevertheless, the user must bear in mind that the results from the r-star formula tend to be overestimates of equivalent thickness, as illustrated in Fig. 4.5, since p_L and p_R have not been taken into account. As reflected by the numerically similar estimates of equivalent thickness from the Original and Probability formulae, it is possible that, under certain conditions, the more simple Original formula can be used as a proxy for the Probability formula where data on pressure ridges are not available. However its validity for conditions other than early autumn and late winter in the Ross Sea needs to be tested.

4.9.2 Biases introduced by sampling process and identification scheme

The parameters r^*, p_L, p_R and K_L are essential inputs to the Probability formula but their values are highly influenced by the methods of data collection. Here, we try to quantify the biases that the sampling process of linear drill transects and the identification of sails and keels from drill profiles may introduce into the derived values of these parameters.

The process of sampling three-dimensional pressure ridges with linear transects may be a source of bias. A linear transect may not simultaneously sample a sail and a keel which are longitudinally separated, and might lead to false identification of dissociated sails and keels, and biases in the derived values of p_L and p_R. Another source of bias is the angle at which a linear transect bisects a ridge. An oblique bisecting angle cuts through more of the ridge, and hence results in a larger cross-sectional area for a keel than that resulting from a perpendicular bisecting angle. This can lead to biases in the values of r^* and K_L. Unfortunately, these effects on r^*, p_L, p_R and K_L cannot be quantified from existing data,

and additional data from three-dimensional studies of pressure ridges and of large areas of ridged ice are needed to fully address this issue.

The scheme used to identify sails and keels from drill profiles may also be a source of bias. As it identifies sails and keels as features which have profiles that depart significantly from the surrounding level ice, the scheme may miss sails and keels which are smaller than the specified minimum height (for a sail) and thickness (for a keel), or which are surrounded by little level ice. We believe that the effect of missing small sails and keels on the estimate of equivalent thickness is minimal, since sails less than 0.3 m above the surrounding level snow surface are unlikely to be observed from the ship and recorded in the ASPeCt data, and keels less than 2.25 times as thick as the surrounding level ice contribute little to total ice volume. In the case where little level ice is sampled by a drill transect which is 50 m to 150 m in length, we estimate that approximately 10% of the total number of keels have been missed by the identification scheme.

The parameter p_L represents information on the frequency of hidden keels which can only be accurately obtained from long transects of concurrent top and bottom surface profiling. It is possible that the value of p_L used in this study differs from the true value, since it has been derived from short drill transects. Equivalent thickness as estimated from the Probability formula is balanced between p_L, which prevents underestimation of the amount of ice underneath level surfaces, and p_R, which prevents the overestimation of the amount of ice underneath sails. How would a realistic value of p_L, obtained from long transects of concurrent top and bottom surface profiling, affect the relative effects of p_L and p_R on estimates of equivalent thickness? In order to address this question we make use of an additional 103 drill profiles obtained on 5 other cruises in the Ross, Amundsen, Bellingshausen and Weddell Seas to provide a dataset which spans 204 profiles and nearly 19 km. Approximately 20 snow sails and keels were identified in this dataset. This is equivalent to snow sail and keel frequencies of the order of 10^{-3} m^{-1}, which is of the same order of magnitude as the average snow sail frequency measured in the Ross Sea by

an airborne laser profilometer along transects of approximately 100 km in length (2.5 snow sails km^{-1}, Weeks *et al.* 1989). Therefore, we expect the effect of p_L on equivalent thickness to remain significantly weaker than that of p_R, even with the application of a realistic value of p_L.

4.9.3 Variance of equivalent ice thickness

The mean variance of estimates of equivalent thickness from individual observations is 18%. When observations are summarized for two degree latitude bands, the variance for each band drops to a mean of 6.3% or 3 cm. The variance of the estimate of equivalent thickness decreases from averaging over increasing number of samples, i.e., with decreasing spatial resolution. Although the variance of individual observations is high, equivalent thickness estimates at one or two degree resolution have reduced variance and can be used for validating sea ice models. However, in order to detect changes in equivalent thickness, data from multiple cruises are needed to first establish the baseline equivalent thickness with some confidence and then to accurately quantify any changes.

4.9.4 Contribution of ridging to total ice mass

From estimates of equivalent thickness, we can estimate the percentage underestimation, U, of total ice mass if keels are ignored and the average thickness is approximated by only the thickness of the surrounding level ice,

$$U = \frac{Z_r - Z_u}{Z_u} \quad [4.16]$$

where upper case letters represent the summation of z_r and z_u along the cruise track. This is also a measure of the contribution of ridge snow sails and keels to the total ice mass. If

every snow sail represents a keel underwater and no keels are underneath level surfaces, then the percentage underestimation by level approximation is 46%, as derived from the r-star formula, for the southbound leg of NBP 95-3 which was just over 1 000 km long (Fig. 4.6a). By incorporating the probabilities of snow sail/keel dissociation into the r-star formula, the percentage underestimation by level approximation drops to 26% in the Probability formula, similar to the 24% derived from the Original formula (Fig. 4.6a). The percentage underestimation by level approximation is similar along the southbound leg of NBP 98-3 which was 1 200 km long (Fig. 4.6c). On the southbound leg of NBP 95-5a, which is close to 700 km in length, the percentage underestimation by level approximation ranges from about 40% according to the Original and Probability formulae to 77% according to the r-star formula. These results show that ridging is an important process in determining the ice thickness distribution in the Ross Sea, and although pressure ridges are small features, they constitute a significant fraction of the total ice mass in the area in the Ross Sea during the autumn / winter period.

4.10 Acknowledgments

This study was funded by National Science Foundation grant OPP-9614844 and a Global Change Student Research Grant from the Center for Global Change and Arctic System Research, University of Alaska Fairbanks made TT's visit to Helsinki University of Technology possible. TT would like to thank Tony Worby, Dan Hawkins, Ron Berry, Paul Layer and Yanling Yu for helpful discussions and statistical advice. The authors would like to thank Terry Tucker, Stan Jacobs and an anonymous reviewer for comments on earlier drafts.

4.11 Figures

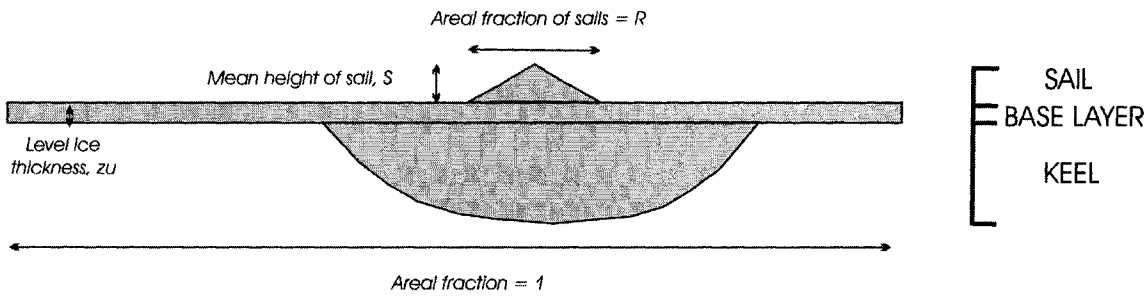

Figure 4.1 Geometrical model of pressure ridge used for deriving equivalent thickness.

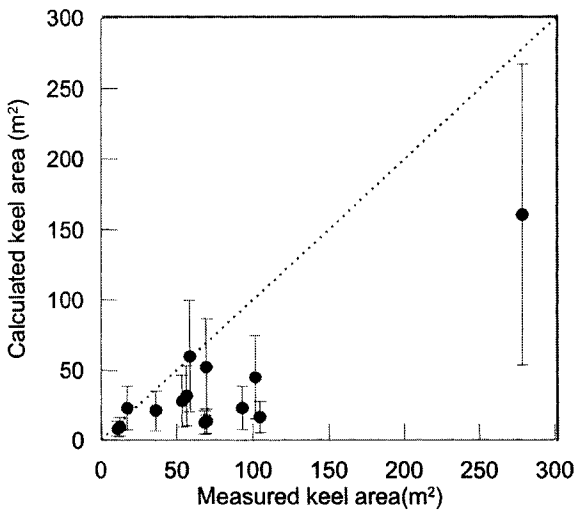

Figure 4.2 Measured and calculated keel cross-sectional areas. Calculations are made based on the assumption of hydrostatic equilibrium. Data represent 13 pressure ridges with both sails and keels in the Ross, Amundsen, Bellingshausen and Weddell Seas. Error bars show the spread of calculated keel areas, assuming 20% uncertainty in densities of snow and slush, and ice porosity, and 5% uncertainty in densities of ice and water. The dotted line represents 1:1 correspondence between the calculated and measured values.

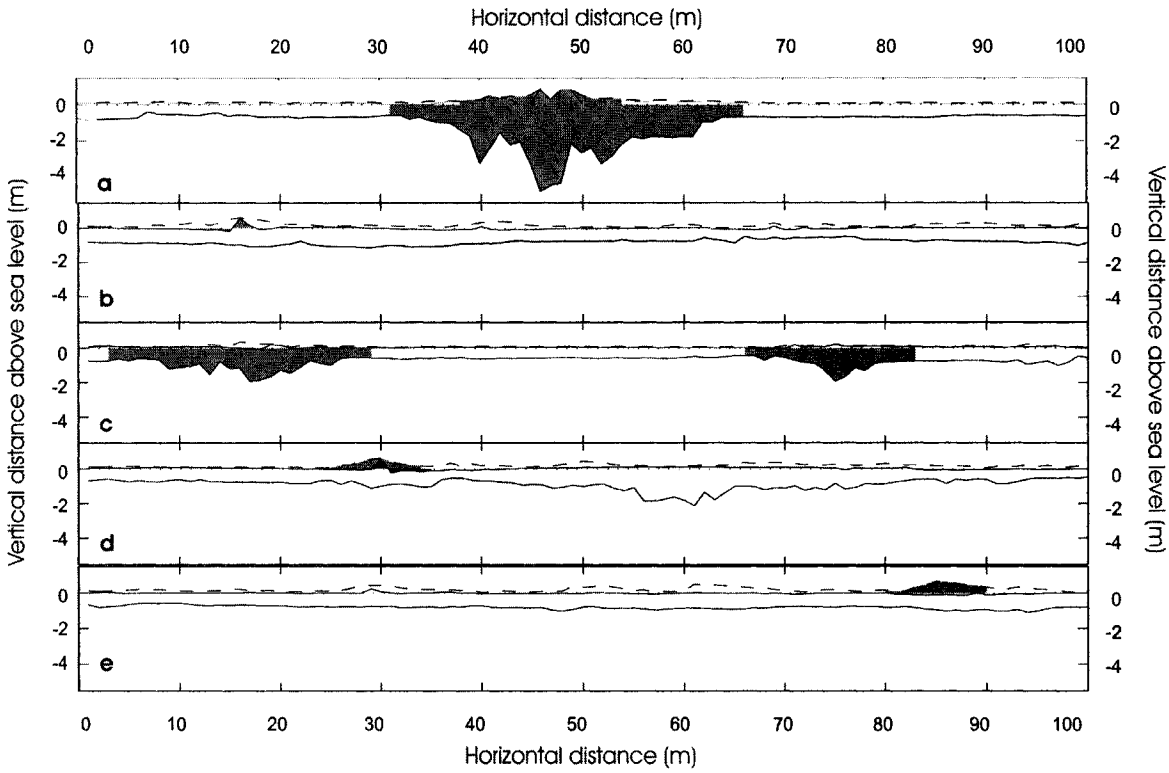

Figure 4.3 Examples of sail/keel dissociation and association. **a.** associated ice sail, snow sail and keel, **b.** an ice sail not associated with a keel, **c.** keels not associated with ice sails, **d.** a snow sail associated with an ice sail, **e.** a snow sail not associated with an ice sail. The dashed line represents the snow surface. The two solid lines represent the top and bottom surfaces of the ice.

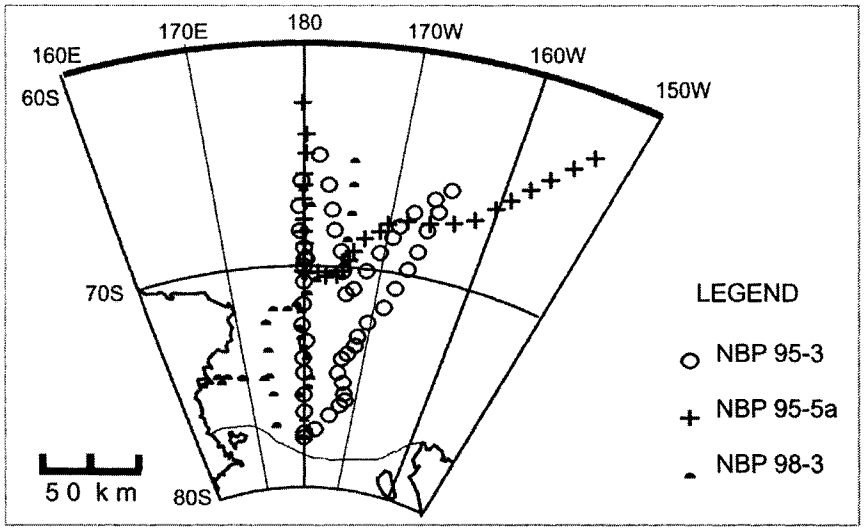

Figure 4.4 Cruise tracks of NBP 95-3, NBP 95-5a and NBP 98-3.

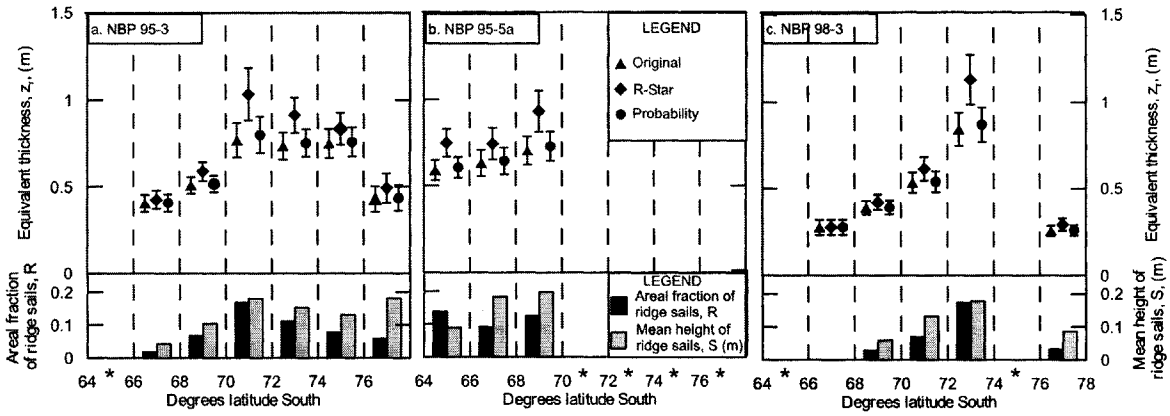

Figure 4.5 Estimates of equivalent thickness from different formulae. Equivalent thickness, z_r, estimated from the Original, r-star and Probability formulae, together with mean observed areal fraction of ridge sails, R, and mean observed height of ridge sails, S, re averaged over 2 degree latitude band along the southbound leg of three cruises are presented and Error bars around z_r indicate the range enclosed by mean +/- 2 times error of the estimate. * indicates no observations in latitude band. **a.** Cruise NBP 95-3, **b.** Cruise NBP 95-5a, **c.** Cruise NBP 98-3.

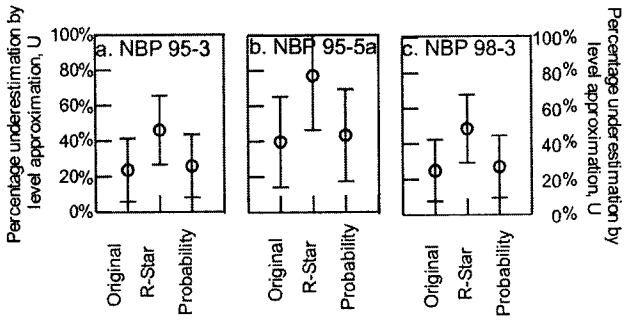

Figure 4.6 Percentage underestimation of total ice mass. Percentage underestimation of total ice mass if keels are ignored and average thickness is approximated by the thickness of the surrounding level ice only.

4.12 Tables

Table 4.1 Mean estimated variances of ship observations and drill measurements.

	Quantity	Mean estimated variance
Observed quantities	Areal coverage of snow sails, R	15 % of observation
	Mean height of snow sails, S	15 % of observation
	Level ice thickness, z_u	15 % of observation
	Snow thickness, z_s	15 % of observation
	Concentration or areal coverage of ice category, C	10 % of observation
Measured quantities	Ice thickness, z_i	0.005 m
	Freeboard, z_f	0.005 m
	Snow thickness, z_s	0.005 m

Table 4.2 Mean values and variances of derived parameters. Mean values and variances of derived parameters used in formulae for estimating equivalent thickness. Drill holes are 1 m apart.

Derived parameters	Mean value	Variance	No. of observations
r^*	7.93	0.068	From 5 manifest keels: 210 drill holes from keels and 75 drill holes from sails
p_R	0.48	0.033	205 drill holes from 16 sails
p_L	0.07	0.003	8 676 drill holes
K_L	0.35 m	0.007 m	481 drill holes from 19 hidden keels
r'	3.58	0.00004	850 drill holes

4.13 References

Beers, Y. 1957. *Introduction to the theory of error.* Addison-Wesley.

Bowen, R.G. and Topham, D.R. 1996. Study of the morphology of a discontinuous section of a first year arctic pressure ridge. *Cold Regions Science and Technology*, 24(1), 83-100.

Burden, R.P. and Timco, G.W. 1995. A catalogue of sea ice ridges. *National Research Council of Canada Report*, TR-1995-27, Ottawa, Ontario.

Comiso, J.C., Wadhams, P., Krabill, W.B., Swift, R.N., Crawford, J.P. & Tucker, W.B. III. 1991. Top/bottom multisensor remote sensing of Arctic sea ice. *Journal of Geophysical Research*, 96 (C2), 2 693-2 709.

Dierking, W. 1995. Laser profiling of the ice surface topography during the Winter Weddell Gyre Study 1992. *Journal of Geophysical Research*, 100 (C4), 4 807-4 820.

Hibler, W.D. III, Mock, S.J. & Tucker, W.B. III. 1974. Classification and variation of sea ice ridging in the western Arctic Basin. *Journal of Geophysical Research*, 79 (18), 2 735-2 743.

Kankaanpää, P. 1997. Distribution, morphology and structure of sea ice pressure ridges in the Baltic Sea. *Fennia*, 175(2), 139-240.

Kirillov, A.A. 1957. Correction for hummocking in the calculation of ice volume. [Uchet torosistosti pri opredelenii ob"ema l'da] *Problemy Arktiki*, No. 2, 53-58.

Kovacs, A. 1972. On pressured sea ice. *In* Proceedings of International Conference on Sea Ice, May 10-13, 1971, Reykjavik, Iceland. 276-295.

Leppäranta, M. 1981. Statistical features of sea ice ridging in the Gulf of Bothnia. *Research report no. 32, Winter Navigation Research Board.* Helsinki Government Printing Office. 46pp.

Massom, R.A., Drinkwater, M.R. & Haas, C. 1997. Winter snow cover on sea ice in the Weddell Sea. *Journal of Geophysical Research,* 102 (C1), 1 101-1 117;

Moore, D.S. & McCabe, G.P. 1993. *Introduction to the practice of statistics.* Freeman.

Neuilly, M. 1999. *Modelling and estimation of measurement errors.* Lavoisier.

Swan, A.R.H, & Sandilands, M. 1995. *Introduction to geological data analysis.* Blackwell Science.

Tin, T. & Jeffries, M.O. 2001. Quantitative identification of Antarctic first year pressure ridges and preliminary results on ridge morphology. *In* Proceedings of 16th International Conference on Port and Ocean Engineering under Arctic Conditions. POAC '01, August 12-17, 2001, Ottawa, Canada. Vol. 3, 1,455-1,464.

Tuhkuri, J. & Lensu, M. in press. Laboratory tests on ridging and rafting of ice sheets. *Journal of Geophysical Research.*

Wadhams, P., Tucker, W.B. III, Krabill, W.B., Swift, R.N., Comiso, J.C. & Davis, N.R. 1992. Relationship between sea ice freeboard and draft in the Arctic Basin, and implications for ice thickness monitoring. *Journal of Geophysical Research,* 97 (C12), 20

325-20 334.

Weeks, W. F., Govoni, J. & Ackley, S. F. 1989. Sea-ice ridging in the Ross Sea, Antarctica, as compared with sites in the Arctic *Journal of Geophysical Research*, 94 (C4), 4 984-4 988.

Weeks, W.F., Kovacs, A. & Hibler, W.D. III 1978. Pressure ridge characteristics in the Arctic coastal environment. *In* Proceedings of 1st International Conference on Port and Ocean Engineering under Arctic Conditions. POAC '71, August 23-30, 1971, Trondheim, Norway. Vol. 1, 152-183.

Worby, A.P. & Ackley, S.F. 2000. Antarctic research yields circumpolar sea ice thickness data. *Eos Transactions, American Geophysical Union*, 81(17), 184-185.

Worby, A.P. & Allison, I. 1999. A technique for making ship-based observations of Antarctic sea ice thickness and characteristics. Part I Observational technique and results. *Antarctic CRC Research Report*, No. 25.

Worby, A.P. 1999. Observing Antarctic sea ice: A practical guide for conducting sea ice observations from vessels operating in the Antarctic pack ice. *A CD-ROM produced for the Antarctic Sea ice Processes and Climate (ASPeCt) program of the Scientific Committee on Antarctic Research (SCAR) Global Change and the Antarctic Program (GLOCHANT) program*. Hobart, Australia.

Chapter 5

Numerical simulation and observation of the dynamics and thermodynamics of the Ross Sea ice pack*

5.1 Abstract

In 1998 and 1999, data on sea ice thickness, drift and ridging characteristics were collected in the Ross Sea, Antarctica. In the central Ross Sea in the autumn, ice thickness reached a maximum of 0.6 m at 74°S and it decreased both northward and southward. A similar pattern in the ice thickness distribution was found in the northeast Ross Sea in the summer but ice was generally thicker than in the winter, due to a combination of greater areal coverage of ridge sails, higher sail heights and higher level ice thickness. In order to understand the observed ice thickness distribution we used a regional two thickness level sea ice-mixed layer-pycnocline model to initiate backward trajectories at the time and location of field observations and examined the dynamic and thermodynamic processes which determine ice thickness along these trajectories. In agreement with previously published ice core and oceanographic data, we found that all four ice thickening processes – thermodynamic and dynamic thickening, snow ice formation and melting –contributed significantly to the mass of the summer ice field in the northeast Ross Sea. In the case of first year ice in the central Ross Sea, both ice core data and model results indicated that thermodynamic thickening was the dominant process that determined ice thickness, although dynamic thickening also played a significant role. Ice cores also indicated that snow ice contributed a significant fraction to the total mass of first year ice in the central Ross Sea. This was not reproduced by model results.

---

* Tin, T., Timmermann, R. and M.O. Jeffries. to be submitted to Journal of Glaciology.

5.2 Introduction

Due to the vastness and remoteness of the Ross Sea ice cover, it is difficult to examine its time-varying characteristics in detail and over a broad scale simultaneously. Satellite remote sensing data allow changes in ice extent to be examined over a large area and over long periods of time (e.g., Zwally et al., 1985; Sturman and Anderson, 1986; Jacobs and Comiso, 1989). Sampling of ice floes from icebreakers can provide snapshots of ice characteristics localized in time and space (e.g., Jeffries and Weeks, 1992; Jeffries and Adolphs, 1997). While the processes involved in the formation of the sampled ice can be inferred from the crystal structure of the ice, the location and time of when and where those processes occurred cannot easily be determined. Local ice sampling can only represent the ice conditions at the time and location of sampling, along with characteristics acquired along its drift path. Numerical models provide well-controlled laboratories to examine the cumulative processes involved in the formation of observed phenomena, especially in terms of ice processes (e.g., Flato and Hibler, 1995; Fichefet and Goose, 1999; Van Woert, 1999). However, the lack of compatible field data to validate numerical output often limits the interpretation of simulation results.

In this study, we combine the power of a numerical model to provide high spatial and temporal resolution information with detailed field observations and measurements of ice thickness to gain some insights into the dynamic and thermodynamic development of the Ross Sea ice pack.

Our field observations were made in the Ross Sea along 180° longitude in May 1998 and along 165°W and 150°W in January 1999 (Fig. 5.1), aboard the R/V Nathaniel B. Palmer during cruises NBP 98-3 and NBP 99-1. These were semi-quantitative shipboard observations recorded following the protocol developed by the Antarctic Sea Ice Processes and Climate (ASPeCt) program. ASPeCt is part of the Scientific Committee on Antarctic Research (SCAR) Global Change and the Antarctic Program (GLOCHANT). One of its goals was to define the broad scale, time-varying characteristics of Antarctic sea ice. To this end, ASPeCt has been promoting summer,

fall, winter, spring measurements of key characteristics of the Antarctic sea ice cover along transects perpendicular to the Antarctic coast and spaced at intervals of about 15-30° of longitude. The observations recorded during our cruises contribute to the ASPeCt data archive.

We use a well-established regional sea ice-mixed layer-pycnocline model (Lemke et al., 1990) to simulate the observed ice pack and to derive the trajectories of the ice observed during NBP 98-3 and NBP 99-1 prior to the time of observation. Trajectories are initiated at the location and time of observation and they are traced backward in time. We then focus on the dynamic and thermodynamic processes which determine ice thickness along these trajectories and examine the relative importance of different processes and their variations in time and space.

In the next section, we present a brief description of various key features of the Ross Sea ice cover. This is followed by a description of the methodology of ASPeCt observations and a presentation of sea ice thickness and ridging characteristics recorded during NBP 98-3 and NBP 99-1 using the ASPeCt observation protocol. Sea ice drift trajectories recorded by buoys deployed on the ice during the cruises are also presented. The various components of the numerical model, some of its features and the choice of model parameter values are summarized and the ability of the model to reproduce observed ice extent, drift and thickness are also discussed. We then describe the methodology used in analyzing backward trajectories, particularly in the light of the findings of the previous section, and present the results from the examination of the different ice thickening processes along the backward trajectories. The relative importance of these processes, their variations in time and space and possible errors in our analysis are then discussed.

The goal of this study is to use a well-established numerical model as a tool to gain a wider spatial and temporal perspective on the observations made during the cruises. While all attempts have been made to optimize the model used in this study in order to produce the most realistic drift results, expansion and development of the model are

beyond the scope of this study.

5.3 The Ross Sea ice cover

5.3.1 Seasonal evolution of sea ice extent

The Ross Sea ice extent reaches a maximum in September (Fig. 5.2b) (Zwally et al., 1985). Melting begins in October as the central and southern Ross Sea melts northward from the Ross Ice Shelf and the northern ice edge moves southward until the two eventually meet (Sturman and Anderson, 1986). By February, the ice extent reaches its minimum, with a residual ice field northeast of the continental shelf (Jacobs and Comiso, 1989) and some perennial ice north of Oates and Pennell Coasts and at scattered locations along the coast of Victoria Land (Jeffries and Weeks, 1992) (Figs. 5.2e and 1). Summer ice extent varies from year-to-year with the residual ice field being completely absent in some years or shifted in location in other years (Jacobs and Comiso, 1989). This is in contrast with the winter ice extent which varies little between years regardless of variability in atmospheric and oceanic forcing (Jacobs and Comiso, 1989). As the season continues, ice cover expands westward, southward and northward of the eastern continental shelf until, at maximum ice extent in September, there is a continuous ice cover from the coast to as far north as 62°S (Fig. 5.2b).

5.3.2 Variability of thickness and ice concentration within ice pack

During the summer, in the eastern Ross Sea a thick snow layer lies on top of the sea ice. This snow cover is commonly between 1-2 m thick and can occasionally reach 3-4 m (Jeffries et al., 1994). There is extensive melting and flooding in the snow pack, but bare ice and melt ponds have not been observed on the ice surface (Morris and Jeffries, 2001). Beneath the snow cover is a layer of snow ice that forms from the freezing of slush, at the flooded snow/ice interface. Voids at the bottom of this layer decrease the bond strength of

the top layer of snow and snow ice with the underlying sea ice. The bottom surface of the sea ice is characteristically pitted with holes (Jeffries and Weeks, 1992).

In the Ross Sea between 160°E and 160°W, the winter ice pack distinctly falls into three zones, defined by its distance from the Ross Ice Shelf (Jeffries and Adolphs, 1997). At zero to two hundred km north of the Ross Ice Shelf is the area where the Ross Polynya periodically opens. Here, thin ice dominates and the age of ice increases with distance from the coast. Both dynamics and thermodynamics are important in contributing towards the ice thickness in this zone, as the polynya is maintained by high divergence (or export of ice). Two to six hundred km north of the Ross Ice Shelf is a region of thicker and older ice that has also been thickened both dynamically and thermodynamically. Extensive ridging has been observed in this zone, particularly in the region east of Victoria Land (Weeks et al., 1989). Beyond six hundred km north of the Ross Ice Shelf, the ice cover is made up of young deformed ice with a thin snow cover. Here, the pancake cycle dominates (Wadhams et al., 1987). Discs of new ice form thermodynamically in open water and are rapidly thickened by rafting under wind and wave action. After the pancakes have consolidated, basal congelation ice growth occurs under calm conditions that are more prevalent in the inner ice pack than in the outer ice pack. In the outer ice pack snow ice forms a significant portion of the ice mass due to frequent flooding of the snow cover by wave action or heavy snow load (Jeffries and Adolphs, 1997; Jeffries et al., 2001).

5.3.3 Polynyas and ice drift

The largest polynya in the Ross Sea is the Ross Polynya in the southwestern Ross Sea, immediately north of the Ross Ice Shelf (Sturman and Anderson, 1986). Strong offshore winds, including katabatic surge events move sea ice out of the area (Bromwich et al., 1998), while intrusions of relatively warm water originating from the Antarctic Circumpolar Current retard ice growth (Fichefet and Goosse, 1999; Jacobs and Comiso,

1989). The polynya is most evident during the austral spring with onset occurring around the beginning of November. The exact timing of the onset is dictated by many factors including thickness and integrity of the ice, springtime temperature and wind stress (Arrigo et al., 1998).

Terra Nova Bay Polynya appears quite clearly throughout the winter in the western Ross Sea near 75°S, 164°E. It is maintained by a combination of katabatic winds that advect sea ice eastward and northeastward away from the shore, and the physical barrier of Drygalski Ice Tongue preventing ice from drifting in from the south (Bromwich and Kurtz, 1984; Kurtz and Bromwich, 1983). Near the continental shelf break, there are the Ross Passage (71°S, 172°E) and Pennell Polynyas (75°S, 180°), which are maintained by upwelling of warmer water from the continental slope region (Jacobs and Comiso, 1989).

Sea ice drift in the Ross Sea reflects the large scale atmospheric and oceanic circulation patterns. Ice drift is westward and northward on the continental shelf following the cyclonic Ross Gyre (Moritz, 1988; Wordie, 1912). Off the continental shelf, the ice joins the Antarctic Circumpolar Current and drifts east at increased speeds.

5.4 Ship observations methodology

According to the ASPeCt protocol, a standard set of observations is made hourly by an observer on the ship's bridge. These include the ship's position and total ice concentration, and an estimate of the areal coverage, thickness, floe size, topography (i.e., areal coverage and mean height of ridge sails) and snow cover of the three thickest ice categories within a radius of approximately 1 km of the ship (Worby and Allison, 1999). Equivalent thickness is calculated from the observation data. It is the thickness of a flat slab of ice which has the same volume as contained in all the ridges and level ice combined within the radius of observation. It is estimated from the areal coverage and mean height of sails, and the surrounding level ice thickness using the following formula:

$$z_r = 0.5RS + z_u + p_R r^* 0.5RS + p_L(1-R)K_L \qquad p_L = 0 \text{ for } R \leq 0.05 \qquad [5.1]$$

The equivalent thickness, z_r, is calculated based on the assumption that the observed ice is made up of level ice with a thickness of z_u, triangular ridge sails that have mean heights and areal coverage of S and R, respectively, and possibly ridge keels which contain r^* times as much ice as in the sails (Tin et al., 2003). However, ridge keels are not always associated with a ridge sail (Tin et al., 2003; Tin and Jeffries, in press). Consequently, we take into account, p_R, the probability that a ridge sail on the surface is associated with a ridge keel underwater and, p_L, the probability that a keel is below a level top surface. The probability that there is a keel underneath a level surface, p_L, is assumed to be negligible for areas which are covered by ridge sails that make up <5% of the total surface area, i.e., $R \leq 0.05$. The mean variance of estimates of z_r for an individual ASPeCt observation is 18%, as determined from data from three cruises by Tin et al. (2003).

ASPeCt observations recorded during cruises NBP 98-3 and NBP 99-1 are averaged over 1° latitude intervals to maintain a spatial resolution which is close to that of the sea ice model (Section 5.5.2). The resultant average observations are referred to as summary observations and their locations are illustrated in Fig. 5.1. The mean variance of estimates of z_r for a summary observation is 3%.

Worby and Wu (1998) have shown that climatological ice thickness data constructed from ASPeCt observations that have been collected over a long period of time can be used satisfactorily to validate numerical models. Unfortunately, the number of ASPeCt observations are limited in the Ross Sea. Hence, in this study, we can only use our observations to represent ice conditions at a specific time and location.

5.5 Ross Sea ice conditions in 1998 and 1999

5.5.1 Ice thickness

Data from ASPeCt summary observations located according to Fig. 5.1 are plotted in

Fig. 5.3. Along the 180 longitude in May 1998, mean equivalent thickness was 0.5 m. Equivalent thickness reached a maximum at 74°S as a result of a high areal coverage of large sails (Fig. 5.3a). Equivalent thickness, areal coverage of sails and sail heights all decreased both northward and southward while areal coverage of sails and sail heights reached insignificant levels north of 70°S (Fig. 5.3d). Level ice thickness did not vary linearly with latitude. It remained consistently at 0.3 m north of 71°S and at 0.5 m south of 72°S.

Along 165°W and 150°W in January 1999, mean equivalent thickness was 1.7 and 1.1 m, respectively. Similar to the ice along 180°, equivalent thickness also reached maximum at 74°S along 165°W and 150°W (Figs. 5.3b and c). The equivalent thickness along 165°W and 150°W in January 1999 was significantly larger than along 180° in May 1998, due to a combination of higher level ice thickness, areal coverage of sails and sail height. Along 165°W, the maximum in equivalent thickness was accompanied by maxima in level ice thickness, areal coverage of sails and sail height (Fig. 5.3e). Along 150°W, level ice thickness was at a maximum at 74°S but maxima in sail height and areal coverage of sails were at 73°S and 75°S, respectively (Fig. 5.3f). Maximum equivalent thickness along 165°W and 150°W were 4.4 m and 2.8 m.

5.5.2 Sea ice drift

Fig. 5.4 plots the trajectories of three of the seven buoys deployed during NBP 98-3 and both of the buoys deployed during NBP 99-1 (Jeffries and Kozlenko, 2002). The buoys deployed in May 1998 transmitted for an average of 85 days while the longest data record (shown in Fig. 5.4a) lasted for 216 days. The buoys initially all traveled northwestward around Cape Adare and one buoy continued westward along the Pennell Coast until it joined the Antarctic Circumpolar Current and drifted eastward.

The two buoys deployed in January 1999 transmitted for an average of 310 days. They

were deployed near 137°W and traveled in different directions. The buoy deployed at 70°S, 138°W drifted eastward into the Amundsen Sea while the buoy deployed at 74°S, 136°W initially drifted westward and then turned eastward at 155°W.

5.6 Numerical model: description, sensitivities and parameterization

The model used in this study consists of a two-layer dynamic-thermodynamic sea-ice model (Hibler, 1979) coupled to a one-dimensional mixed layer-pycnocline model (Lemke, 1987). The sea ice is capped by a snow layer (Semtner, 1976) which, when encountering freezing conditions after being flooded by seawater, converts into snow ice (Leppäranta, 1983). Sea ice is represented in each grid cell by a slab of single thickness. The model used in this study is the same as the one used in Fischer and Lemke (1994), Harder and Lemke (1994), Harder and Fischer (1999) and Timmermann et al., (1999). It has been used and updated continuously since 1990 (Lemke et al., 1990) and its features have been examined in a number of studies focused on the Southern Ocean (e.g., Owens and Lemke, 1990; Stössel et al., 1990). The dynamic-thermodynamic sea ice model includes features that have been tested and improved extensively through studies focused on both the Arctic and the Antarctic (e.g., Hibler, 1980; Hibler and Walsh, 1982; Hibler and Ackley, 1983; Hibler, 1984; Walsh et al., 1985). This sea ice-mixed layer-pycnocline model was chosen for the present study because it has been well-established and has shown to represent the Southern Ocean sea ice cover reasonably well. The findings of the studies undertaken in the previous 13 years provide documentation on the sensitivities of the model, allowing the model to be used a tool with relative ease. In the following sections we describe the various components of the model, the model domain and forcing fields, some of the sensitivities of the model which have been revealed in previous studies, and summarize the choice of values of model parameters.

5.6.1 Model description

5.6.1.1 Sea ice model

5.6.1.1.1 Dynamics and dynamic thickening

The dynamic part of the model is based on the sea ice momentum balance:

$$m\frac{D\mathbf{u}}{Dt} = \boldsymbol{\tau}_a + \boldsymbol{\tau}_w + \mathbf{F} + \mathbf{C} + \mathbf{T} \qquad [5.2]$$

where bold type indicates vector quantities, m is the ice mass per area, $m\frac{D\mathbf{u}}{Dt}$ is the temporal change in momentum, $\boldsymbol{\tau}_a$ denotes wind stress, $\boldsymbol{\tau}_w$ is the stress between ice and water , **F** represents the internal force due to ice deformation, **C** is the Coriolis force and **T** is the force due to sea surface tilt. Coriolis force only modifies the drift direction, and the force due to sea surface tilt is generally small. Hence, $\boldsymbol{\tau}_a$, $\boldsymbol{\tau}_w$ and **F** are the important contributions for the simulation of ice drift (Leppäranta and Hibler, 1987; Hibler, 1999; Harder and Fischer, 1999).

Wind and oceanic stresses, $\boldsymbol{\tau}_a$ and $\boldsymbol{\tau}_w$, are determined by

$$\boldsymbol{\tau}_a = \rho_a c_a u_a \mathbf{u}_a \qquad [5.3]$$

$$\boldsymbol{\tau}_w = \rho_w c_w |u_w - u_i| \{(\mathbf{u}_w - \mathbf{u}_i)\cos\theta + \mathbf{k} \times (\mathbf{u}_w - \mathbf{u}_i) \sin\theta\} \qquad [5.4]$$

where subscripts a, w and i represent air, water and ice; and ρ, c, u and θ are density, drag coefficient, velocity and turning angle, respectively (McPhee, 1979). The ratio c_a/c_w determines the relative strength of atmospheric and oceanic forcing on the ice.

Internal forces, **F**, are described in terms of the divergence of a two-dimensional stress tensor, based on the assumption of a viscous-plastic rheology for large scale sea ice behaviour together with an elliptical yield curve (Hibler, 1979; Ip et al., 1991). These internal forces arise from ice deformation and are proportional to the large scale strength

of the ice cover, P. This is parameterized in terms of two ice strength parameters, P^* and C^*, the mean ice thickness over a grid cell, $\bar{h}$, and ice concentration, A (Hibler, 1979). The strength of the ice cover increases linearly with average ice thickness and exponentially with ice concentration

$$P(\bar{h},A) = P^* \bar{h} \exp(-C^*(1-A)) \qquad [5.5]$$

For the purpose of comparing with field data, we are more interested in the actual ice thickness in the ice-covered part of the grid cell, z_i, than the mean ice thickness over a grid cell, $\bar{h}$. The two are related through:

$$z_i = \frac{\bar{h}}{A} \qquad [5.6a]$$

and, using the quotient rule

$$\frac{dz_i}{dt} = \frac{1}{A}\left(\frac{d\bar{h}}{dt} - z_i \frac{dA}{dt}\right) \qquad [5.6b]$$

Ice dynamics may cause an increase in actual ice thickness by increasing the amount of open water and piling up the existing ice volume over a smaller surface area. We define the rate of dynamic thickening, $\left.\frac{dz_i}{dt}\right|_{dynamic}$, as the rate of increase in actual ice thickness due to piling up of existing ice volume over a reduced surface area. During shear deformation of the ice cover, there is no change in the ice volume within the grid cell under shear deformation but the amount of open water in the grid cell is increased (Hibler, 1984). Any subsequent thermodynamic growth of new ice in the newly created

open water is not included in $\left.\frac{dz_i}{dt}\right|_{dynamic}$ but contributes towards the thermodynamic thickening rate instead (see Section 5.6.1.1.2). The rate of dynamic thickening depends on the rate at which open water is increased due to shear deformation, Q_A (Flato and Hibler, 1991; Harder and Lemke, 1994). Considering only the effects of shear deformation, $\psi_s(\dot{\varepsilon}_{ij})$

$$\frac{dA}{dt} = -Q_A = -\psi_s(\dot{\varepsilon}_{ij})\exp[-C^*(1-A)] \qquad [5.7a]$$

and

$$\left.\frac{dz_i}{dt}\right|_{dynamic} = \frac{\bar{h}}{A^2}Q_A \qquad [5.7b]$$

where $$\psi_s(\dot{\varepsilon}_{ij}) = 0.5\{\Delta(\dot{\varepsilon}) - |\dot{\varepsilon}_{11} + \dot{\varepsilon}_{22}|\} \qquad [5.7c]$$

and $$\Delta = \sqrt{(\dot{\varepsilon}_{11}^{\ 2} + \dot{\varepsilon}_{22}^{\ 2})(1+e^{-2}) + 4\dot{\varepsilon}_{12}^{\ 2}e^{-2} + 2\dot{\varepsilon}_{11}^{\ 2}\dot{\varepsilon}_{22}^{\ 2}(1-e^{-2})} \qquad [5.7d]$$

As explained in Hibler (1984), Flato and Hibler (1991) and Harder and Lemke (1994), $\left.\frac{dz_i}{dt}\right|_{dynamic}$ represents ice thickness changes due to all types of ice deformation, and differences between ridging (piling up of broken ice blocks) and rafting (stacking of floes) are not resolved. During ice deformation, snow volume is conserved along with ice volume.

5.6.1.1.2 Thermodynamics: thermodynamic thickening and melting

The thermodynamic part of the model implements Stefan growth by assuming a linear temperature profile across both snow and ice layers. Ice growth rates are determined from conductive, long wave, short wave and oceanic heat fluxes through the ice (Semtner, 1979). The net thermodynamic growth rate over a grid cell, $\left.\frac{d\bar{h}}{dt}\right|_{ther\ \mathrm{mod}\ ynamic}$, is the sum of the growth rate of existing ice in the grid cell, the rate of new ice growth over open water and the rate of melting due to the oceanic heat flux.

$$\left.\frac{d\bar{h}}{dt}\right|_{ther\ \mathrm{mod}\ ynamic} = Af(\bar{h}) + (1-A)f(0) - \frac{Q_0}{\rho_i L} \qquad [5.8]$$

where $f(h)$ is the growth rate of ice thickness h, Q_0 is the oceanic heat flux which is determined from the mixed layer-pycnocline model, ρ_i is density of sea ice and L is the latent heat of fusion. Ice within a grid cell is modeled by a slab of single thickness. Since thermodynamic growth rates vary non-linearly with ice thickness, the growth rate of the slab is calculated from the average of growth rates of seven imaginary ice classes, following Walsh et al. (1985). The thickness of each ice class is spaced at equal intervals between zero and twice the average thickness. As indicated in Eqn. 5.8, since new ice growth over open water is a thermodynamic process, it is included within $\left.\frac{dz_i}{dt}\right|_{ther\ \mathrm{mod}\ ynamic}$, regardless of whether the open water has been created by ice dynamics. We refer to positive values of $\left.\frac{dz_i}{dt}\right|_{ther\ \mathrm{mod}\ ynamic}$ as rates of thermodynamic thickening, T_+, and negative values as rates of melting, T_-:

$$T_+ = \left.\frac{dz_i}{dt}\right|_{ther\,mod\,ynamic} \qquad \left.\frac{dz_i}{dt}\right|_{ther\,mod\,ynamic} \geq 0 \qquad [5.9a]$$

$$T_- = \left.\frac{dz_i}{dt}\right|_{ther\,mod\,ynamic} \qquad \left.\frac{dz_i}{dt}\right|_{ther\,mod\,ynamic} \prec 0 \qquad [5.9b]$$

In the model, when $\left.\frac{dz_i}{dt}\right|_{ther\,mod\,ynamic}$ falls below zero as a result of a net positive heat flux into the ice at the top surface, the snow cover melts first and melting of ice does not begin until the overlying snow has been completely melted. However, if $\left.\frac{dz_i}{dt}\right|_{ther\,mod\,ynamic}$ is negative because of a large oceanic heat flux, ice thickness is reduced.

Ice concentration is also affected by thermodynamic growth, particularly in the case of new ice forming on previously open water. It is assumed that open water does not freeze over instantly, but rather that the fraction of open water decays exponentially at a rate of $\frac{h_0}{f(0)}$, where h_0 is an empirical lead-closing parameter and $f(0)$ is the growth rate for ice of zero thickness. The term $\frac{h_0}{f(0)}$ parameterizes the rate at which the newly formed ice modifies the thickness of the ice slab within the grid cell. The rate of change of ice concentration due to new ice formation on open water, S_A, is

$$S_A = (1 - A)\frac{f(0)}{h_o} \qquad [5.10]$$

5.6.1.1.3 Flooding and snow ice formation

The bottom of the snow layer can be submerged underwater as a result of a heavy snow load. This phenomenon is known as flooding. The submerged snow, also referred to

as slush, freezes to form snow ice, adding to the total ice thickness. The amount of snow ice that is formed is equivalent to the difference between ice draft, h_d and ice thickness, h_i. The rate of snow ice formation over the grid cell is defined as

$$\left.\frac{d\bar{h}}{dt}\right|_{flood} = \frac{h_d - h_i}{\Delta t} \qquad h_i < h_d \qquad [5.14]$$

where $$h_d = \frac{\rho_s}{\rho_w} h_s + \frac{\rho_i}{\rho_w} h_i \qquad [5.15]$$

subscript s represents snow, h is thickness and Δt is the size of the time step of the model (Leppäranta, 1983).

5.6.1.2 Mixed layer-pycnocline model

The oceanic heat flux needed to compute the thermodynamic growth rate of the ice is supplied by the mixed layer-pycnocline model. This model represents the upper ocean as a surface mixed layer underlain by a pycnocline. Temperature and salinity are assumed to be constant in the mixed layer while they are assumed to vary exponentially with depth in the pycnocline. The pycnocline is assumed to be more saline than the mixed layer at all times, warmer than the mixed layer in the winter and colder in the summer. The sea ice model is coupled to the mixed layer through momentum, salt and heat fluxes. Increased salt flux into the mixed layer at cold temperatures, such as during thermodynamic growth of ice, reduces stability of the upper water column. This in turn causes entrainment of warm water from the pycnocline into the mixed layer, deepening the mixed layer. Subsequently, the entrained heat flux reaches the sea ice as an increased oceanic heat flux. A different scenario occurs during the melting of sea ice. Fresh melt water enters the mixed layer and stabilizes the water column, thus inhibiting convection. This leads to

retreat of the mixed layer and a reduction of oceanic heat flux to the sea ice.

5.6.2 Model domain and forcing fields

For our study we use a circumpolar grid with zonal boundaries at 50°S and 82°S with an isotropic resolution of 1.5° zonally and 1.5° cos (ϕ) meridionally for the whole model domain. Daily National Centers for Environmental Prediction (NCEP) / National Center for Atmospheric Research (NCAR) reanalysis output for 10 m wind speed, 2 m air temperature, specific humidity, cloudiness and net precipitation (P-E) are used for atmospheric forcing. A model run for the nine-year integration period between 1985-1994 serves as the spin up. The model is then run for the period of 1995-1999 for analysis. Climatological ocean currents, salinity and temperature are taken from output of the BRIOS-2 coupled sea ice ocean model of the Alfred-Wegener Institute. This model has been used extensively for studies of ice-ocean interactions in the Ross and Weddell Seas (Assmann et al., 2003; Timmermann et al., 2002a; Timmermann et al., 2002b).

5.6.3 Sensitivities of the model as revealed by previous studies

Various versions of the sea ice model and the sea ice-mixed layer-pycnocline model by various authors have been used to examine the sea ice cover in the Southern Ocean (e.g., Harder and Fischer, 1999; Stössel et al., 1990) while the focus has mainly been on the Weddell Sea (e.g., Owens and Lemke, 1990; Lemke et al., 1990). Here, we present a summary of some of the sensitivities of this model, as revealed by these studies.

5.6.3.1 Ice strength parameters, P and C**

The strength of the ice cover determines the degree to which the ice can be compressed. Therefore, it has a stronger effect in regions of convergent or shearing

motion than in divergent regions. The strength of the ice cover is parameterized in terms of two ice strength parameters, P^* and C^*, which have opposite effects on the ice drift and ice thickness (Hibler, 1979). In regions of convergence or shearing, a high ice strength due to a large P^* slows down ice drift (Geiger et al., 1998; Harder and Fischer, 1999) and reduces the ice thickness, while exerting little influence on ice extent (Owens and Lemke, 1990; Stössel et al., 1990). Increasing C^* has the same effect on ice thickness as reducing P^* (Hibler and Walsh, 1982; Owens and Lemke, 1990). Common values for P^* range between 20 000 and 40 000 Nm^{-2} while values for C^* range between 10 and 20.

5.6.3.2 Lead closing parameter, h_0

The lead closing parameter determines how fast leads and open water are frozen over completely. A small h_0 value indicates that leads freeze over slowly, resulting in a thin ice cover, while a large h_0 value results in a thick ice cover (Owens and Lemke, 1990; Stössel et al., 1990). Ice thickness in the summer appears to be less sensitive to the parameterization of h_0 (Fischer and Lemke, 1994). Values of h_0 are typically between 0.25 and 1.0 m (Hibler and Ackley, 1983).

5.6.3.3 Drag coefficients, c_a and c_w

Drag coefficients are used in the computation of the forces imparted on the ice by wind and ocean currents. Sea ice distribution is most sensitive to the patterns of wind stress (Stössel et al., 1990) but measurements (McPhee, 1980) and model simulations (Harder and Fischer, 1999) have shown that the ratio of the drag coefficients is much more important than their absolute values, provided the absolute values are within a reasonable range. A large ratio of c_a/c_w would result in the wind stress having a stronger influence over ice drift velocities than the oceanic stress and would result in fast ice drift velocities (Harder and Fischer, 1999). Values of 0.3 to 0.5 are commonly used for the

ratio of c_a/c_w.

5.6.3.4 Others

Ice extent in the summer is strongly influenced by the parameterization of surface albedo, while its effect is small on the winter ice extent (Fischer and Lemke, 1994). The quality of model results is highly sensitive to the forcing fields (Fischer and Lemke, 1994). Higher air temperatures can reduce ice volume and shift the phase of the seasonal cycle, while changes in precipitation can impart local differences in snow and ice thickness (Stössel et al., 1990).

5.6.4 Choice of values for parameters

As indicated in Section 5.6.3, a judicious choice of values for model parameters is crucial for a realistic simulation of the sea ice cover. Harder and Fischer (1999) conducted a study to find optimal values for the model parameters of P^*, c_a and c_w. In accordance with their findings we found that the parameter values of $c_a = 1.6 \times 10^{-3}$, $c_w = 4.5 \times 10^{-3}$, $P^* = 20\ 0000\ \mathrm{Nm}^{-2}$ and C^*=20 provided the best results for simulating sea ice drift (Fig. 5.4). A value of h_0=0.25 m provided the best result for simulating ice thickness in our study area. These values are comparable to physical estimates made over the Arctic sea ice cover by Hibler (1979) where $c_a = 1.2 \times 10^{-3}$, $c_w = 5.5 \times 10^{-3}$, C^*=20 and h_0=0.5 m. A lower value of 5 000 Nm^{-2} was used in Hibler (1979) when simulating the ice cover's response to 8 day average winds. However, because of the nonlinear wind stress, daily wind fields yield a larger average wind force and hence $P^* = 20\ 0000\ \mathrm{Nm}^{-2}$ is commonly used when simulating the ice cover's response to daily winds (Hibler and Ackley, 1983).

In this study, the albedos of snow and ice under melting conditions are increased to close to or equal to their values under frozen conditions in order to produce a realistic

summer ice extent. This is in accordance with observations and measurements in the Ross Sea in the summer, where the absence of bare ice and melt ponds (Morris and Jeffries, 2001) results in high surface albedo. All-wave albedo measurements range from 0.7 to 0.86, with a possible increase of an average of 1.4% and a maximum of 4% due to clouds (Zhou et al., 2001). Therefore, in the model, the albedos of snow and ice under melting conditions are assumed to be 0.80 and 0.75, while albedos of frozen snow and ice are maintained at 0.85 and 0.75, respectively.

5.7 Comparison between numerical simulations and field observations of the Ross Sea ice conditions in 1998 and 1999

5.7.1 Sea ice extent

Fig. 5.2 shows the simulated sea ice extent superimposed on the ice extent measured by the special sensor microwave imager (SSM/I). There is close agreement between simulated and observed ice extent in the winter months, e.g., May 1998, September 1998 and April 1999. The seasonal cycles of the simulated and observed ice covers are also in agreement, reaching maximum ice extent in September and minimum ice extent in February. In both simulation and observation, melting begins both at the northern ice edge and at the front of the Ross Ice Shelf (Figs. 5.2c). However, melting along Victoria Land is too vigorous in the model (Figs. 5.2d,f).

5.7.2 Sea ice drift

Fig. 5.4 plots the simulated and observed trajectories of the buoys deployed during NBP 98-3 and NBP 99-1. The simulated trajectories are derived from the simulated Eulerian ice velocities by setting the start position and date of the simulated trajectories to those of the observed buoys and then successively calculating the movement of a hypothetical ice particle for each time step. Velocity components are interpolated

bilinearly to the simulated buoy position for each time step. Once the simulated trajectory has significantly drifted away from the observed buoy track, it experiences a different forcing and thus cannot be expected to match the observation accurately (Harder and Fischer, 1999). Therefore, the simulated trajectory is restarted at the location along the observed buoy track after every 60 days.

Fig. 5.4 shows that the model captures the large scale drift pattern reasonably well. Features like the westward-drift along the coastal current, the northward-drift out of the Ross Sea and the eastward-flowing Antarctic Circumpolar Current are reproduced quite realistically. However, in general, the model has difficulty in capturing variations in the north-south direction. Drift velocities are generally slower than observed, and the model drift is overly eastward in the central Ross Sea.

These discrepancies arise from insufficiencies in the forcing fields as well as the physical model. The resolutions of NCEP forcing fields and the model are 2.5° x 2.5° and approximately 1.5° x 1.5°, respectively. Since the drift tracks of each of the buoys deployed on NBP 99-1 span an area of fewer than 5° latitude, a maximum of only two forcing field points in the north-south direction is available for simulating the drift. Local variations on scales smaller than the model grid size or the spatial resolution of the forcing fields tend to be smoothed out and hence are underrepresented in the simulation results. Other studies have shown that NCEP reanalysis underestimates wind speeds by roughly 20% (Smith et al., 2001). As this may be contributing towards the discrepancies between the simulated and observed drift we simulated ice drift with wind speeds, arbitrarily increased by 20%. We found that this resulted in other discrepancies between simulated and observed trajectories and conclude that the underestimation of wind speeds is not the sole cause of the discrepancies between observed and simulated drifts that are illustrated in Fig. 5.4.

5.7.3 Ice thickness

Ice thickness is simulated for the same time and location as the ASPeCt summary observations in Fig. 5.1 and they are plotted with equivalent ice thickness derived from the observation data in Figs. 5.3a, b and c.

In general, the simulated ice thickness distribution agrees reasonably well with the distribution of equivalent thickness as derived from observation data. Along 180° and 150°W, both simulated and observed ice thicknesses drop off toward the northern ice edge and toward the continent to the south (Figs. 5.3a and c). Along 165°W, both decrease from north to south (Fig. 5.3b). The model overestimates ice thickness between 66°S and 71°S along 180° in the autumn ice cover in 1998 (Fig. 5.3a). It underestimates ice thickness in the region south of 72°S along 165°W (Fig. 5.3b) and in the region between 72° and 73°S along 150°W in the summer ice cover in 1999 (Figs. 5.3c).

5.8 Establishing backward trajectories

Using the findings of Section 5.7, we designed our analysis of the backward trajectories to minimize the effects of the limitations of the model. Calculation of backward trajectories was similar to simulating forward trajectories described in Section 5.7.2. The backward trajectory was initiated at the position of an ASPeCt summary observation (Fig. 5.1). In order to match the field observations, backward trajectories were initiated on May 15, 1998 along 180° and on January 15, 1999 along 165°W and 150°W. The hypothesized ice floe was successively moved in the opposite direction of the velocity vector at the present location to arrive at the location of the previous time step. All backward trajectories were stopped on March 15, 1998, which was assumed to be the end of the 97/98 melt season. Simulated buoys were also stopped if they encounter completely open water.

The evolution of snow and ice thicknesses and the four processes which determined ice thickness – thermodynamic thickening, dynamic thickening, snow ice formation and

melting - were monitored along the trajectories. Since the simulated trajectories may depart from the actual trajectories in nature, particularly at subgrid scales, only the large scale drift pattern was inferred from the simulated trajectories. Also, the ice thickening processes along the trajectories were interpreted as averages over 1° latitude and longitude, in order to maintain a spatial resolution close to that of the model grid.

The underestimation of ice around Victoria Land in the summer in the model should have little effect on our analysis since our interest in this area is restricted to the months of March to May. During the interpretation of the results of the analysis we took into account that the actual drift was likely to be faster and would cover more distance, especially in the north-south direction, than the simulated drift. The actual drift was also likely to be more westward in the central Ross Sea than the simulated drift as indicated by the comparison between observed and simulated drift in Section 5.7.2.

As the model underestimated the thickness of the heavily ridged ice near the continent in January 1999, we focussed on examining the backward trajectories of floes which were north of 72°S along the 165°W and 150°W in January 1999 (Fig. 5.1). If the backward trajectories of these floes extended into the region south of 72°S we took into account that the rate of dynamic thickening in this region was likely to be underestimated.

5.9 Results of backward trajectory analysis

5.9.1 Backward trajectories initiated along 180° on May 15, 1998

Backward trajectories were initiated at the location of ten summary observations along 180° on May 15, 1998 (Fig. 5.1). The resultant floe trajectories (to be described forward in time) fell into two main groups. Northwest (NW) trajectories originated from the central Ross Sea near 180°, on or just after March 15, 1998 and followed a mean path along 180° northward (Fig. 5.5, trajectory a). Southwest (SW) trajectories originated from the southwestern Ross Sea usually between mid March and mid April and travel northeastward (Fig. 5.5, trajectory b). Out of the ten floe trajectories there were six NW

and four SW trajectories, respectively.

Thermodynamic thickening was the predominant ice thickening process along both trajectories (Fig. 5.6). It is the net amount of ice thickness increase arising from ice growth at the base of existing ice, new ice formation over open water and basal melt (Section 5.6.1.1.2). It was active throughout the period of March to May, with peak activity taking place at the end of March (Fig. 5.6a). Along the trajectories, the rate of thermodynamic thickening decreased with time which coincided with the floes reaching more northerly latitudes (Fig. 5.7). Dynamic thickening became active after the end of March (Fig. 5.6b) and although thermodynamic thickening was the predominant process, dynamic thickening contributed a mean of 20% towards the total thickening rate along the trajectories (Fig. 5.6g). Snow ice formation was negligible along these trajectories (Fig. 5.6c), as was melting, except for a few isolated melt episodes (Fig. 5.6d). The lack of snow ice formation was due to a small ratio between snow and ice thickness arising from a combination of low snow thickness and high ice thickness (Figs. 5.6e and f).

5.9.2 Backward trajectories initiated along 165°W and 150°W on January 15, 1999

Backward trajectories were initiated at the location of seven summary observations along 165°W on January 15, 1999 (Fig. 5.1). All floe trajectories originated from the western front of Marie Byrd Land on March 15, 1998 (Fig. 5.5, trajectories c and d). They traveled westward into the Ross Sea and turned northward between 165°W and 175°W. Some floes drifted further north where they joined the Antarctic Circumpolar Current and then turned towards the northeast (Fig. 5.5, trajectory c). Since trajectories differed little except in total displacement, all these trajectories were analyzed together and referred to as Central (C) trajectories.

Backward trajectories were also initiated at the location of nine summary observations along 150°W on January 15, 1999 (Fig. 5.1). These floe trajectories were categorized as Northeast (NE), Gyre (G) or Amundsen (A) trajectories. Three NE trajectories originated

west of 150°W, in the Ross Sea on March 15, 1998. They initially traveled northwestward until they joined the Antarctic Circumpolar Current at which time they turned towards the northeast (Fig. 5.5, trajectory e). Five G trajectories originated close to 150°W in March 1998. They appeared to be trapped in the center of the Ross Gyre, resulting in little overall displacement along these trajectories (Fig. 5.5, trajectory f). The two A trajectories originated east of 150°W, in the Amundsen Sea and traveled westward with the coastal currents and the easterly winds (Fig. 5.5, trajectory g).

For C, NE and A trajectories, thermodynamic thickening was insignificant after the beginning of May (Figs. 5.8a and 5.9a). Dynamic thickening and melting were the main processes that competed to determine ice thickness (Figs. 5.8b,d and 5.9b,d). Rates of snow ice formation were higher along these trajectories than NW and SW trajectories (Figs. 5.6c, 5.8c and 5.9c) and were particularly widespread along NE and A trajectories (Fig. 5.9c).

For C and NE trajectories, peak dynamic thickening activity was found between the beginning of May and end of October (Figs. 5.8b and 5.9b). This occurred in the region south of 75°S and on both sides of 160°W along C trajectories, and in the region of 70°S and 160°W along NE trajectories (Fig. 5.10). Along C trajectories, dynamic thickening rates decreased towards the north while they decreased both towards the northern ice edge and the continent along NE trajectories (Fig. 5.10a). Dynamic thickening also took place between the beginning of May and the end of October along A trajectories although peak activity was concentrated at the beginning of June and the beginning of October (Fig. 5.9b), corresponding to the region of 73°S and 120°W and 140°W, respectively (Fig. 5.10). Events of high dynamic thickening activity were accompanied by events of high oceanic heat flux and high winds (Figs. 5.8, 5.9 and 5.11). Dynamic thickening rates were significantly reduced after the beginning of December which was also a trend seen in the ice concentration (Fig. 5.8a,g and 5.9a,g).

Along C, NE and A trajectories melting took place during three melt episodes. The first episode began on March 15, 1998 and lasted until the end of April, 1998. The second

episode started at the end of May, 1998 and ended at the end of October, 1998. The third episode went from the beginning of December, 1998 to January 15, 1999 (Figs. 5.8d and 5.9d). Along C and NE trajectories, the first and third melt episodes coincided with the furthest south and furthest north latitudes at the beginning and end of the trajectories, respectively (Fig. 5.12). A trajectories followed a predominantly zonal path from east to west hence, the first and third melt episodes coincided with the furthest east and furthest west longitudes, respectively (Fig. 5.12). The second melt episode took place along C, NE and A trajectories at various latitudes and longitudes (Fig. 5.12). This points to time rather than location as the primary control over the onset of melt episodes. For all C, NE and A trajectories, events of high melting activity during the second melt episode coincided with events of high dynamic thickening activity and oceanic heat flux (Figs. 5.8b, d and 5.9b, d).

Snow ice formation was widespread along all backward trajectories initiated along 150°W (Fig. 5.11a). It occurred between the beginning of May and end of October which also coincided with the second melt episode and the period of peak dynamic thickening activity (Figs. 5.11a and d). During this period, snow accumulated on increasingly thicker ice, maintaining a ratio between snow and ice thickness which was consistently greater than 0.3 (Figs. 5.11 b and c). According to Eqn. 15, this is the value which would result in flooding, assuming that the densities of snow, sea ice and seawater are 300 kg m^{-3}, 900 kg m^{-3} and 1020 kg m^{-3}, respectively. Between the beginning of May and end of October, events of high snow ice formation rates were accompanied by events of high precipitation and wind velocities (Fig. 5.11). Prior to and after this period, there was insufficient snow accumulation to cause flooding, even during high precipitation events.

5.10 Discussion

5.10.1 Evolution of sea ice thickness in the Ross Sea

Backward trajectories initiated along 180° (NW and SW trajectories) followed the

evolution of first year ice found in the central Ross Sea over a period of two months. This spanned the period from the end of the 97/98 melt season to its observation in May 15, 1998. On the other hand, backward trajectories initiated along 165°W and 150°W (C, NE, A and G trajectories) followed the evolution of ice of the residual ice field northeast on the continental shelf in January 1999 over ten months, a period which spanned the end of the 98/99 melt season to the beginning of the 99/00 melt season.

NW and SW trajectories indicated that the first year ice which was found in the central Ross Sea in May 1998 originated from the southern and southwestern Ross Sea, in the zone of the Ross Polynya, and then drifted northward. The floes experienced decreasing thermodynamic thickening as they drifted northward. This is partly due to higher temperatures at more northerly latitudes slowing down thermodynamic thickening. A reduction in shear deformation of the ice cover may also reduce the amount of open water created and subsequently lowered the amount of new ice formed. In addition, as the floes thickened with time, increased ice thickness and snow accumulation reduced the vertical temperature gradient across the ice, which retarded thermodynamic thickening. Dynamic thickening rates were naturally small during this time because ice floes were young and thin (Fig. 5.6e). Although dynamic thickening can increase ice thickness by several hundred percent, the absolute magnitude will still be small if the original ice floes are thin. According to model results, the floes did not experience significant snow ice formation and melting during this period.

Model results partially corroborate with ice core data collected during NBP 98-3. Ice cores showed a majority of congelation ice, reflecting the dominance of thermodynamic thickening (Jeffries et al., 2001). Frazil ice made up one third of the total ice mass and its abundance indicated the significance of dynamic thickening. The final 10% of the mass in the ice cores was made up of snow ice that occurred in insignificant amounts along the model trajectories. Although the percentage of snow ice can potentially be halved if a different identification criterion is used (Maksym, 2001), there is still a non-negligible amount of snow ice in the ice cores which is not reproduced by the model. This arises

from an underestimation of snow thickness and an overestimation of ice thickness along NW and SW trajectories. Mean snow and ice thicknesses for this area during this period were 0.15 m and 0.65 m, respectively (Jeffries and Adolphs, 1997). An underestimation of snow thickness of less than 0.01 m or overestimation of ice thickness of less than 0.5 m effectively inhibits flooding and snow ice formation. The model overestimates ice thickness by only 0.05 m to 0.7 m but, together with an underrepresentation of precipitation in the NCEP reanalysis data, flooding is inhibited. As a result, while the model trajectories present a realistic balance between the roles of thermodynamic and dynamic thickening, the role of snow ice formation is underestimated.

C, NE, A and G trajectories indicate that ice floes in the residual ice field in January 1999 were in the eastern Ross Sea and the Amundsen Sea at the end of the 97/98 melt season. During the next ten months ice that originated from the eastern Ross Sea drifted northwestward, following the mean wind field and the large scale ocean circulation, and turned northeastward, when they joined the Antarctic Circumpolar Current. Ice from the Amundsen Sea drifted westward with the coastal currents and the prevailing easterly winds. All floes experienced significant thermodynamic thickening at the beginning of their trajectories, between March and May. After May, thermodynamic thickening slowed down due to the insulating effect of over 1.5 m of ice and 0.3 m of snow (Figs. 5.8 and 5.9) and dynamic thickening, melting and snow ice formation were the dominant processes which determined ice thickness. By November, all other processes were insignificant and melting dominated. Evidence of the activity of all four processes was also seen in ice cores obtained during NBP 99-1 (Jeffries, unpublished data).

Dynamic thickening, melting and snow ice formation were simultaneously active in winter, during the period between the beginning of May and the end of October. The coincidence between peak dynamic thickening and peak melting activity can be explained by increased heat flux arising from ice deformation. Ice core and oceanographic data obtained in October 1994, around 150°W, in the region covered by C and G trajectories, indicated widespread melting at the bottom of the sea ice as well as warm water

upwelling in the Ross Gyre (Jeffries et al., 2001; Jeffries et al., 1995). This agreed with model results which indicated that events of high dynamic thickening activity were accompanied by events of high melting and high oceanic heat flux. This is because, during shear deformation of the ice cover, open water is simultaneously increased while existing floes thicken as they are piled up (Flato and Hibler, 1991). Ice forms readily over open water at low air temperatures. As new ice forms, cold dense brine is released into the ocean, deepening the mixed layer. This in turn increases the oceanic heat flux to the bottom of the ice and induces melting. Melt rate from increased oceanic heat flux is greater than growth rate of the new ice, leading to a net decrease in ice thickness within the grid cell.

Events of peak dynamic thickening activity and snow ice formation occurred simultaneously because they were results of the same weather systems that brought high winds and precipitation. High winds resulted in ice deformation, while precipitation caused submergence of the snow/ice interface resulting in snow ice formation, provided that there was sufficient snow accumulated on the ice floes. However, after November, during the melt season at the end of the year, there was insufficient snow accumulated to induce flooding, even during high precipitation events. During this time, extensive melting had reduced the compactness of the ice pack and high internal forces did not build up, even during high wind events.

The floes which were along 165°W in January 1999 had experienced high dynamic thickening activity in the region south of 75°S and around 160°W where onshore winds (Fig. 5.13a) and ocean currents (Fig. 5.13b) induced convergent ice motion over highly compact and thick ice (Figs. 5.13c and d). For these floes and the floes which were along 150°W in January 1999, stress built up in the regions where their drift directions changed from traveling westward into the Ross Sea to traveling northwards (Fig. 5.12), contributing towards the high dynamic thickening activity in the region around 160°W.

5.10.2 Errors

As indicated in Section 5.7, there are limitations to the model's ability to reproduce the characteristics of the Ross Sea ice cover. Here, we discuss possible differences between our findings reported in this study and actual conditions in nature. We also discuss different methods for overcoming the limitations of the model and the effects that these methods may have on our findings.

Due to deficiencies in model physics and forcing fields, it is likely that actual trajectories of real floes were more westward in the Ross Sea than the simulated trajectories. Near Cape Adare, actual trajectories might have a stronger westward component than the simulated NW and SW trajectories. As a result of the coarse resolution of the NCEP atmospheric forcing fields, real trajectories in the residual ice field in 1999 might have larger displacements in the north-south direction at northern latitudes than the simulated C and NE trajectories. The parts of the simulated trajectories which were predominantly zonal, such as Amundsen trajectories, were not affected by the coarse resolution of the forcing fields in the meridional direction and should be close to actual trajectories. We would expect the net ice thickening rate to be even higher in the residual ice field in the region south of 72°S than simulated at the beginning of C trajectories, since comparisons with observations indicated that the model underestimates ice thickness in this region.

Limitations in the simulation of ice dynamics may be overcome by incorporating forcing fields of higher resolution, a realistic ice thickness distribution within each grid cell and realistic parameterizations of ice strength and atmospheric and oceanic drag. NCEP forcing fields come from a combination of field data and model output and the quality of the output depends on the availability of field data (Kalnay et al., 1996). In the polar regions, climate variables are measured regularly only at certain locations on land. It is unlikely that, in the near future, these variables, including wind speeds, air temperature, humidity, precipitation and cloudiness, will be monitored regularly over the Southern Ocean. Therefore, forcing fields over the Southern Ocean with higher spatial resolution

and quality than the existing NCEP reanalysis are not likely to be available soon. However, there is a need for more studies to independently verify the errors within the available NCEP forcing fields.

In the model used in this study, ice is represented in each grid cell as a slab with single thickness. In multi-category sea ice models, ice thickness in each grid cell is divided into several thickness classes, each with a different relative abundance, dependent on the assumed ice thickness distribution (e.g., Hibler 1980; Flato and Hibler, 1995; Lipscomb, 2001; Haapala, 2000). In nature, the sea ice cover consists of a relatively high abundance of thin ice and decreasing amounts of increasingly thicker ice (Wadhams, 1998), therefore such skewed ice thickness distributions are commonly used in multi-category sea ice models. If ice strength is then parameterized in terms of the thickness and abundance of each ice class, then both dynamic and thermodynamic thickening rates would increase as a result of increased ice deformation. Dynamic thickening rates would increase because there is a higher proportion of thinner and hence, weaker ice being piled up as the ice cover deforms. Also, shear deformation of the ice cover leads to more open water creation that allows more new ice to form thermodynamically. Similarly, it has been demonstrated that high frequency divergence events, such as those arising from inertial oscillations and tidal forcing, are common in both the Arctic and Antarctic ice cover (e.g., Geiger et al., 1997; Geiger et al., 1998; Hutchings and Hibler, 2002). These events increase the amount of new ice formation, leading to an increase of ice thickness of over 10% (Heil et al., 2001). Effects of inertial forcing can be simulated by embedding the sea ice into the ocean boundary layer, allowing the high frequency dynamics of the ocean boundary layer to be transmitted to the sea ice (Hibler et al., 1998; Heil et al., 2002). Other studies have shown that roughness features on the top and bottom surfaces of sea ice enhance the effects of winds and ocean currents on ice drift (e.g. Andreas and Claffey, 1995). This can be accounted for by including sea ice roughness in the parameterization of atmospheric and oceanic drag (Steiner et al., 1999). We expect that incorporation of inertial embedding and parameterization of ice strength based on

multiple ice thickness classes will increase the amount of thermodynamic and dynamic thickening arising from deformation of the ice cover. It is uncertain as to the effect of parameterizing drag coefficients in terms of sea ice roughness for the study region because Antarctic pressure ridges are flatter and less massive than Arctic pressure ridges (Tin and Jeffries, 2003), and their effect on atmospheric and oceanic drag is likely to be smaller than that of Arctic pressure ridges.

Drawing from our comparisons between observed and simulated ice thickness (Section 5.7.3) and the findings of previous studies (e.g., Hibler et al., 1998; Heil et al., 2002; Geiger et al., 1997; Geiger et al., 1998; Hutchings and Hibler, 2002), we conclude that the findings in this study provide lower bound estimates of the effect of ice deformation on the ice thickness distribution in the study area. A comparison between observed and simulated deformation of the ice cover would provide a quantitative measure for our underestimation of the effect of ice deformation. However, such measures are only valid exactly for the time and the region in which observations are available and are only estimates when extrapolated and applied to other areas and time periods.

In the model, snow ice formation was underestimated in the central Ross Sea in the autumn due to an overestimation of ice thickness and an underestimation of snow thickness. Including multiple ice classes in the sea ice model may improve the simulation of snow ice formation by improving the estimates of ice thickness. The simulation of snow ice formation is also influenced by the implementation of melt processes in the model. The model used in this study implements the retreat of the sea ice cover in the summer by surface melting of the complete snow cover followed by melting of the ice. However, during the melt season in the Antarctic, a snow cover, often in excess of 1 m in thickness, still remains on top of the sea ice (Morris et al., 2001). A large part of the retreat of the ice cover proceeds through lateral and bottom melting where short wave radiation is absorbed by open water and the heat melts ice floes from the sides and from the bottom (Oshima et al., 1998). Further melting increases the amount of open water

available to absorb short wave radiation which in turn accelerates melting. Lateral and bottom melting allow a thick snow cover to remain on a thinning ice floe and facilitate snow ice formation during the melt season. Hence, we would expect snow ice formation to persist later into the melt season than as represented in the model and implementation of lateral melting in the model to improve the simulation of snow ice formation.

Last but not least, in this study, the vertical component of the ocean circulation and feedbacks within the ice-ocean-atmosphere system have not been considered. Upwelling of subsurface water masses can induce melting in sea ice and even maintain polynyas (Fichefet and Goosse, 1999; Jacobs and Comiso, 1989). Cloudiness influences surface albedo (Zhou et al., 2001) which in turn affects the surface heat budget and hence determines the growth and melt of sea ice. The presence or absence of sea ice modifies the transfer of moisture between the ocean and the atmosphere which in turn influences cloud formation. The incorporation of interactions with the atmosphere and the ocean, multi-category ice thickness classes, realistic parameterizations of ice strength and atmospheric and oceanic drag and forcing fields of higher resolution may all improve the simulation of the snow and ice thickness distribution in the Southern Ocean. They may also affect the spatial and temporal variations and the relative importance of the ice thickening processes discussed in this study. However, relative to the size of the Southern Ocean, our observations and understanding of the ice thickness distribution, ice strength and interactions within the atmosphere-ice-ocean system are sparse and limited. This study has demonstrated that numerical models and detailed field observations can be used together to examine physical processes underlying observed phenomena effectively and that simple models can provide valuable insights. Features included in numerical models must be supported by physical realities in the Southern Ocean. Therefore, as far as possible, numerical experiments should be designed to support or explain field observations while field observations should provide key information needed in modeling of the physical processes. It is only by coordinating modeling and observation efforts that the vast and remote Southern Ocean sea ice cover can be explored efficiently.

5.11 Conclusions

In 1998 and 1999, we collected data on sea ice thickness, drift and ridging characteristics in the Ross Sea. In the central Ross Sea in the autumn, mean ice thickness was 0.5 m. Ice thickness increased southward from the northern ice edge and northward from the continent until it reached a maximum at 74°S. A similar pattern in the ice thickness distribution was found in the northeast Ross Sea in the summer. However, ice is generally thicker in the summer, with a mean thickness of 1.4 and maximum of 4.4 m. Higher ice thickness in the summer resulted from a combination of greater areal coverage of ridge sails, higher sail heights and higher level ice thickness. Sea ice drift in the central Ross Sea in the winter followed a northwest direction around Cape Adare, then it continued westward along the Pennell Coast and eventually joined the Antarctic Circumpolar Current and drifted eastward. Ice in the northeast Ross Sea in the summer drifted in two distinct directions: ice near the coast drifted westward, following the coastal currents while ice further north drifted eastward into the Amundsen Sea.

In order to understand the observed ice thickness distribution we used a regional sea ice-mixed layer-pycnocline model to initiate backward trajectories at the time and location of field observations and examined the dynamic and thermodynamic processes which determine ice thickness along these trajectories. We found that sea ice dynamics plays an important role in the evolution of the sea ice thickness distribution in the Ross Sea through sea ice drift, creation of open water and piling of existing ice volume during deformation events. We found that first year ice in the central Ross Sea in the winter originated from the southern and southwestern Ross Sea, in the zone of the Ross Polynya. Both our model results and previously published ice core data indicate that thermodynamic thickening, which is the net effect of ice growth at the base of existing ice, new ice formation over open water and basal melt, is the dominant process that determine thickness of this first year ice in the central Ross Sea. Dynamic thickening, which is a result of piling of existing ice during deformation of the ice cover, also plays a significant role and is responsible for 20% of the net thickening rates. Contrary to ice core

data, model results do not indicate that snow ice forms a significant fraction of mass of this ice as a result of an underrepresentation of precipitation in the model forcing fields and an overestimation of ice thickness by the model. For the residual ice field in the northeast Ross Sea in the summer, all four processes of ice thickening – thermodynamic thickening, dynamic thickening, melting and snow ice formation – have contributed significantly to the total ice mass during the previous year. Thermodynamic thickening is significant only in autumn and at the beginning of winter, the other three processes are active during the winter and spring, and melting dominates in summer. In winter, the balance between dynamic thickening, snow ice formation and melting determine whether there is a net thickening or thinning of the ice. During this time, high winds acting on the compact ice cover causes deformation and leads to high dynamic thickening activity. The winds are accompanied by ample precipitation which leads to the formation of snow ice. As the ice cover deforms, open water is increased simultaneously as existing floes are thickened as they are piled up. New ice formation in the open water releases brine into the ocean, deepens the mixed layer, increases the amount of oceanic heat flux and induces melting at the bottom surface of the ice. Model results are supported by evidence of dynamic thickening, snow ice formation and bottom melting present in ice cores and evidence of warm water upwelling in oceanographic data. Apart from time, geographical location also exerts influence over the activity of ice thickening processes. For first year ice in the central Ross Sea, warm temperatures at northerly latitudes reduce thermodynamic thickening rates. For the summer residual ice field, onshore atmospheric and oceanic forcing results in high dynamic thickening activity near the coast around 160eW. Further north, along the same longitude, stress builds up as drift directions change from westward to northward and increases dynamic thickening rates. Our findings provide lower bound estimates of the effect of ice deformation on the ice thickness distribution in the study area. The effect in nature is likely to be greater.

This study has demonstrated that numerical models and detailed field observations can be used together to examine physical processes underlying observed phenomena

effectively and that simple models can provide valuable insights. The Southern Ocean sea ice cover is vast and remote and it is only be coordinating modeling and observation efforts that it can be explored efficiently.

5.12 Acknowledgments

Thanks to everyone onboard the R/V Nathaniel B. Palmer during NBP 98-3 and NBP 99-1 for making fieldwork such an enjoyable experience. Thanks to Paul Bond, Camille Li, Shusun Li, Nick Kozlenko, Ted Maksym, Kim Morris, Dan Naber, Jean-Louis Tison and Xiaobing Zhou for helping to collect the ASPeCt data at all times of the night. Thanks to Nick Kozlenko for primary processing of buoy data. This study was funded jointly by NSF grant OPP-9614844, a Thesis Completion Fellowship from the Graduate School of UAF and by the Geophysical Institute, UAF. A Global Change Student Research Grant from the Center for Global Change and Arctic System Research, UAF and a Student Travel Grant from the College of Science, Engineering and Mathematics at UAF made TT's visit to UCL possible. Sincere thanks to Karen Assmann who initiated the collaboration by introducing TT and RT, and for providing the model grid and forcing fields. NCEP forcing fields were obtained from the NOAA-CIRES Climate Diagnostics Center, Boulder, Colorado.

5.13 Figures

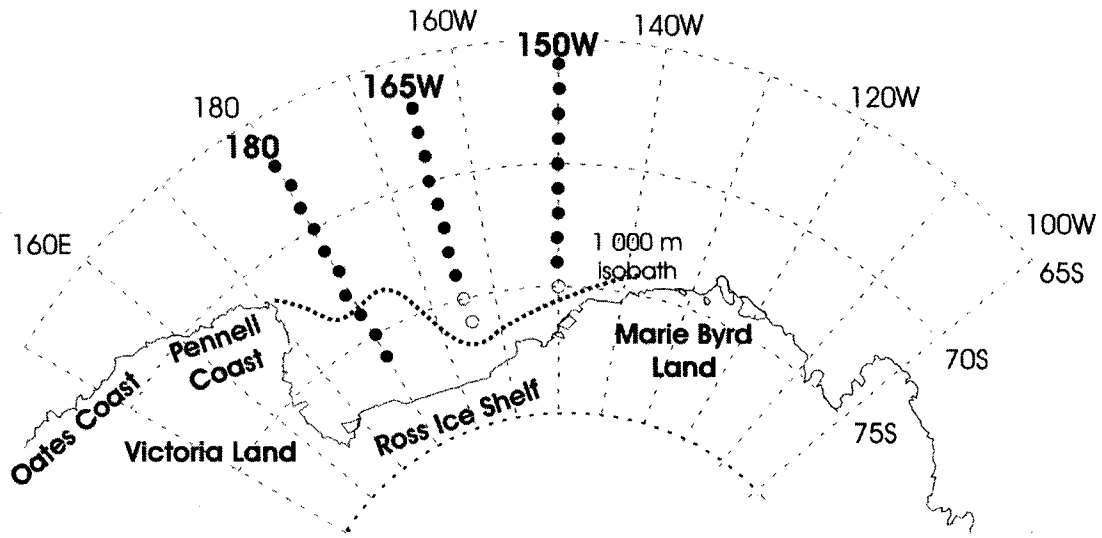

Figure 5.1 Locations of summary ASPeCt observations in the Ross Sea. Circles indicate locations of summary ASPeCt observations made along the 180 longitude during NBP 98-3 and along 165W and 150W during NBP 99-1. Closed circles (•) represent locations of summary observations which are used to initiate backward trajectories in our study. Each summary observation is derived from averaging observations within the same 1 degree latitude bin. The dotted line represents the approximate location of the 1 000 m isobath which is considered as the edge of the continental shelf.

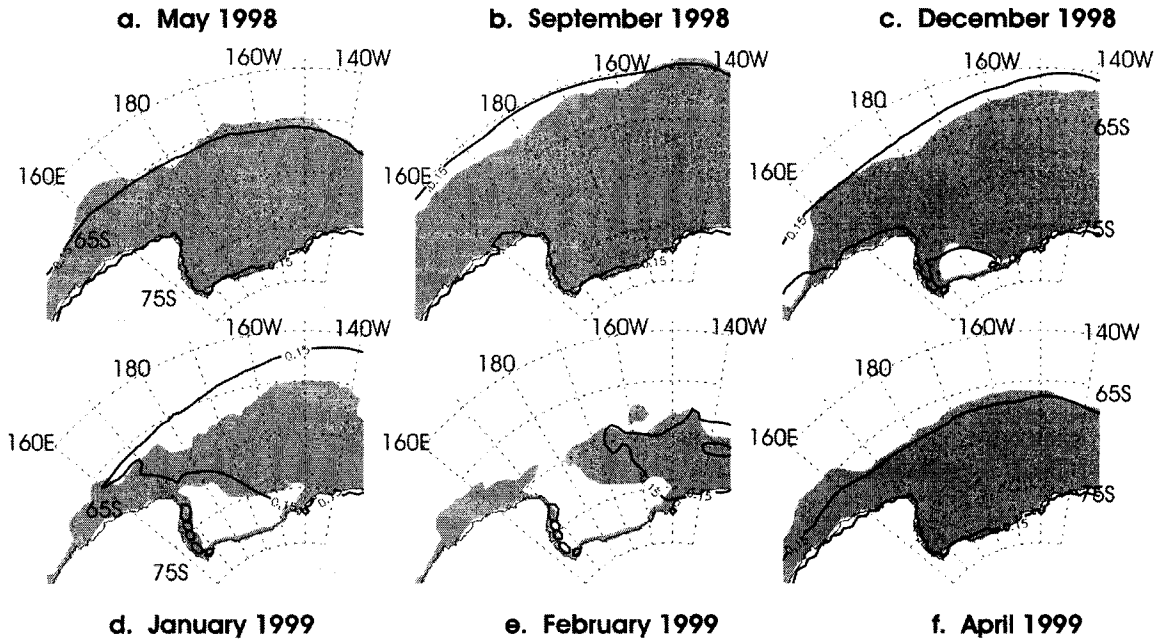

Figure 5.2 Observed and simulated seasonal evolution of sea ice extent. Shaded areas indicate ice concentrations of >15% from special sensor microwave imager (SSM/I) data in 1998 and 1999. Solid contour lines indicate the simulated ice edge as defined by ice concentration of 15% from model simulations.

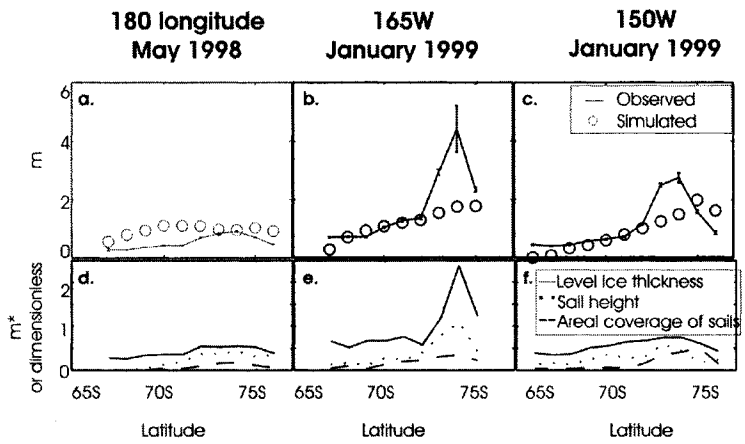

Figure 5.3 Observed and simulated ice thickness. **a.**, **b.**, and **c.** plot equivalent thickness derived from ASPeCt observations (-) and ice thickness simulated by the model (o) along **a.** 180 longitude in May 1998, **b.** 165W in January 1999, and **c.** 150W in January 1999. Equivalent thickness is plotted together with error bars. **d.**, **e.** and **f.** plot observed level ice thickness (-), ridge sail height (. .) and areal coverage of sails (--) along **d.** 180 longitude in May 1998, **e.** 165W in January 1999 and **f.** 150W in January 1999, as recorded in ASPeCt observations. *For **d.**, **e.** and **f.**, the vertical axis assumes the units of m in the cases of level ice thickness and sail height and is dimensionless for the case of areal coverage of sails.

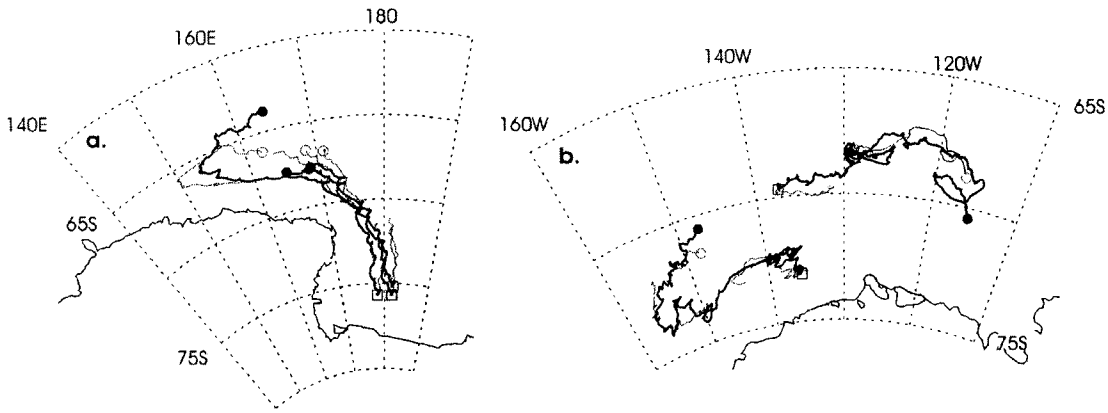

Figure 5.4 Observed and simulated ice drift. Observed (-) and simulated (-) drift tracks of buoys deployed during **a.** NBP 98-3 in May 1998 and during **b.** NBP 99-1 in January 1999. (□) denote the locations of deployments. (•) denote the end of observed drift tracks. (o) denote the end of simulated drift tracks. After every 60 days, simulated buoys are restarted at the location of the observed drift track.

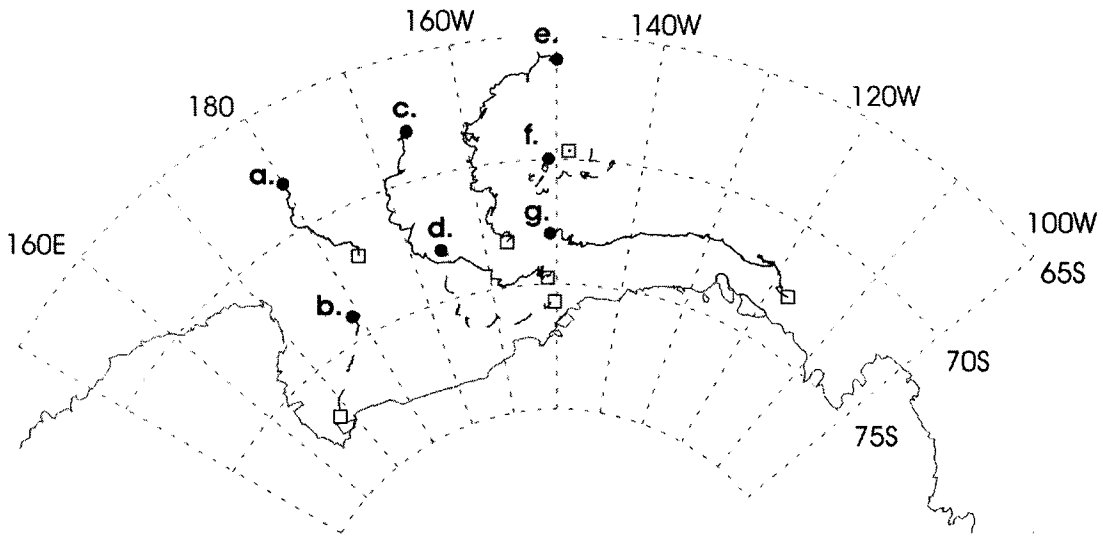

Figure 5.5 Backward trajectories initiated at locations of ASPeCt summary observations. Examples of the simulated trajectories of ice floes prior to their encounter with cruises NBP 98-3 and NBP 99-1. The groups of trajectories are referred to as **a.** Northwest (NW), **b.** Southwest (SW), **c.** and **d.** Central (C), **e.** Northeast (NE), **f.** Gyre (G), and **g.** Amundsen (A) trajectories. Described forward in time, (□) denote the beginning of the trajectories, which were two months prior to observation in the case of ice along 180 longitude and ten months prior ot observation in the case of ice along 175W and 150W. (•) denote the end of the trajectories, i.e., at the location of observation.

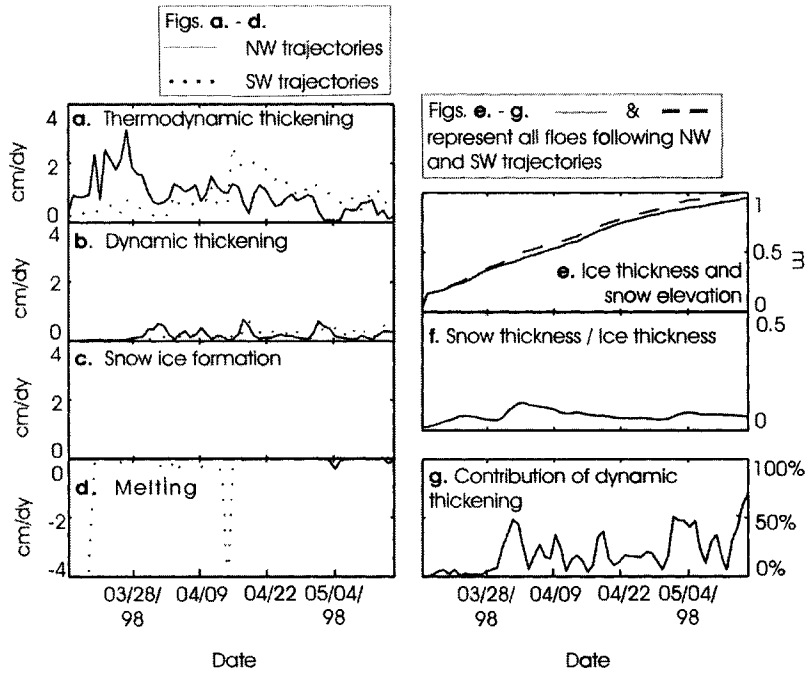

Figure 5.6 Processes and characteristics of floes observed along 180 longitude in May 1998. **a.** Thermodynamic thickening, **b.** dynamic thickening, **c.** snow ice formation, and **d.** melting rates along the trajectories of floes represented by Northwest (NW) (-) and Southwest (SW) (. .) trajectories. **e.** Ice thickness (-) and snow elevation (--), **f.** ratio between snow thickness and ice thickness (snow thickness / ice thickness), and **g.** contribution of dynamic thickening to net ice thickening rates for all floes represented by NW and SW trajectories. Snow elevation is the sum of ice thickness and snow thickness. The vertical distance between (-) and (--) is the snow thickness.

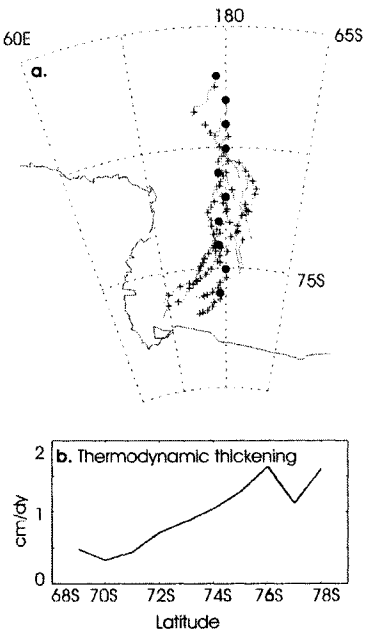

Figure 5.7 Thermodynamic thickening along NW and SW trajectories. **a.** (+) denote rates of > 0.5 cm/dy. (•) are the locations of the ASPeCt summary observations and are assumed to be the locations of the hypothesized ice floes on May 15, 1998. Lines indicate simulated trajectories of the hypothesized ice floes between March 15, 1998 and May 15, 1998. **b.** Variation of thermodynamic thickening rates with latitude, averaged along both Northwest (NW) and Southwest (SW) trajectories.

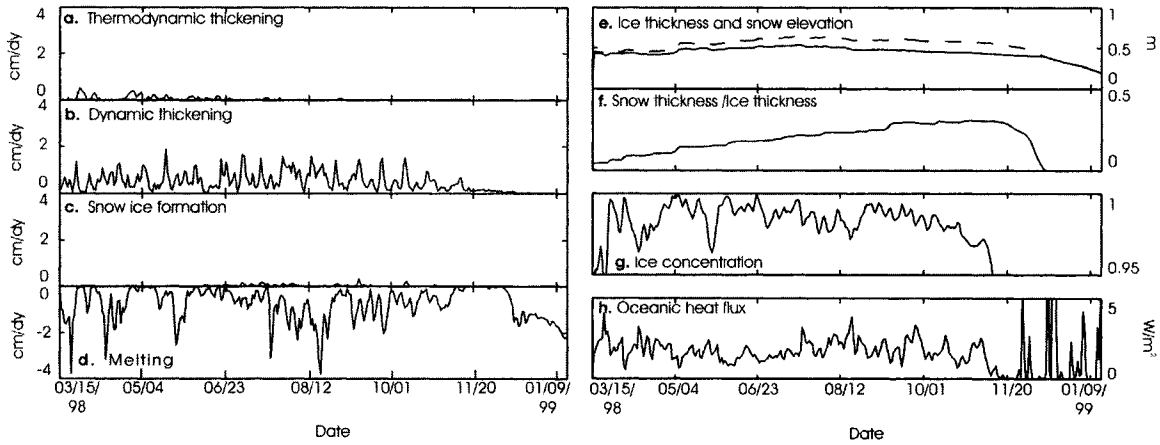

Figure 5.8 Processes and characteristics of floes observed along 165W in January 1999. **a.** Thermodynamic thickening, **b.** dynamic thickening, **c.** snow ice formation, and **d.** melting rates, **e.** ice thickness (-) and snow elevation (--), **f.** ratio between snow thickness and ice thickness (snow thickness / ice thickness), and **g.** ice concentration, and **h.** oceanic heat flux. All floes are represented by Central (C) trajectories. Snow elevation is the sum of ice thickness and snow thickness. The vertical distance between (-) and (--) is the snow thickness.

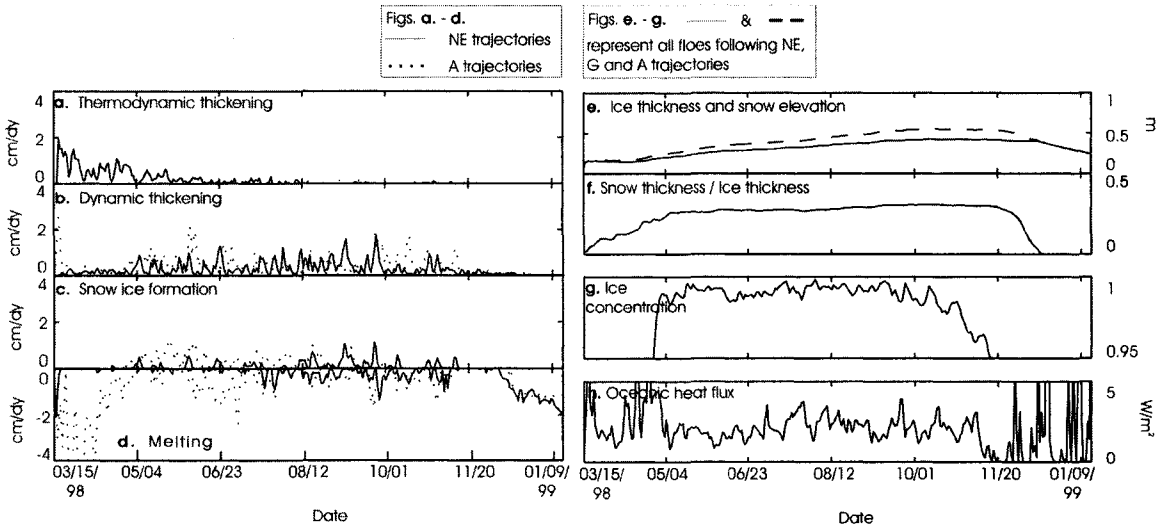

Figure 5.9 Processes and characteristics of floes observed along 150W in January 1999. **a.** Thermodynamic thickening, **b.** dynamic thickening, **c.** snow ice formation, and **d.** melting rates along the trajectories of floes represented by Northeast (NE) (-) and Amundsen (A) (. .) trajectories. **e.** Ice thickness (-) and snow elevation (--), **f.** ratio between snow thickness and ice thickness (snow thickness / ice thickness), and **g.** contribution of dynamic thickening to net ice thickening rates for all floes represented by NE, Gyre (G) and A trajectories. Snow elevation is the sum of ice thickness and snow thickness. The vertical distance between (-) and (--) is the snow thickness.

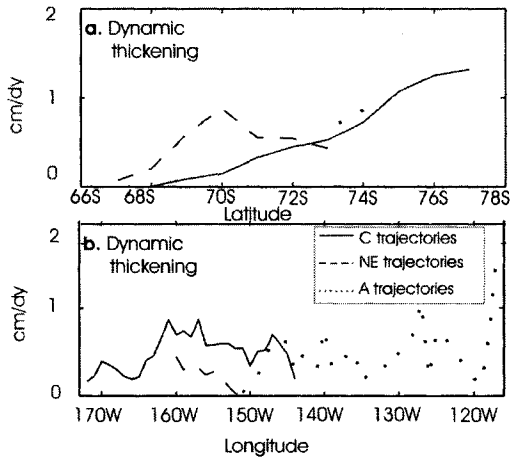

Figure 5.10 Dynamic thickening along NE, G and A trajectories. Variation of rates of dynamic thickening with **a.** latitude and **b.** longitude along Central (C) (-), Northeast (NE) (--) and Amudsen (A) (..) trajectories.

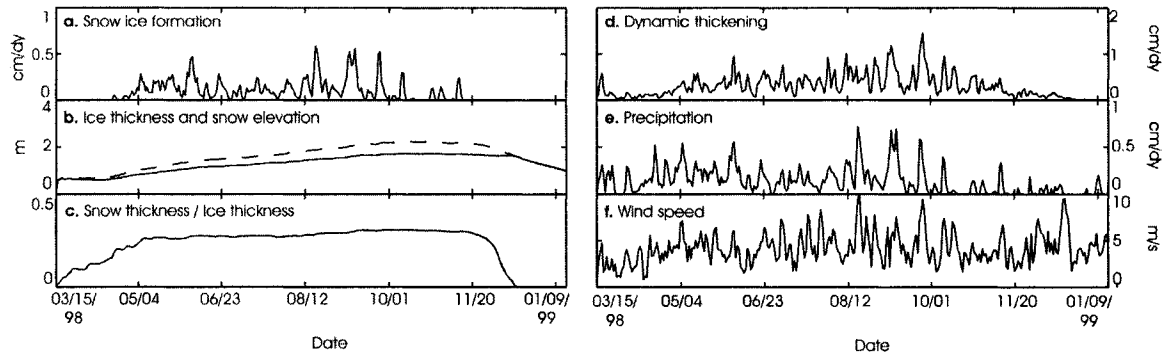

Figure 5.11 Forcing and processes of floes observed along 150W in January 1999. **a.** Snow ice formation, **b.** Ice thickness (-) and snow elevation (--), **c.** ratio between snow thickness and ice thickness (snow thickness / ice thickness), **d.** dynamic thickening, **e.** precipitation, and **f.** wind speeds all floes represented by Northeast (NE), Gyre (G) and Amundsen (A) trajectories. Snow elevation is the sum of ice thickness and snow thickness. The vertical distance between (-) and (--) is the snow thickness.

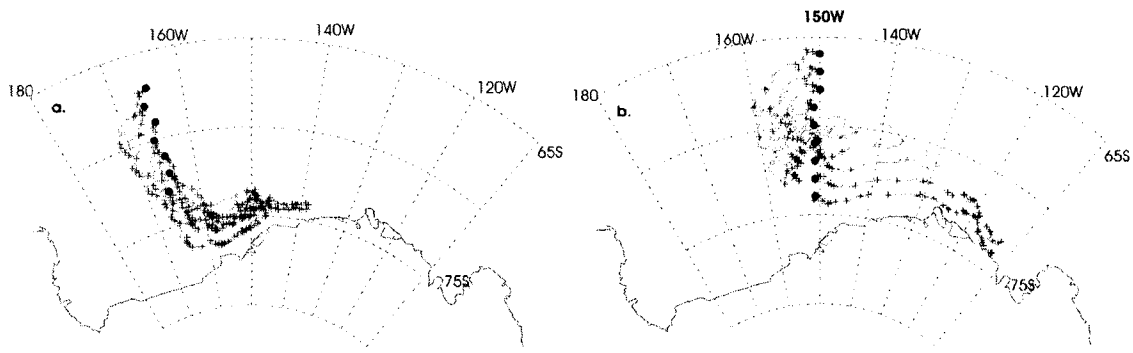

Figure 5.12 Melting along C, NE, G and A trajectories. Rates of melting along **a.** Central (C), **b.** Northeast (NE), Gyre (G) and Amundsen (A) trajectories. (+) denote rates of > 0.5 cm/dy. (•) are the locations of the ASPeCt summary observations and are assumed to be the locations of the hypothesized ice floes on January 15, 1999. Lines indicate simulated trajectories of the hypothesized ice floes between March 15, 1998 and January15, 1999. Around 150W is a region of high melting which is associated with warm water upwelling in the Ross Gyre.

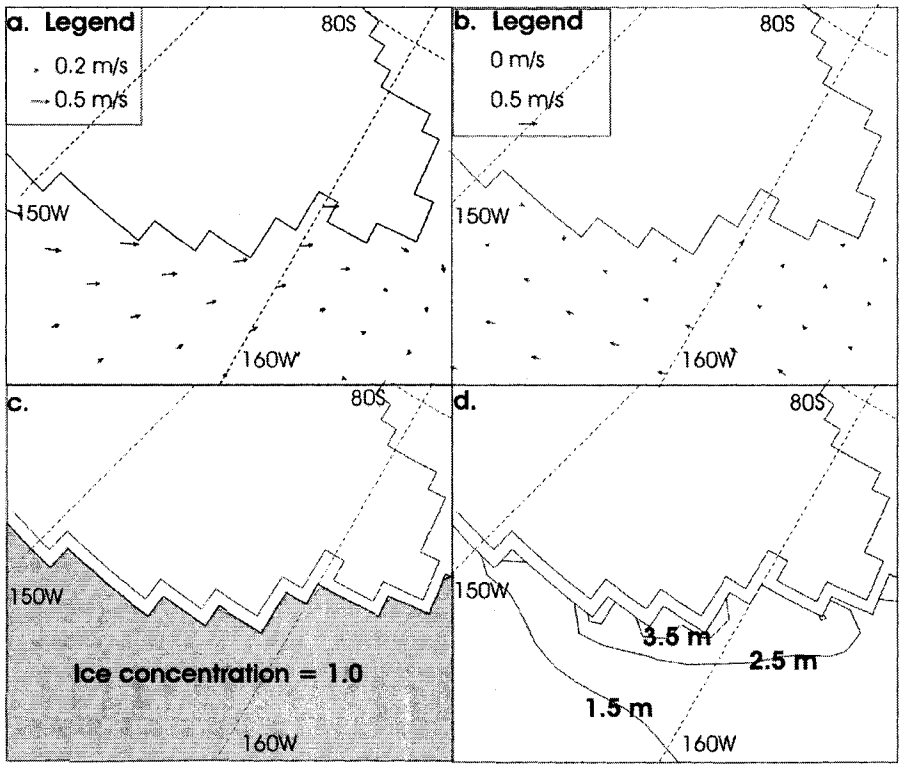

Figure 5.13 Model forcing and simulated ice conditions near 75S, 160W in May 1998. Average **a.** wind velocities, **b.** ocean currents, **c.** ice concentration, and **d.** ice thickness in May 1998 in the vicinity of 75S, 160W, as simulated by the model.

5.14 References

Andreas, E.L. and K.J. Claffey. 1995. Air-ice drag coefficients in the western Weddell Sea 1. Values deduced from profile measurements. *Journal of Geophysical Research*, 100(C3), 4821-4831.

Arrigo, K.R., Weiss, A.M. and Smith, W.O. 1998. Physical forcing of phytoplankton dynamics in the southwestern Ross Sea. *Journal of Geophysical Research*, 103(C1), 1007-1021.

Assmann, K., Hellmer, H.H. and Beckmann, A. 2003. Seasonal variation in circulation and watermass distribution on the Ross Sea continental shelf. *Antarctic Science*, 15(1).

Bromwich, D.H. and Kurtz, D.D. 1984. Katabatic wind forcing of the Terra Nova Bay polynya. *Journal of Geophysical Research*, 89(C3), 3561-3572.

Bromwich, D., Liu, Z., Rogers, A.N. and Van Woert, M.L. 1989. Winter atmospheric forcing of the Ross Sea polynya. In: Jacobs, S.S. and Weiss, R.F. (eds.) *Ocean, ice, and atmosphere: interactions at the Antarctic continental margin*, Antarctic Research Series, vol. 75, 101-133. American Geophysical Union, Washington, D.C.

Flato, G.M. and Hibler, W.D., III. 1995. Ridging and strength in modeling the thickness distribution of arctic sea ice. *Journal of Geophysical Research*, 100(C9), 18,611-18,626.

Flato, G.M., Hibler, W.D., III. 1991. Initial numerical investigation of the extent of sea-ice ridging. *Annals of Glaciology*, (15), 31-36.

Fichefet, T. and Goosse, H. 1999. Numerical investigation of the spring Ross Sea polynya. *Geophysical Research Letters*, 26(8), 1015-1018.

Fischer, H. and Lemke, P. 1994. On the required accuracy of atmospheric forcing fields for driving dynamic-thermodynamic sea ice models. In: Johannessen, O.M, Muench, R.D. and Overland, J.E. (eds.) *The polar oceans and their role in shaping the global environment*, Geophysical Monograph, vol. 85, 373-381. American Geophysical Union, Washington, D.C.

Geiger, C.A., Ackley, S.F. and Hibler, W.D., III. 1998. Sea ice drift and deformation processes in the western Weddell Sea. *In:* Jeffries, M.O. (ed.) *Antarctic sea ice: physical processes, interactions and variability*. Antarctic Research Series v. 74, American Geophysical Union, Washington D.C., 141-160.

Geiger, C.A., Ackley, S.F. and Hibler, W.D., III. 1997. Year-round pack ice in the western Weddell Sea, Antarctica: response and sensitivity to atmospheric and oceanic forcing. *Annals of Glaciology*, (25), 269-275.

Geiger, C.A., Hibler, W.D., III and Ackley, S.F. 1998. Large-scale sea ice drift and deformation: comparison between models and observations in the western Weddell Sea during 1992. *Journal of Geophysical Research,* 103(C10), 21893-21913.

Haapala, Jari. 2000. On the modelling of ice-thickness redistribution. *Journal of Glaciology*, 46(154), 427-437.

Harder, M. 1994. Roughness, age and drift trajectories of sea ice in large-scale simulations and their use in model verifications. *Annals of Glaciology*, 25, 237-240.

Harder, M. and Fischer, H. 1999. Sea ice dynamics in the Weddell Sea simulated with an optimized model. *Journal of Geophysical Research*, 104 (C5), 11151-11162.

Harder, M. and Lemke, P. 1994. Modelling the extent of sea ice ridging in the Weddell Sea. In: Johannessen, O.M, Muench, R.D. and Overland, J.E. (eds.) *The polar oceans and their role in shaping the global environment*, Geophysical Monograph, vol. 85, 187-197. American Geophysical Union, Washington, D.C.

Heil, P., Allison, I. And Lytle. 2001. Effect of high-frequency deformation on the sea-ice thickness. In: Dempsey, J.P. and Shen, H.H. (eds.) *Scaling laws in ice mechanics and ice dynamics*. Solid mechanics and its applications, 94, Kluwer Academic Publishers, 417-426.

Heil, P. and Hibler, W.D. III. 2002. Modeling the high-frequency component of Arctic sea-ice drift and deformation. *Journal of Physical Oceanography*, 32 (11), 3039-3057.

Hibler, W.D., III. 1984. The role of sea ice dynamics in modeling CO2 increases. *In:*

Hansen, J.E. and Takahashi T. (eds.) *Climate process and climate sensitivity*, American Geophysical Union, Washington, D.C., 238-253.

Hibler, W.D., III. 1980. Modeling a variable thickness sea ice cover. *Monthly Weather Review*, 108(12), 1943-1973.

Hibler, W.D. III. 1979. A dynamic thermodynamic sea ice model. *Journal of Physical Oceanography*, (9), 815-846.

Hibler, W.D., III and Ackley, S.F. 1983. Numerical simulation of the Weddell Sea pack ice. *Journal of Geophysical Research*, 88(C5), 2873-2887.

Hibler, W.D., III, Schulson, E.M. 1999. Fracture propagation characteristics of an anisotropic model of flawed sea ice. *In:* Shen, H.T. (ed.) *Proceedings of 14th International Symposium on Ice. Ice in surface waters*. Potsdam, NY, USA, 27-31 July 1998. Vol. 1, Rotterdam. A.A. Balkema, 1033-1040.

Hibler, W.D., III and Walsh, J.E. 1982. On modeling seasonal and interannual fluctuations of Arctic sea ice. *Journal of Physical Oceanography*, 12, 1514-1523.

Hibler, W.D., Heil, P. and Lytle, V.I. 1999. On simulating high-frequency variability in Antarctic sea-ice dynamics models. *Annals of Glaciology*, 27, 443-448.

Hutchings, J.K. and Hibler, W.D. III. 2002. Modelling sea ice deformation with a viscous-plastic isotropic rheology. *In:* Shen, H.T. (ed.) *Proceedings of 16th International Symposium on Ice. Ice in the environment*. Dunedin, New Zealand, 2-6 December 2002. Vol. 2, 358-366.

Ip, C.F., Hibler, W.D., III and Flato, G.M. 1991. On the effect of rheology on seasonal sea-ice simulations. *Annals of Glaciology*, (15), 17-25.

Jacobs, S.S. and Comiso, J.C. 1989. Sea ice and oceanic processes on the Ross Sea continental shelf. *Journal of Geophysical Research*, 94(C12), 18195-18211.

Jeffries, M.O. unpublished data. Data collected on cruise NBP 99-1.

Jeffries, M.O. and Adolphs, U. 1997. Early winter ice and snow thickness distribution, ice structure and development of the western Ross Sea pack ice between the ice edge and the Ross Ice Shelf. *Antarctic Science*, 9(2), 188-200.

Jeffries, M. O. and Kozlenko, N. 2002. Buoy deployments in the Ross Sea pack ice, 1998 and 1999. *International programme for Antarctic buoys : Report of the third meeting of programme participants*, WMO/WCRP, Geneva, Switzerland, WCRP Informal Report No. 5/2002, 11-17.

Jeffries, M.O. and Weeks, W.F. 1992. Structural characteristics and development of sea ice in the western Ross Sea. *Antarctic Science*, 5(1), 63-75.

Jeffries, M.O., Jaña, R., Li, S. and McCullars, S. 1995. Sea-ice-and snow-thickness distributions in late winter 1993 and 1994 in the Ross, Amundsen, and Bellingshausen Seas. *Antarctic Journal of the United States*, 30(1-4), 18-21.

Jeffries, M.O., Krouse, H.R., Hurst-Cushing, B. and Maksym, Ted. 2001. Snow-ice accretion and snow-cover depletion on Antarctic first-year sea-ice floes. *Annals of Glaciology*, (33), 51-60.

Jeffries, M.O., Shaw, R.A., Morris, K., Veazey, A.L. and Krouse H.R. 1994. Crystal structure, stable isotopes ($\delta^{18}O$), and development of sea ice in the Ross, Amundsen, and Bellingshausen Seas, Antarctica. *Journal of Geophysical Research*, 99(C1), 985-995.

Kurtz, D.D. and Bromwich, D.H. 1983. Satellite observed behavior of the Terra Nova Bay polynya. *Journal of Geophysical Research*, 88(C14), 9717-9722.

Leppäranta, M. and Hibler, W.D., III. 1987. Mesoscale sea ice deformation in the East Greenland marginal ice zone. *Journal of Geophysical Research*, 92(C7), 7060-7070.

Lemke, P., W.B. Owens, Hibler, W.D.III, 1990. A coupled sea ice-mixed layer-pycnocline model for the Weddell Sea. *Journal of Geophysical Research*, 95 (C6), 9513-9525.

Leppäranta, M. 1983. A growth model for black ice, snow ice and snow thickness in subarctic basins. *Nordic Hydrology*, 14(2), 59-70.

Lipscomb, W.H. 2001. Remapping the thickness distribution in sea ice models. *Journal of Geophysical Research*, 106 (7), 13989-14000.

Lemke, P. 1987. A coupled one-dimensional sea ice-ocean model. *Journal of Geophysical Research*, 92(C12), 13164-13172.

Maksym, T. 2001. Brine percolation, flooding and snow ice formation on Antarctic sea ice. Ph.D. thesis. University of Alaska Fairbanks, USA.

McPhee, M.G. 1980. An analysis of pack ice drift in summer. In: Pritchard, R.S. (ed.) *Sea ice processes and models*. University of Washington Press, Seattle.

McPhee, M.G. 1979. The effect of the oceanic boundary layer on the mean drift of pack ice: Application of a simple model. *Journal of Physical Oceanography*, (9), 388-400.

Moritz, R.E. 1988. Ross Sea data buoy project, 1986-1988. *Antarctic Journal of the United States*, 23(5), 78-80.

Morris, K. and Jeffries, M.O. 2001. Seasonal contrasts in snow-cover characteristics on Ross Sea ice floes. *Annals of Glaciology* (33), 61-68.

Ohshima, K.I., Yoshida, K., Shimoda, H., Wakatsuchi, M., Endoh, T. and Fukuchi, M. 1998. Relationship between the upper ocean and sea ice during the antarctic melting season. *Journal of Geophysical Research* , 103(C4), 7601-7615.

Owens, W.B. and Lemke, P. 1990. Sensitivity studies with a sea ice-mixed layer-pycnocline model in the Weddell Sea. *Journal of Geophysical Research*, 95(C6): 9527-9538.

Semtner, A.J. 1976. A model of the thermodynamic growth of sea ice in numerical investigations of climate. *Journal of Physical Oceanography*, (6), 379-389.

Smith, S.R., Legler, D.M. and Verzone, K.V. 2001. Quantifying Uncertainties in NCEP Reananlyses Using High-Quality Research Vessel Observations. *Journal of Climate*, 14, 4062-4072.

Steiner, N., Harder, M. and Lemke, P. 1999. Sea-ice roughness and drag coefficients in a dynamic-thermodynamic sea-ice model for the Arctic. *Tellus*, 51A(5), 964-978.

Stössel, A., Lemke, P. and Owens, W.B. 1990. Coupled sea ice-mixed layer simulations for the Southern Ocean. *Journal of Geophysical Research*, 95(C6), 9539-9555.

Sturman, A.P. and Anderson, M.R. 1986. On the sea-ice regime of the Ross Sea,

Antarctica. *Journal of Glaciology*, 32(110), 54-59.

Timmermann, R., Beckmann, A. and Hellmer, H.H 2002a. Simulations of ice-ocean dynamics in the Weddell Sea, Part 1: Model configuration and validation. *Journal of Geophysical Research*, 107(C3), 10.1-10.11.

Timmermann, R., Beckmann, A. and Hellmer, H.H 2002b. Simulations of ice-ocean dynamics in the Weddell Sea, Part 2: Interannual variability 1985-1993. *Journal of Geophysical Research*, 107(C3), 11.1-11.9.

Tin, T., Jeffries, M.O, Lensu, M. and Tuhkuri, J. 2003. Estimating the thickness of ridged sea ice from ship observations in the Ross Sea, Antarctica. *Antarctic Science*, 15(1).

Tin, T. and Jeffries, M.O. in press. Morphology of deformed first year sea ice features in the Southern Ocean. *Cold Regions Science and Technology*.

Van Woert, M.L. 1999. Wintertime expansion and contraction of the Terra Nova Bay polynya In: Spezie, G. and Manzella, G.M.R. (eds.) *Oceanography of the Ross Sea, Antarctica*, 145-164. Springer-Verlag, Milan, Italy.

Webb, David J. and 16 others (The FRAM Group). 1991. *An eddy-resolving model of the Southern Ocean*. Eos, 72(15), 169, 174.

Wadhams, P. 1998. Sea ice morphology. In: M. Leppäranta (ed.) *Physics of ice-covered seas*: lecture notes from a summer school in Savonlinna, Finland 6-17 June, 1994. University of Helsinki, Department of Geophysics, 1998, Vol. 1, 231-287.

Weeks, W.F., Ackley, S.F. and Govoni, J. 1989. Sea ice ridging in the Ross Sea, Antarctica, as compared with sites in the Arctic. *Journal of Geophysical Research*, 94(C4), 4987-4988.

Wadhams, P., Lange, M.A. and Ackley, S.F. 1987. The ice thickness distribution across the Atlantic sector of the Antarctic ocean in midwinter. *Journal of Geophysical Research*, 92(C13), 14535-14552.

Walsh, J.E., Hibler, W.D., III and Ross, B. 1985. Numerical simulation of northern hemisphere sea ice variability, 1951-1980. *Journal of Geophysical Research*, 90(C3), 4847-4865.

Worby, A. and Allison, I. 1999. A technique for making ship-based observations of Antarctic sea ice thickness and characteristics. Part I Observational technique and results. Antarctic CRC Research Report, No. 25.

Worby, A.P. and Wu, X. 1998. East Antarctic sea ice: observations and modelling. *Annals of Glaciology*, (27), 427-432.

Wordie, J.M. 1921. The Ross Sea drift of the "Aurora" in 1915-1916. *Geographical Journal*, 58(3), 219-224.

Zhou, X., Li, S. and Morris, K. 2001. Measurement of all-wave and spectral albedos of snow-covered summer sea ice in the Ross Sea, Antarctica. *Annals of Glaciology*, (33), 267-274.

Zwally, H.J., Comiso, J.C. and Gordon, A.L. 1985. Antarctic offshore leads and polynyas and oceanographic effects. In: S.S. Jacobs (ed.) *Oceanology of the Antarctic continental shelf, Antarctic Research Series*, vol. 43, 203-226. American Geophysical Union, Washington, DC.

Conclusions

In this study, I made use of sea ice thickness data collected on icebreaker cruises together with a numerical model to achieve two study objectives. The first objective was to enhance our ability to estimate ice thickness remotely, and the second objective was to examine the dynamic and thermodynamic processes involved in the development of ice prior to its observation during icebreaker cruises.

The new and original research undertaken in this study include:

- the first examination of the relationship between the surface roughness and ice thickness of Antarctic sea ice;
- development of a quantitative criterion specifically for identifying deformed features from drill profiles obtained from Antarctic sea ice;
- the first quantitative examination of the morphology and state of hydrostatic equilibrium of Antarctic deformed features, including a comparison between Arctic and Antarctic pressure ridges and an assessment of the factors that contribute towards the observed differences;
- an improvement of the methodology used to estimate ice thickness from ship observation data. This was accomplished by incorporating more realistic components of ridge morphology into the assumed geometrical model.
- an examination of the evolution of sea ice thickness in the Ross Sea by combining detailed field observations with a numerical model. This was the first study to examine dynamic and thermodynamic processes along simulated backward trajectories in the study area.

Study findings indicate that there are statistically significant correlations between mean snow elevation and mean ice thickness, and between mean snow surface roughness and mean ice thickness over profiles of $\geq$ 100 m in length. Deformed ice features can be

assumed to be hydrostatically balanced on the length scale of ≥ 100 m but the assumption is not valid at the scale of individual ridge sails. Results also show that for the autumn Ross Sea ice cover, the probability that a sail is associated with a keel underwater is 0.48 while the probability that a keel is below a level snow surface is 0.07. In view of the first study objective of enhancing our ability to estimate ice thickness remotely, these findings indicate that ice thickness can be estimated fairly reliably from surface observations using hydrostatic equilibrium or statistical relationships on length scales of the order of ≥ 100 m but not on smaller length scales. Also, the effect that not all sails are associated with a keel underwater and not all keels are associated with a sail on the surface must be accounted for when estimating ice thickness from surface observations.

In view of the second study objective of examining the processes involved in the development of ice, results from different aspects of the study all indicate that ice dynamics plays an important role in determining the sea ice thickness distribution in the Ross Sea. Results from analysis of ice thickness data show that approximating the mass in deformed ice features by the surrounding level ice thickness underestimates the ice mass within individual deformed ice features by roughly 50%, and underestimates the ice mass in a 1 000 km^2 area by approximately 30%. Model results indicate that in the Ross Sea, dynamic thickening is active through autumn, winter and spring. In autumn and at the beginning of winter, when thermodynamic thickening dominates, dynamic thickening still contributes 20% towards the net ice thickening rates. Thermodynamic thickening slows down during the rest of the winter and dynamic thickening becomes the dominant ice thickening process as a result of high winds acting on a compact ice cover. Model results also indicate that the winds are accompanied by ample precipitation which adds mass to the ice cover in the form of snow ice. Ice thickness is further influenced by the occurrence of bottom melting, which arises from increased oceanic heat flux due to new ice formation in open water areas created by ice deformation. By summer, dynamic thickening and snow ice formation decrease with decreasing ice concentration and snow thickness, and melting dominates.

Other aspects of the study have also produced new and interesting findings. From my comparison between the morphology of Antarctic and Arctic first year ridges, I have shown that Antarctic ridges are flatter and less massive than their Arctic counterparts. Differences are greater when compared to ridges in the Beaufort Sea than those in the Arctic temperate regions. I propose a number of hypotheses which, in addition to differences arising from sampling strategies, may explain the differences between the morphology of Arctic and Antarctic ridges. First, Arctic temperate and Antarctic ridges are both formed by the rafting and ridging of first year floes; therefore they are similar in size and smaller than the ridges in the Beaufort Sea, which are built from young lead ice as it is pushed against thick first year or multi-year floes. Second, higher surface friction on Antarctic parent ice causes a higher keel area to sail area ratio in Antarctic pressure ridges than in Arctic pressure ridges. Third, lower ice strength and driving forces result in smaller and flatter ridges in the Southern Ocean. These observations and hypotheses provide a fertile ground for future investigations. In-depth field studies of the anatomy of Antarctic deformed features can provide much needed information for understanding their formation mechanisms. Such studies should include examination of the cross-sectional profile of the deformed feature, the sizes and orientations of the constituent blocks, and the macro porosity and amount of consolidation of the deformed feature. Measurements of the winds and ocean currents acting on the ice cover, and the stress and strain sustained by the ice cover would also aid in explaining the differences in ridge morphology. Since it is difficult to simulate or observe the formation of deformed features in the field, laboratory or numerical modeling studies can be used to examine the processes and ice characteristics that may explain the differences between Arctic and Antarctic ridges. Field studies and laboratory or numerical modeling experiments should be coordinated. The study process should be iterative, with field observations giving rise to hypotheses that are tested in experiments and experimental results being verified in the field.

Other findings of this study have also opened up a variety of questions that may be

pursued upon further study. Although the study indicates a significant correlation between mean snow elevation and mean ice thickness, and between mean snow surface roughness and mean ice thickness, there is a need for the collection and analysis of more elevation and thickness data before ice thickness can be estimated accurately from air or spaceborne altimetry. Additional data can contribute towards estimating and constraining the accuracy of the estimated ice thickness. Data from different regions and at different times will provide information for accurate estimations of ice thickness throughout the Southern Ocean all year round. If ice thickness is to be retrieved accurately from laser altimetry data collected onboard satellites such as ICESAT or CryoSat, field data must be examined at a length scale comparable to that of the satellite footprint.

Another direction for future research is in the quantification of the accuracy of ice thickness estimated from ship-based visual observations. This study has illustrated the use of ship observations data in describing ice conditions and in validating numerical models. I hope that a robust quantification of the accuracy of ice thickness estimated from ship observations data will promote the use of the data in future studies. Accuracy of the estimated ice thickness can be quantified by measuring ice thickness accurately at a large number of locations within the radius of observation and comparing the mean measured ice thickness with the ice thickness calculated from ship observations data. Accurate ice thickness measurements can be made by drilling single holes or short transects. The choice of sample locations can be greatly enhanced by the availability of helicopter support. Such comparison exercises should be made for at least one observation at every 100 km (or 1° latitude) in order to sample a wide range of different ice conditions.

This study introduced the concept of following the evolution of a small parcel of ice floes in time as it drifts in space. Since such field data are not currently available in the Ross Sea, in this study, the concept was examined using a numerical model. However, field studies that examine ice properties and forcing conditions along drift trajectories would provide invaluable insights into the evolution of the ice thickness distribution. This can be accomplished with a drifting ice station that follows the drift of the ice. Ice core

and oceanographic data can be collected along the drift trajectories and the evolution of ice thickness and the processes that determine it can be monitored along the trajectories.